THE UNIVERSITY
of EDINBURGH

Fluorescence Microscopy of Inkjet Prints

Maria Diana Castro Spencer

Degree of Doctor of Philosophy

The University of Edinburgh

2010

Abstract

Inkjet printing technology has been developing rapidly during recent years, pressing the ink and paper manufacturers to develop a better understanding of the mechanism of fixation of inkjet dye into the substrate.

The aim of the work described in this thesis was to investigate the three-dimensional distribution of inkjet dye in paper and the interaction between dye and paper using advanced fluorescence microscopy techniques, Confocal Laser Scanning Microscopy (CLSM), and Two-photon Fluorescence Lifetime Imaging Microscopy (2P-FLIM).

It has been shown that CLSM is a valuable, non-destructive, rapid technique for three-dimensional imaging of printed samples and evaluation of print quality. The intrinsic fluorescence of both the inkjet dye and the paper substrate can be used to determine the spread and penetration of ink droplets in different inkjet papers. The optical sectioning capability of CLSM enables the position of the ink layer relative to the paper surface and the penetration depth of the ink to be quantified. It was observed that while in the microporous type of inkjet paper the penetration depends on the quantity of ink in the printed sample, in the swellable type of inkjet paper the penetration is almost the same for different amounts of ink.

2P-FLIM has been employed to spatially map, in three-dimensions, fluorescence lifetimes by measuring the lifetime at each pixel in the image. Fluorescent molecules in both the ink and paper were analysed. Because the fluorescence lifetime is affected by the local molecular environment, the fluorescence lifetime maps provide information on the interaction between inkjet dye and paper. Analysis of fluorescence lifetime maps reveals the interaction between dye molecules and silica or alumina particles in the paper, variations of the molecular environment within a single ink dot and that interaction between dye and paper is affected by pH.

Declaration

I declare that the work presented in this thesis is my own unless otherwise stated by a reference.

Maria Diana Castro Spencer
May 2010

Acknowledgements

I would like to thank God for giving me the opportunity and helping me to achieve one of my dreams.

Thanks to my supervisor Dr Anita Jones, for all her support, help, guidance, teaching, patience, help and continuous encouragement. Dr Jones has not only been a supervisor but an example of excellence.

I would also like to thank Dr Patricia Richardson for all her help during my PhD, Dr Robert Neely for taking the time to install and show me how to use the 2P-FLIM equipment and his guidance with FLIM software and to Dr J. Arlt for his great help in Cosmic.

I am very grateful to Dr Owen Lozman and Dr Thomas Paul, of FFIC for valuable discussions and help with all the necessary prints and dyes.

Thanks to all in room 252, in particular Xiaohua, Mathieu, John and Nuha. All of you have contributed greatly to making my experience at the university very enjoyable. Thanks to Mathieu for helping me so much with all the lifetime measurements and for your friendship.

Thanks to Dr H. Baxter and Dr R. Baxter for their encouragement and help to finish my thesis.

And finally a big thanks to all my family, Carolina, Scott, Felipe, Stephen, Catalina, Ana Maria and Thomas, for their fabulous support, help, love and continuous encouragement during this time. Thank you!

Abbreviations

2PE	two photon excited fluorescence microscopy
2P-FLIM	two photon -fluorescence lifetime imaging microscopy/ microscope
3D	three-dimensional
C	concentration
CLSM	confocal laser scanning microscopy/microscope
FFIC	Fujifilm Imaging Colourants
FLIM	fluorescence lifetime imaging microscopy/ microscope
FRET	fluorescence resonance energy transfer
FWHM	full width of a curve at the half-maximum height
I	Intensity
k_f	rate constant for fluorescence emission
k_n	rate constant for radiative processes
k_{nr}	rate constant for non-radiative processes
MCP	multichannel plate
n	refractive index
NA	numerical aperture
OBA	optical brightening agent
PMT	photomultiplier tube
RhB	rhodamine B
SOHO	small ofice and home printing
PVOH	polivynilalcohol
PVA	polivynilacrilate
PVP	polivynilpirrolidine
UV	ultraviolet
ε	extinction coefficient
λ	wavelength
Φ	quantum yield
T	fluorescence lifetime

1 Introduction

During the last decade inkjet printing technology has developed very rapidly and new printers with high speed and resolution are now available on the market, extending applications from conventional printing of documents and photographs to new technologies such as manufacturing of organic light-emitting displays. High-quality photo-images with a resolution that exceeds that of the human eye [1] can now be created, however, the physical principles underlying inkjet technology are not yet completely understood. For this reason inkjet technology has attracted the interest of research scientists. The Inkjet Research Centre at the University of Cambridge has been studying jet and drop creation, drop flight and drop/surface interaction, inkjet applications and novel printing materials [2]. In Sweden, at Karlstad University, there has been research on printability and on the interaction between ink and paper [3]. Manufacturers of ink and paper are also continuously analysing the relation and interaction between ink and paper in order to produce better inkjet inks and papers.

The present work, which has been carried out in collaboration with Fujifilm Inkjet Colorants (FFIC) Ltd, has been concerned with investigating the utility of fluorescence microscopy to study inkjet printing, taking advantage of the intrinsic fluorescence of some inkjet inks. The aims of this work were: (i) to examine the shape and radial spread of inkjet dots printed on a variety of papers; (ii) to determine whether confocal laser scanning microscopy (CLSM) could be used to obtain quantitative information on the depth of penetration of ink into paper; (iii) to determine whether two-photon excitation microscopy offered any significant advantages over CLSM in these applications; and (iv) to investigate the potential of fluorescence lifetime imaging microscopy (FLIM) to provide information on ink–paper interactions.

In Chapter 2, a brief introduction to inkjet technology and the history of its development is given. Chapter 3 presents a account of the theory of the absorption and emission of light by molecules. Chapter 4 describes the principles and methodology of the fluorescence microscopy techniques used in this work.

Chapter 5 reports the use of confocal laser scanning microscopy to image directly the ink printed on paper. Firstly, results of imaging the radial spread of individual inkjet dots,

printed on different types of paper, are presented. Then, the use of CLSM to slice the sample (optically), and thereby measure the depth of penetration of ink into paper, is described. The latter technique was validated by comparison of the results with those obtained from imaging of a corresponding physical cross-section of printed paper. In Chapter 6 measurements of radial spread and depth profiles using two-photon excitation microscopy are compared with those obtained using CLSM and the relative merits of the two techniques are assessed.

Chapter 7 describes the use of fluorescence lifetime imaging microscopy in combination with a model ink (rhodamine B dye) to explore ink–paper interactions, by exploiting the environmental sensitivity of the fluorescence lifetime of the dye. The results reveal association of the dye with different components of the paper structure.

Finally, in Chapter 8 the overall conclusions that can be drawn from the work are presented, together with suggestions for future studies.

2 Inkjet technology

Inkjet technology is a dot-matrix printing technology in which a series of ink droplets ejected from small orifices (nozzles) located in the printer head hit the surface of a suitable medium to create an image. The droplets are electronically controlled and fired to certain points known as pixels, which are small squares of a definite dimension. The number and size of these small dots determine the resolution of the image, measured as 'dots per inch' (dpi). Most printed colour images are the result of multiple droplets of four basic colours, cyan, magenta, yellow, and black according to optical principles.

Inkjet printing technology has been improving very rapidly during recent years and new printers with high speed and resolution are now available. New printers can create high-quality photo-images with a resolution that exceeds that which can be detected by the human eye. However, the complete physical theory behind inkjet technology is not yet completely understood.

2.1 Inkjet printers

In 1878 Lord Raleigh proposed a mechanism by which a liquid stream is broken into droplets [4] which is the basis of inkjet technology.

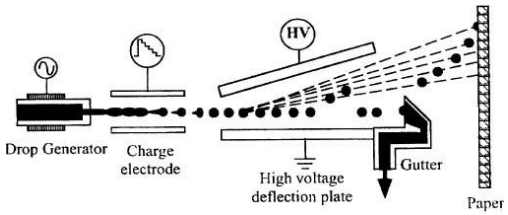

Figure 2-1 Schematic representing a 'Continuous Inkjet System' Reproduced from reference [4]

It was not until 1951, however, that the first commercial 'continuous' inkjet printer was produced by Siemens. During the following years, this 'continuous mode' was constantly improved. Sweet, in 1960, discovered that by applying a pressure wave to the print head, the ink was forced through the nozzles producing droplets of uniform size [4]. He then decided to split the dots and found that, by applying an electric charge in a selective way, the desired

dots would hit the paper while the others would be deflected and sent for recirculation as shown in Figure 2-1[4]. Using this basic principle, IBM produced its first inkjet printer in 1976, the IBM 4640.

In 1973 a new technology was developed by Cambridge Consultants called ‘drop on demand’ which allows the production of controlled droplets, making inkjet technology a more reliable technique [4]. In 1979, both Canon and Hewlett Packard simultaneously developed their own ‘drop on demand technology’, known as bubble-jet or thermal inkjet technology [4].

As shown in Figure 2-2, a drop is ejected from the nozzle of the print head after a tiny resistive heating element, located near the nozzle, heats a small volume of ink, normally water based, producing a steam bubble that expands generating the necessary pressure to eject a tiny ink droplet. After the drop is ejected, the bubble collapses, the pressure is reduced and fresh ink is admitted from the reserve tank as shown in Figure 2-3 [4]

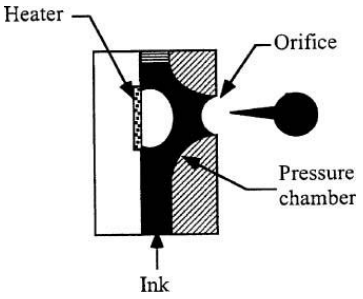

Figure 2-2 Schematic representing a ‘drop on demand’ inkjet system. Reproduced from reference[4].

The first Hewlett Packard print heads had only 12 nozzles. Print heads were relatively cheap, and they were changed with each cartridge. This technology is still used by Hewlett Packard, Canon, Lexmark, Olivetti and Xerox.

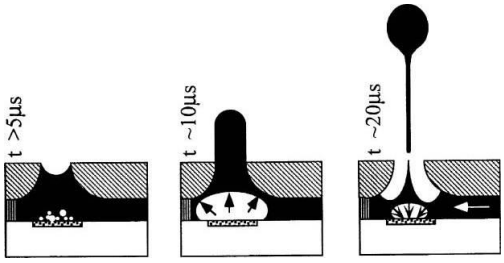

Figure 2-3 Schematic representing the drop formation process. Reproduced from reference [4]

In 1987 Cambridge Consultants patented a different technology using piezoelectric crystals [1]. This technology uses a ceramic that vibrates at high frequency when an electric charge is applied (Figure 2-4). The vibration forces the ink through the nozzle producing the droplet. Using this new technology Epson created a printer, in 1993, which had a 'built-in' print head that did not have to be changed with each ink cartridge. This technology is still used in Epson printers.

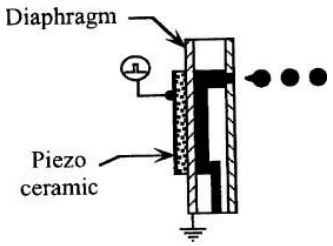

Figure 2-4 Schematic representing a 'Piezo-electric inkjet' system. Reproduced from reference [4]

During the last few years, the goal of manufacturers of inkjet printers has been to achieve better resolution, faster, more reliable and cheaper printers. Superior resolution is accomplished through smaller drops (5 to 150 pl) that will give resolutions between 100 to 1600 dpi. Faster printers need to have more nozzles per print head or more print heads per system and they must maintain the accuracy of droplet position in order to continue to be reliable. Hewlett Packard provides an example of this evolution, having started with a printer with 12 nozzles in 1984 and offering a printer with 10560 nozzles in 2006. The resolution of the latest printers is so high that it exceeds the resolution capability of the human eye.

Because of the rapid development in inkjet technology and the requirements of the market predicted for coming years (Figure 2-5), research must continue in order to improve the properties and attributes of ink and substrate to obtain high-quality printed images.

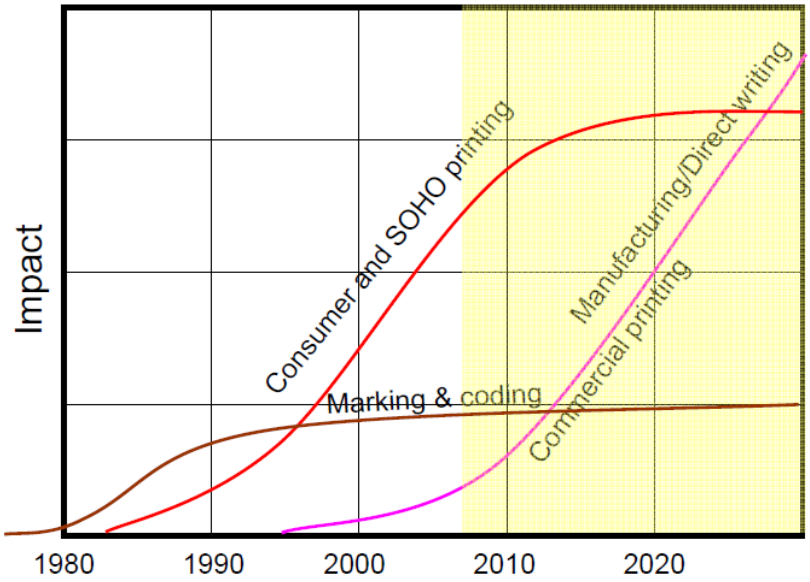

Figure 2-5 Inkjet technology trend in consumers, small office and home printing (SOHO), marking and coding, manufacturing and commercial printing (Reproduced from reference [2])

2.2 Inkjet inks

The chemistry of the ink is an important parameter as it affects print quality, determines drop ejection characteristics and controls the reliability of the printing system [4]. There are several types of inkjet inks depending on the printer and substrate. The most common types of inks are: water-based inks, commonly used in home and small office printers; solvent-based; UV-curable; and hot melt inks. Table 2-1 shows the drying process of the different types of ink.

Type of ink	**Drying process**
Water-based	Absorption and evaporation
Solvent based	Evaporation and absorption
UV-curable	Absorption and UV-curing equipment
Hot-melt	Solidification by temperature decrease

Table 2-1 Types of ink and drying process

The inkjet ink undergoes many processes during printing; first, it is kept in the print head, then it is transformed into droplets, absorbed or adsorbed by the substrate, fixed to the substrate and finally exposed to several environmental and mechanical agents.

The colourant can be a dye or a pigment. Dyes are small molecules (less than 10 nm) [3] that are soluble in the carrier fluid; they provide highly saturated and intense colours often fade easily due to their sensitivity to environmental agents such as humidity and ozone. Pigments are very fine solid particles dispersed in the carrier fluid with a much bigger particle size that offers more stability. The disadvantage of these pigmented inks is that they have a rough surface when printed that scatters the light, producing duller colours. They also have some inherent problems as their relatively large particle size can cause nozzle clogging. This is a big problem as the technology tends towards smaller nozzle diameter to obtain a higher resolution. Presently we can find printers producing drops with an average volume of 3 pl and a diameter of 18 μm [2]. However, new technology is allowing the preparation of smaller pigment particles improving the print quality.

Water-based inks were the first used in inkjet printing and are still common today.

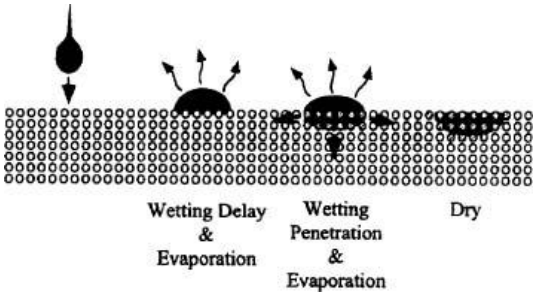

Figure 2-6 Drying mechanism of a water-based inkjet drop on plain paper. Reproduced from reference [4]

Figure 2-6 illustrates the behaviour of a water-based ink drop when it hits the surface of uncoated paper [4]. When the drop hits the surface it tends to spread and then penetrate the paper. The rate of absorption and evaporation determines the position of the dye. The position of the ink depends on the physical and chemical properties of the ink and the paper, and their interaction. As the eye can only detect the colour near the surface, all the newly developed inkjet papers have an ink-receiving layer that traps the dye near to the surface as the ink is absorbed. This will generate images that are well defined and have vibrant colours.

A typical ink formulation for a narrow format, home or office inkjet printer is a complex mixture with an average of 20 different compounds. Its principal constituents are: dyes (2–5%), surfactants and additives (2–5%), co-solvent (30%) and water (65%) [5]. Because of the high percentage of water in the ink, a good paper must have the ability to absorb water rapidly and at the same time fix the dye at the surface of the paper. The ink dots formed must be bright, round, have well-defined edges and offer good colour contrast. To achieve this, surface tension, viscosity, composition and pH have to be carefully balanced [5].

According to Fleming [5] the ink density or print darkness is affected by the electrostatic interactions between the anionic dyes and the oxides present in the first coating layer of the inkjet paper.

The solvent-based inks are normally used for commercial applications such as coding and marking on cans and bottles. They dry faster than aqueous inks, but emit volatile organic compounds. An ultraviolet light cures the UV inks; they are used in wide-format printing of rigid substrates. The disadvantages of these inks are the high cost, and health and safety risks. Hot-melt inks are used in industrial marking and in labelling. The great advantage of these inks is that they can be used in several substrates and their disadvantages are due to the topography of the prints because they can suffer abrasion.

2.3 Inkjet papers

The paper or substrate has the function of receiving and holding the ink, and creating the image. An inkjet paper should therefore hold the ink as near as possible to the surface to provide high optical print density, have a fast solvent absorbency rate to prevent colour bleeding, and produce images with high water and light fastness [3].

The choice of the correct paper depends on the particular settings of the printer for a particular use. Therefore there is a wide range of coated papers depending on the application for which they are intended. In order to produce high-quality prints, inkjet papers need a special coating. The market offers mainly two types of coating: pigment or microporous, and resin- or swellable-based coatings although combinations of these systems also exist [3]. Photo papers are typically multi-layered systems consisting of an ink-receiving layer, a protective layer and the substrate which is normally cellulose.

In the pigment or microporous coating, the ink is absorbed into a porous pigment network. Silica is the most common pigment used because of its good absorbency capacity based in its large surface area (in the range of 50–1000 m^2/g, available for ink adhesion) due to its inter- and intra-particle pores. Various types of silica pigment are available: fumed, gel, precipitated and colloidal. Their particle sizes typically range from less than 100 nm to greater than 1 μm. Alumina is also used as pigment in inkjet coatings with particle sizes similar to those of silica. This type of coating uses different polymers as binders that absorb the ink solvent and at the same time help to immobilise the pigment and attach them to the base of the paper. Therefore when used in aqueous inks, highly water-absorbent binders are used such as polyvinyl alcohol (PVOH), polyvinyl acetate (PVA) and polyvinyl pyrrolidone (PVP) among others. PVOH is the most efficient binder [3] for use with silica as a pigment. The most common additives in this type of coating are the optical brightening agent (OBA) and the cationic polymer believed to help in the fixation properties of the inkjet-receiving layer by attracting the anionic dye molecules to the very large surface of the silica pigment.

Swellable or resin-type papers have an ink-receptive coating, usually made of a combination of polymers similar to gelatine that swells when receiving or accommodating the ink. As the water evaporates, the coating layer shrinks back to its original thickness keeping the dye inside. The drying process in this type of paper is relatively slow and sensitive to humidity but produces images with very good stability.

3 Theory of fluorescence

In this thesis the intrinsic ability of some dye and paper molecules to absorb light of a given wavelength and emit light of a different wavelength, is exploited by using various fluorescence microscopy techniques to measure the spread and penetration of dye droplets in different inkjet papers. The purpose of this chapter is to summarise the theoretical principles that rule the interaction of these types of molecules with light and to understand the basis of the techniques used to monitor these interactions.

3.1 Electronic Spectroscopy

Every molecule has a distinctive and quantized electronic composition which determines its ability to absorb light. Some molecules can absorb a specific wavelength of light that excites an electron from a low- to a high-energy level, and emits light of a different wavelength, a few nanoseconds later, when the electron returns to its ground energy level. Many of the colours of objects around us, such as the green of vegetation, the colours of the flowers and those of the dyes are due to these types of electronic transitions [6].

3.1.1 Absorption

When a molecule absorbs a photon of light with energy (E), an electron in the ground electronic state (E_m) is promoted to a higher (excited) electronic state (E_n).

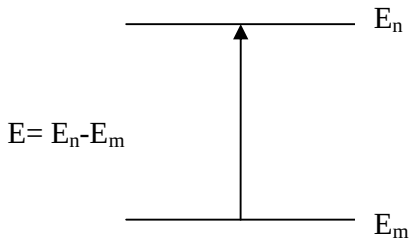

Figure 3-1 Illustration of an absorption of a photon of light with energy (E), causing an electronic transition from the ground state (Em), to an excited state (En).

$$E = E_n - E_m$$ **Equation 3-1**

Every molecule has a characteristic absorption pattern that depends on its electronic structure [7].

The absorption is caused by the interaction of the electric vector of the light with the electrons and nuclei of the molecule. This interaction is described in terms of a vector quantity called the transition dipole moment (μ_{mn}) related to the wave functions of the ground (Ψ_m) and excited state (Ψ_n) by the dipole moment operator (μ) [8, 9].

$$\mu_{mn} = \int \Psi_m \, \mu \, \Psi_n \, d\tau \qquad \textbf{Equation 3-2}$$

The probability of a photon being absorbed depends on the square of the transition dipole moment. If the transition dipole moment is zero then the probability of occurrence is zero and it is called a forbidden transition, otherwise it is an allowed transition [10].

These transitions can be experimentally measured, considering the Beer-Lambert Law that relates the intensity of absorption (A), to the concentration (c) of the absorbing species, the length (l) of the sample in which absorption occurs, and the molar absorption coefficient (ε) of the absorbing species at a particular wavelength.

$$A = \log \frac{I_0}{I} = \varepsilon \, c \, l \qquad \textbf{Equation 3-3}$$

(where I_0 is the intensity of incident radiation and I is the intensity of the transmitted light.)

The absorption of light by substances with colour is due to these types of electronic transitions. Every dye or pigment has a characteristic absorption spectrum obtained by measuring the absorbance (A) at different wavelengths.

3.1.2 De-excitation

All the excited molecules must return to the ground state after a period of time that will depend on the decay paths available. The Jabloński diagram Figure 3-2, illustrates schematically the processes that contribute to the decay of the excited state [11].

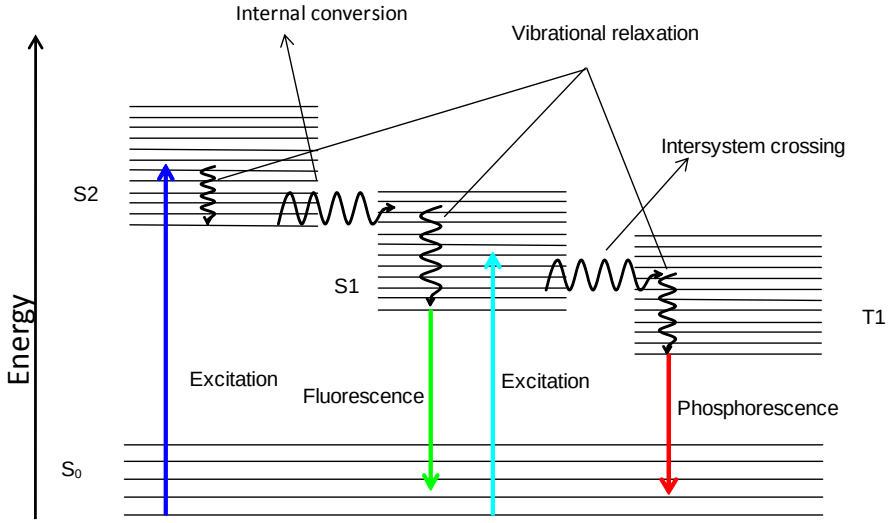

Figure 3-2 Jabloński Diagram. The absorption (blue) and radiative decay processes (green and red) are denoted by straight lines and the non-radiative processes by wavy arrows.

3.1.3 Non-radiative decay

The intramolecular non-radiative decay processes are vibrational relaxation, internal conversion and intersystem crossing, and all of them compete with the radiative processes, fluorescence and phosphorescence.

3.1.3.1 Vibrational relaxation

Each electronic excited state (S_1, S_2) has several vibrational levels, represented as horizontal lines in Figure 3-2. Vibrational relaxation occurs between these closely spaced levels. During this process, energy is thermally transferred to the environment. Kasha's rule establishes that, in condensed phases, this vibrational relaxation occurs very rapidly, on the picoseconds timescale, compared with the fluorescence [12].

3.1.3.2 Internal conversion (IC) and intersystem crossing (ISC)

When an electron jumps between isoenergetic vibrational levels of two different electronic energy states (S), with the same spin multiplicity, a non-radiative decay process, called internal conversion, occurs (Figure 3-3).

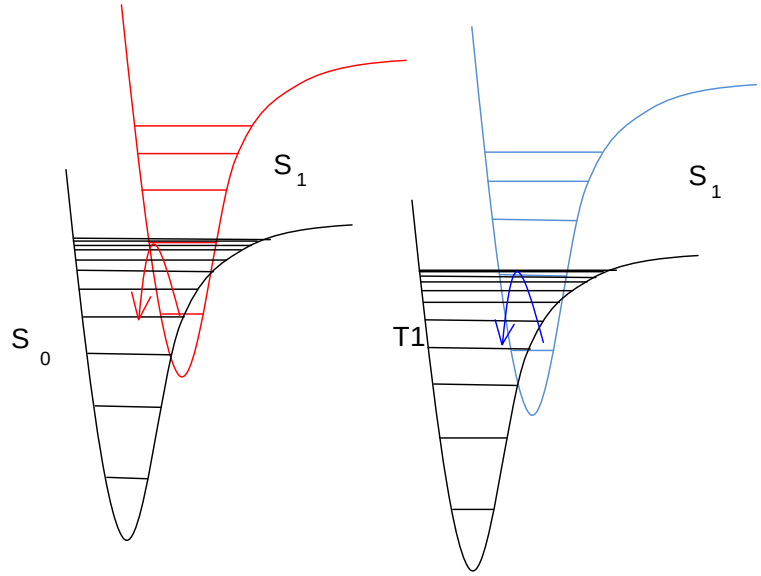

Figure 3-3 Schematic representation of internal conversion (red) between singlets and intersystem crossing (blue) between triplets or energy levels with different multiplicity. Reproduced from [13].

Intersystem crossing (ISC) is a non-radiative decay that occurs when the process takes place between two electronic energy levels with different multiplicity and therefore is a spin-forbidden transition. As shown in Figure 3, both IC and ISC result in conversion of electronic energy into vibrational energy [6]. In the condensed phase, the excess vibrational energy is lost to the surroundings as heat.

3.1.4 Radiative decay

Radiative decay occurs when an electronically excited molecule returns to its ground electronic state, emitting a photon of radiation. There are two types of radiative decay: fluorescence, which occurs between electronic states of the same spin multiplicity, and phosphorescence, which occurs between electronic states of different spin multiplicity. Transitions between states of the same multiplicity are allowed and take place in a short interval of time, of the order of nanoseconds to picoseconds; while transitions between states with different multiplicity are of a forbidden nature and occur on a longer timescale, of the order of milliseconds to seconds. Phosphorescence is not relevant to the work presented in this thesis and will not be considered further.

3.2 Fluorescence

Some molecules, fluorophores, have the ability to absorb light of a particular wavelength and emit light of a longer wavelength. This phenomenon occurs when a molecule, originally in its ground state (S_0), absorbs a photon and is excited to a higher electronically and excited state, such as S_2 or S_1, and then emits a photon of lower energy when returning to its ground electronic state. As explained previously, before returning to the ground state, the molecule suffers radiationless processes that are very fast which means that in general fluorescence will occur only from the ground vibronic level of the S_1 state. This theory, known as Kasha's rule, establishes that, for fluorophores in a condensed phase, the emission spectrum of a fluorophore is independent of the excitation wavelength.

The excitation spectrum of a molecule shows the distribution of the emission intensity as a function of excitation wavelength and contains information about the vibrational structure of the excited state. The emission spectrum on the other hand shows fluorescence emission intensity as a function of emission wavelength and gives information relating to the ground state vibronic levels.

Figure 3-4 shows the different vibrational structures in the excited state and in the ground state, and how both the excitation and emission processes depend on these vibrational levels.

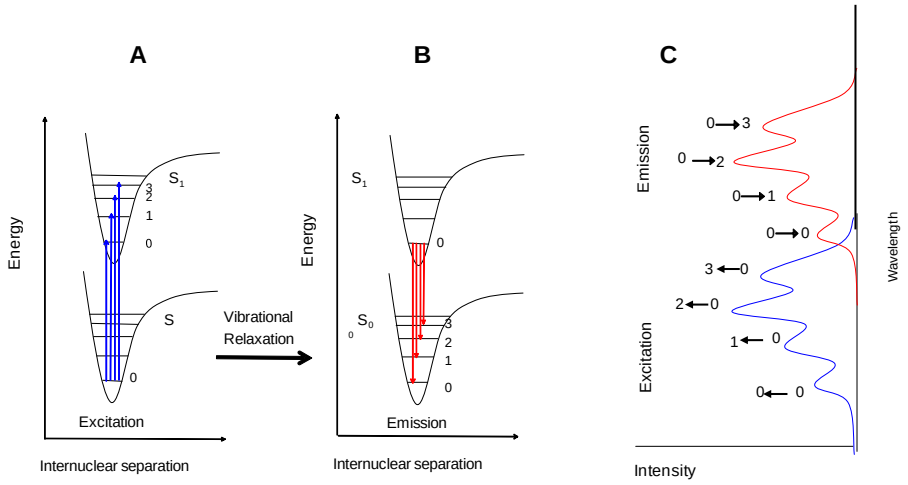

Figure 3-4 Schematic representation of transitions that occur during the excitation (A) and emission (B) events of a fluorophore, and excitation and emission spectra (C) showing the transitions happening during excitation and emission. (Reproduced from [14])

Radiative decay competes with non-radiative decay processes which means that the fluorescence quantum yield (ratio of photons emitted to photons absorbed) is generally less than one. The energy released as fluorescence is lower than the energy absorbed when excited, due to loss of energy to the environment. This means that the emission wavelength is shifted to the red (longer wavelength) compared with excitation spectrum, as shown in Figure 3-5.

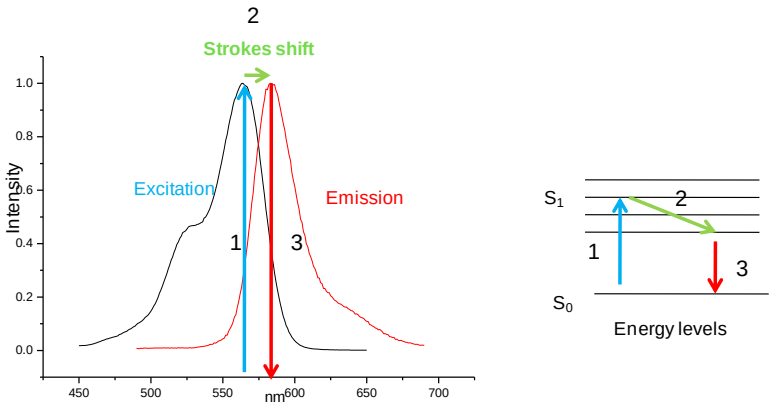

Figure 3-5 Excitation (black) and emission fluorescence spectra (red) showing Stokes' shift between them and a schematic of the electronic levels showing excitation and emission and the Stokes' shift.

Figure 3-5 illustrates the Stokes' shift which is defined as the difference in wavelength between the maximum of the excitation spectrum and the maximum of the emission spectrum. The fact that the fluorescence emission occurs in a different region of the spectrum, at longer wavelengths, explains why fluorescence spectroscopy is such a useful technique that allows the detection of the small amount of photons emitted by the fluorophores with no interference from the large amount of exciting photons.

Most fluorophores used in microscopy are large aromatic molecules with delocalised π-electron systems which absorb and emit in the visible region. They are photostable molecules which can absorb and emit many times before suffering photochemical decomposition or photo-bleaching with the corresponding loss of fluorescence intensity.

The development of a wide range of efficient fluorophores has contributed greatly to the development of new bio-imaging techniques that have revolutionized many aspects of biology and medicine.

3.2.1 Fluorescence decay kinetics

All excited fluorophores will return to the ground state and the rate of this process, considering the radiative and non-radiative routes, obeys a first-order kinetic equation.

$$-\frac{d[M^*]}{dt} = (k_R + k_{NR})[M^*] \qquad \textbf{Equation 3-4}$$

(where [M*] is the concentration of excited fluorophore molecules at time (t) after the excitation, and k_R and k_{NR} are the emissive and non-radiative rate constant respectively.)

Considering k_F as the sum of the rate constant in both processes and integrating the above equation, because all the excited fluorophores have the same probability of emitting fluorescence in a period of time (t), an exponential expression for the fluorescence decay is obtained, as shown in Equation 3-5.

$$[M^*](t) = [M^*]_0 e^{-(k_F t)} \qquad \textbf{Equation 3-5}$$

(where and $[M^*]_0$ is the concentration of M* at t= 0.)

In fluorescence experiments the parameter measured is the fluorescence intensity (I_F) which depends on the concentration of excited molecules.

$$I_F(t) = k_R[M^*] \qquad \textbf{Equation 3-6}$$

Substituting [M*] from Equation 3-6 gives:

$$I_F(t) = I_0 k_R e^{-(k_F t)} \qquad \textbf{Equation 3-7}$$

(where I_0 is the intensity at the time of the excitation pulse.)

The fluorescence lifetime (τ) is defined as the time in which the fluorescence intensity decays to 1/e of the initial intensity (I_0) and is the inverse of the rate constant of the decay ($1/k_F$). So rewriting equation 3-7:

$$I(t) = I_0 e^{\frac{-t}{\tau}}$$ **Equation 3-8**

(where $\tau = (1/k_F)$.)

Equation 3-8 relates intensity to the fluorescence lifetime, quantities that can be experimentally measured. The technique employed to measure the fluorescence lifetime in this thesis is fluorescence lifetime imaging microscopy (FLIM) explained in detail in Chapter 4.

3.2.2 Fluorescence lifetime

The fluorescence lifetime (τ) represents the time that the molecule can stay in an excited state and interact with other molecules in the environment.

$$\tau = \frac{1}{k_R + K_{NR}}$$ **Equation 3-9**

Where K_R and K_{NR} are the radiative and non-radiative rate constants respectively.

Each fluorophore has a distinctive fluorescence lifetime value within certain specific environmental conditions During the period of time that a molecule remains in an excited state it can be affected by intermolecular interactions or the properties of the surroundings. These environmental interactions affect the rate of non-radiative decay and this means that the fluorescence lifetime may be sensitive to factors such as polarity, temperature, pH, viscosity and interactions with other molecules (e.g. by collision or energy transfer) [12].

The Strickler Berg formula, Equation 3-10, predicts that the fluorescence lifetime is inversily proportional to the square of the refractive index [15].

$$K_R = \frac{1}{\tau_0} = 2.88 * 10^{-9} n^2 \frac{\int I(\nu)\, d\nu}{\int I(\nu)\nu^{-3} d\nu} \int \frac{\varepsilon(\nu)}{\nu}\, d\nu$$ **Equation 3-10**

where τ_0 is the natural lifetime, I is the fluorescence emission, ε is the extinction coefficient, ν is the wave number, and n is the refractive index. The Strickler Berg formula predicts that the radiative process depends on the refractive index of the environment.

The fluorescence quantum yield (Φ) is an indicator of the fluorescence efficiency and is defined as the relation between the number of photons emitted and the number of photons absorbed. A high quantum yield will responsible for a very intense emission and will create high-contrast images when observed under a fluorescence microscope.

$$\Phi_F = \frac{number\ of\ photons\ emitted}{number\ of\ photons\ absorbed}$$ **Equation 3-11**

The fluorescence quantum yield can be related to the fluorescence lifetime by Equation 3-12.

$$\Phi_F = \frac{k_R}{k_F} = k_R \tau_F$$ **Equation 3-12**

(where k_R is the rate constant for the radiative or fluorescence decay and it is unique for each fluorophore because it depends on the intrinsic electronic structure of the fluorophore.)

3.2.3 Fluorescence Resonance Energy Transfer (FRET)

Fluorescence resonance energy transfer is a process by which an excited molecule (donor) can transfer its energy to a nearby chromophore (acceptor) . The absorption spectrum of the acceptor must overlap the fluorescence emission spectrum of the donor molecule.This exchange of energy between one another is a result of a non-radiative dipole-dipole interaction. The efficiency of this process depends on the distance between both molecules, usually not higher than 100 Å.When FRET occurs the fluorescence lifetime of the donor is quenched and the lifetime of the acceptor is increased [12].

4 Fluorescence Microscopy

The purpose of this chapter is to present a brief account of the different types of fluorescence microscopy techniques used throughout this work to observe the behaviour of the dyes when absorbed by different inkjet papers and measure their fluorescence lifetimes within different inkjet paper environments.

4.1 Introduction

Fluorescence microscopy is an optical technique capable of imaging a specimen based on its fluorescence emission. The specimen can be intrinsically fluorescent or can be labelled with extrinsic fluorescent molecules. In a fluorescence microscope, the fluorophore is excited with a specific wavelength of light and the emitted fluorescence is collected by an appropriate detector which by transforming the signal and sending it to a computer creates a high-contrast image. This technique has several advantages, such as: high selectivity, because the excitation and emission spectra are intrinsic properties of the molecule; high sensitivity, because a very small amount of fluorescence can be detected, even fluorescence from a single molecule [12].

Fluorescence microscopy employs two types of optical paths: the transmitted light illumination (diascopic fluorescence), in which a condenser focuses the exciting light on to the objective; and the epi-illumination (episcopic fluorescence) where the exciting light is reflected directly into the objective by a dichroic beam-splitting mirror. For the work presented in this thesis, epifluorescence microscopy was used.

4.1.1 Epifluorescence Microscope

In this type of microscope the sample is excited with a specific wavelength light and the fluorescence emitted is collected by the objective and sent to the detector through a dichroic or dichromatic mirror. The dichromatic mirror is an optical beam-splitter device designed to reflect lower wavelength light (excitation) and transmit higher wavelength light (emission) for one photon excitation processes and the opposite for two photon excitation processes. Figure 4-2 shows the mode of operation of an epifluorescence microscope.

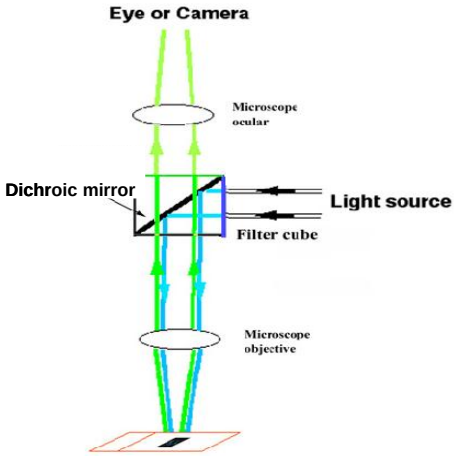

Figure 4-1 Diagram illustrating the optical path in an epifluorescence microscope [12].

The main components of an epifluorescence microscope are the excitation light sources, the optical lenses, the objectives, stage and specimen chambers [12].

4.1.2 Confocal Laser Scanning Microscope

Confocal microscopy can be considered a modern technique. With the development of new lasers, affordable computers and new digital imaging software in the late seventies, the first confocal laser scanning microscopes were built and applied to biological and material specimens [10].

Confocal laser scanning microscopy is a technique that generates three-dimensional (3-D) optical images without any detriment to the sample [16]. Figure 4-2 illustrates the main parts of a confocal laser scanning microscope (CLSM). A group of lasers provides the source of excitation. The laser light or exciting light, passes through an excitation pinhole, is reflected by a dichroic mirror or beam splitter and focused by a microscope objective to a small spot in the object. The light is absorbed by the sample and the intrinsic or artificially added fluorophores emit fluorescence spherically in all directions. The objective then collects some of this emitted light that has a longer wavelength than the excitation light and sends it to the detector via the dichroic mirror through a second pinhole located in front of it. The detectors used by the CLSM are photomultiplier tubes (PMT) [10].

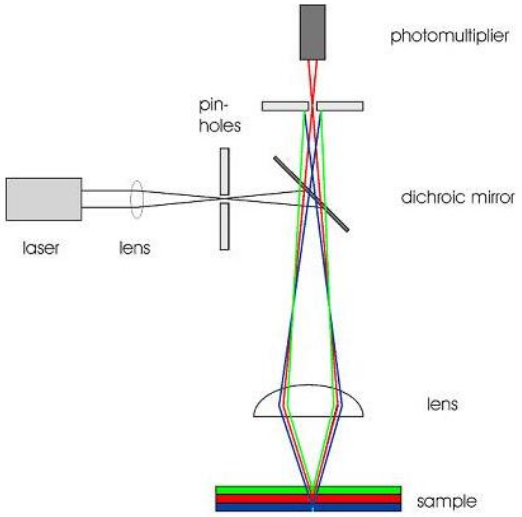

Figure 4-2 Simplified diagram of confocal laser microscopy set-up (courtesy of J. Gutenberg Universität).

4.1.2.1 Wavelength selection filters

In a fluorescence microscope the excitation and emission wavelengths are selected by filters that are designed to transmit a certain part of the electromagnetic spectrum, while reflecting the rest of the spectrum. There are different types of filters on the market, short or long pass filters as well as specific filters designed to transmit or reflect only a narrow band of wavelengths. Figure 4-3 is a graphic representation of how they work.

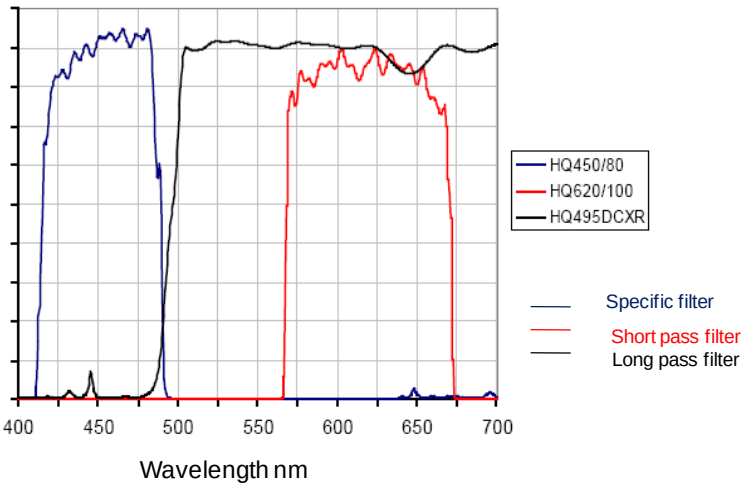

Figure 4-3 Types of filters used in fluorescence microscopy; short pass filter, long pass filter, and specific filter.The vertical axis (y) represents transmission and horizontal axis (x) represents wavelength in nm (Graphic from Biorad – Confocal Scanning System Manual) [17].

4.1.2.2 Microscope objectives

The fluorescence microscope objective plays an important role in the quality of the image the microscope is able to produce. The aim of the objective is to focus the laser light to a small point in the sample, and collect and transmit the emitted light generated to the detector. The design of each objective comprises a complex series of optical elements carefully positioned with respect to each other, aiming to achieve an optimal performance under several types of illumination, providing at the same time, various degrees of optical correction for the primary optical aberrations.

Figure 4-4 A fluorescence microscope objective marked with the necessary specifications to determine the application for which the objective is designed. (Courtesy of Nikon).

Every fluorescence microscopy objective is stamped with its specifications as shown in Figure 4-4. These engravings show what the objective is designed for and the required conditions for its use. The characteristics inscribed are: manufacturer; flat-field correction abbreviated as Plan, Pl, E; aberration correction, marked as Achro or Achromat (achromatic), Fl, Fluar, Fluor, Neofluar or Fluotar (fluorite), and Apo (apochromatic) which corresponds to the highest degree of spherical and chromatic aberrations; magnification; numerical aperture (NA); tube length for which the objective was designed to give its finest images (usually 160 millimetres or the Greek infinity symbol); the thickness of cover glass protecting the specimen (usually 0.17 millimetres); the working distance which is distance between the closest surface of the cover glass and the objective front lens; magnification

colour code; immersion medium, which can be oil or water, or, when these designations are absent the objective is meant to be used dry; with air between the lowest part of the objective and the specimen; and finally, the objective can have other special features that are specific to a particular manufacturer and type of objective.

The NA is an important parameter that expresses the amount of emitted fluorescence light the objective is able to collect. If the sample is considered as a point, an angle (α) can be defined as the angle between the direction of the emitted fluorescence light and the excitation light, then the NA is defined by the following equation:

$$NA = n \sin \alpha$$ **Equation 4-1**

(where n is the refractive index of the immersion medium.)

Objectives capable of collecting light over a large α angle will create bright images and are called large numerical aperture (NA) objectives. The NA values can vary from a range of 0.1 for very low magnification objectives to as much as 1.6 for high-performance objectives. Figure 4-5 illustrates the concept of numerical aperture.

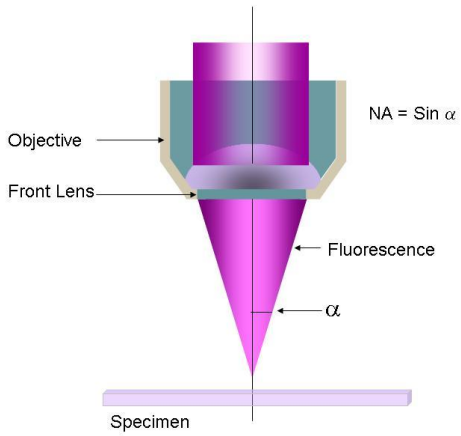

Figure 4-5 Illustration of the meaning of numerical aperture (NA), showing the angle (α) of light collected.

4.1.2.3 Microscope resolution

The resolution of a fluorescence microscope (r), which is defined as the minimum detectable distance between two small points, depends on the wavelength of the excitation light and the numerical aperture of the objective.

$$r = 0.61 (\lambda / NA) \quad \text{or} \quad r = 0.61 (\lambda / (n \sin \alpha)$$ **Equation 4-2**

(where r is the distance between two objects and λ is the wavelength of the excitation light.)

This means that a high NA value and a short wavelength excitation light will be associated with a high objective resolving power. It can be concluded that the resolution limit of the microscope depends on the wavelength of the excitation light, the angular aperture of the light captured by the objective and the refractive index of the immersion medium.

4.1.2.4 Specimen chambers and stages

Different types of chambers are available depending on the specific application. For this thesis the samples analysed were printed inkjet papers that were cut into small squares and fitted in a specially designed metallic device that held the paper as a sandwich between two surfaces to keep it flat on the stage of the inverted microscope. The Biorad 2000 used in this work had a computer-controlled xy and xz stage.

4.1.3 The detection pinhole in the CLSM

The pinhole in front of the detector is located in a conjugate plane with both the plane of focus of the microscope objective and the point of excitation of the laser (confocal pinholes). These pinholes will give first, a focused exciting laser and second, a detected signal with no out-of-focus information from above or below the focal plane.

The ideal pinhole diameter will depend on the magnification (M), the ratio between the excitation and detected wavelength, and the numerical aperture of the objective (NA). In the case of the Biorad Radiance 2000 the pinhole size is set to be equal to the Airy disk

diameter, according to the following formula, which the system calculates automatically [17]:

$$\text{Diameter of pinhole} = \frac{73.2\ \lambda\ M}{N.A.} \qquad \textbf{Equation 4-3}$$

(where λ is considered as the middle value of the emission band pass filter, M is the objective magnification and NA is the numerical aperture of the objective.)

The axial resolution is affected by the NA of the objective and can be calculated by the following formula:

$$r_{axial} = \frac{2\lambda}{n(\sin^2\ \alpha)} = \frac{2\ \lambda}{n(\sin^2\ (\sin^{-1}(NA/n))} \qquad \textbf{Equation 4-4}$$

(where n is the refractive index of the medium used between the objective and sample.)

The lateral resolution in a confocal laser scanning microscope is the same as that obtained by a wide-field microscope and is defined by Equation 4-2.

From these equations it is obvious that the lateral resolution is inversely proportional to the NA and the axial resolution is inversely proportional to the square of NA and λ as well.

4.1.4 Laser scanning

In a confocal fluorescence microscope the image is formed by detecting the photons emitted at each point of the sample. To obtain an optical section or an image, the laser has to raster across the sample in a two-dimensional area (xy), point by point, and the signal is sent from the detector to a computer where the image is created. By taking successive images at focal planes in the z-axis direction, optical stacks can be collected and a 3-D image can be created by using digital imaging processing software as shown in Figure 4-6. The thickness of the optical sections can be as small as 500 nm depending on the aperture of the pinhole. A laser scanning device in which the excitation laser is scanned across the sample is used, rather than moving the sample, as this provides higher scan speeds.

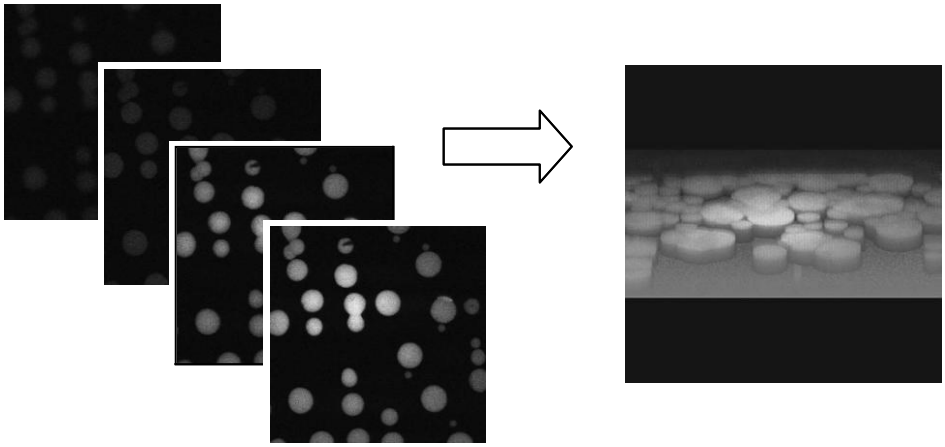

Figure 4-6 Optical sections in z-axis provided by the CLSM and a 3-D image of dye Ar52 printed on coated inkjet paper using Image J as the image analysis software.

4.1.5 Lasers

Lasers are the source of excitation used by commercial confocal microscopes. Their extremely directional and bright output makes them appropriate for this application allowing efficient sample illumination.

The Biorad CLSM had a set of different lasers that permit excitation of fluorophores within a wide range of wavelengths. Table 4-1 shows the different lasers available in the Biorad Radiance 2000MP system used.

Laser	Laser medium	Wavelength nm	Power mW
Ar	Argon	457, 476, 488, 514	14.00
He-Ne	Helium-Neon Gas	543	1.50
Red Diode		633	5.00

Table 4-1 Lasers used in CLSM.

It is important to use the minimum possible power to minimise the amount of energy directed to the sample to reduce the possibility of photobleaching or damage.

The CLSM used has the ability to excite the sample with three different lasers (wavelength) and at the same time detect the emitted fluorescence in three different channels by three

different PMT detectors. This means that three fluorophores can be detected independently at the same time and can be spatially correlated in the three-dimensional image obtained.

4.1.6 Detectors

All detectors for fluorescence microscopy must be able to sense low levels of emitted fluorescence. These photo-detectors must have a good quantum efficiency (QE) or fraction of photons that generate an output signal and good control of noise level. The detectors available for fluorescence microscopy can be divided into photon detectors or photomultiplier tubes (PMT) or image detectors (cameras). PMTs are very sensitive devices that are able to detect single fluorescent photons and convert their energy into electrical pulses. All CLSM and FLIM experiments were carried out using a photomultiplier tube.

As we can see in Figure 4-7 the emitted photon excites the electrons in the cathode causing the emission of a photoelectron that is accelerated by the electric field, created by the voltage applied between the photocatode and the anode. These photoelectrons collide with the internal wall of the channel causing the emission of secondary electrons and this process is repeated several times generating a great number of electrons released at the output end. These types of detectors can amplify the current 10,000 times.

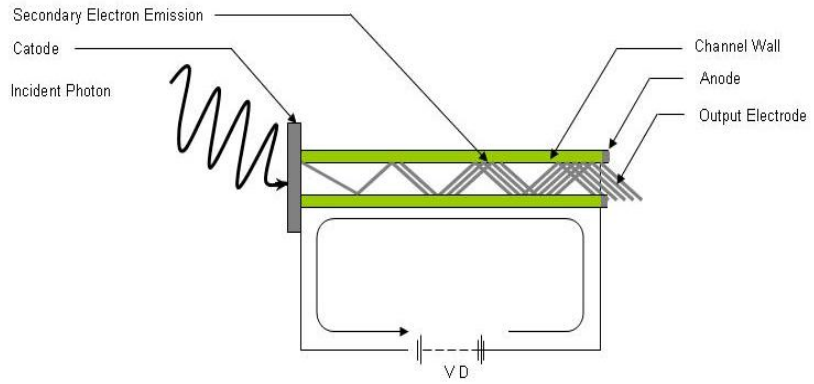

Figure 4-7 Illustration of the operating mechanism of a PMT.

The Biorad Radiance 2000 MP CLSM has three PMTs on different detector channels. A transmission detector is also available to collect the transmitted scanned laser light.

4.1.7 System software – LaserSharp

The Biorad Radiance 2000 uses the LaserSharp 2000 software which allows the system to control different acquisition parameters, builds and displays the image. The first step, when planning an experiment in the Biorad Radiance 2000 CLSM, is to create a method choosing the necessary excitation laser wavelength followed by selecting the appropriate dichroic mirror, emission filter and detector. This procedure has to be repeated for each fluorophore present in the sample. Figure 4-8 shows the optics and filters dialog box.

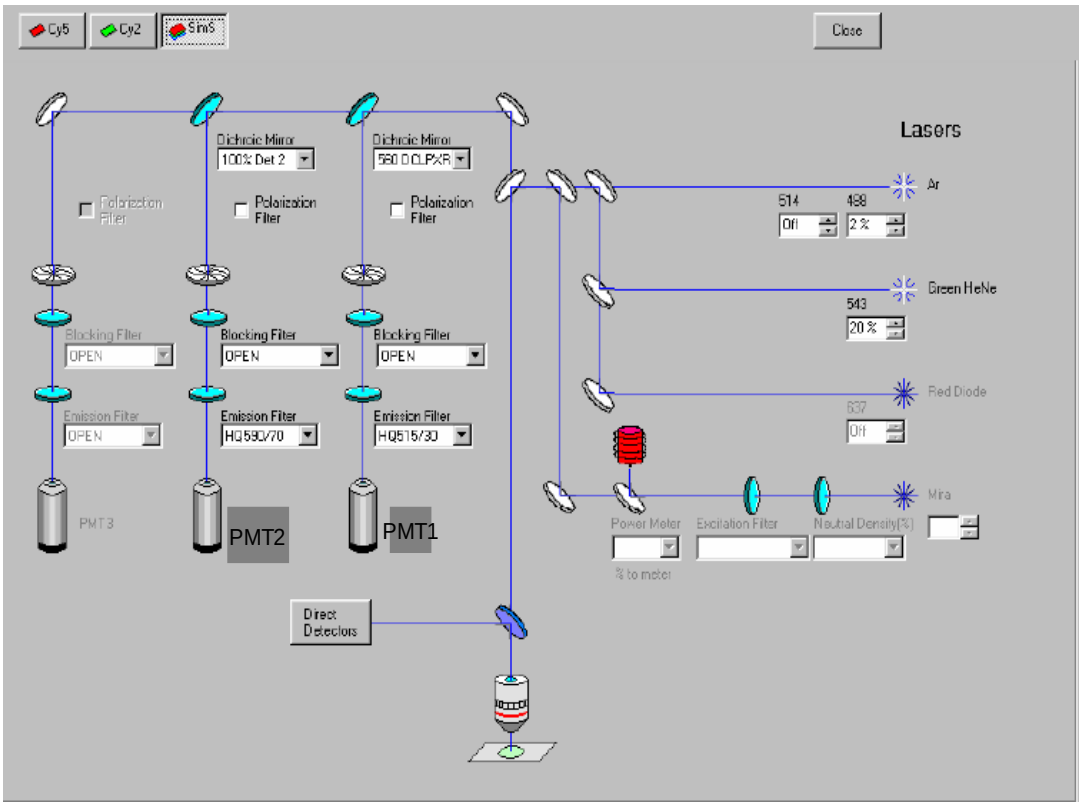

Figure 4-8 Illustration of the optics and filters dialog box of the Laser Sharp software .

Once the method is created and saved, the experiment can begin and the screen will display one or more images, depending on the number of channels chosen.

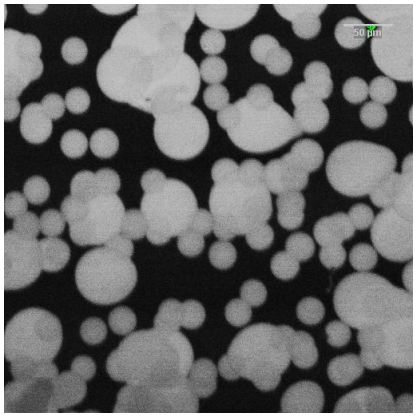

Figure 4-9 CLSM image of an inkjet paper printed with a magenta ink, with 10% colour, permitting the identification of small drops.

To obtain good contrast images, certain parameters must be controlled during the experiment such as: scan speed, collection method, zoom, laser power, pinhole diameter or iris, gain and offset values as shown in Figure 4-10.

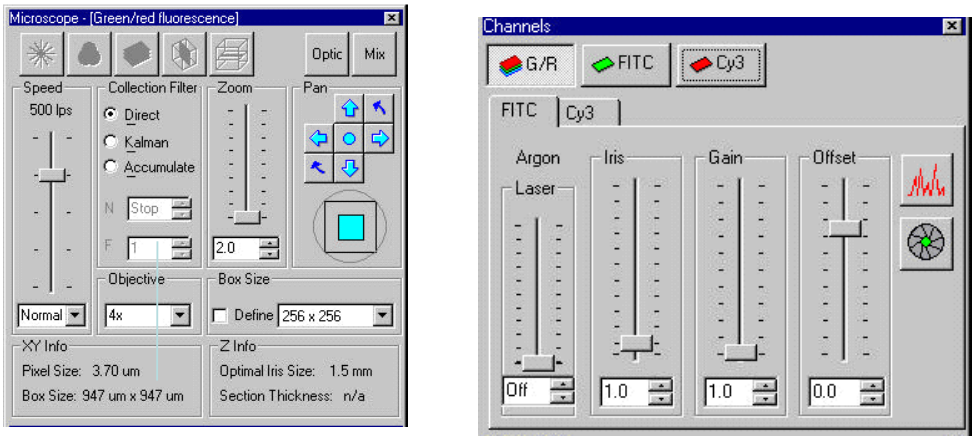

Figure 4-10 Laser Sharp dialog box with scanning and detector controls. Left panel showing a scanning speed of 400 lines per second (LPS), direct collection, zoom of 20 and a 4X objective. Right panel showing the power of the laser, the pinhole diameter or iris (1.0), Gain (1.0) and offset (0.0).

The software allows the control of the optical system set-up, previously established when creating the method, through the Optics/Filter configuration dialog shown in Figure 4-8.

To complete a z-stack the system needs the input of the start (bottom of the image) and stop position (top of the image) together with the desired step size, which ideally is half the thickness of each optical slice. Figure 4-11 shows the dialog box available to construct z-stacks.

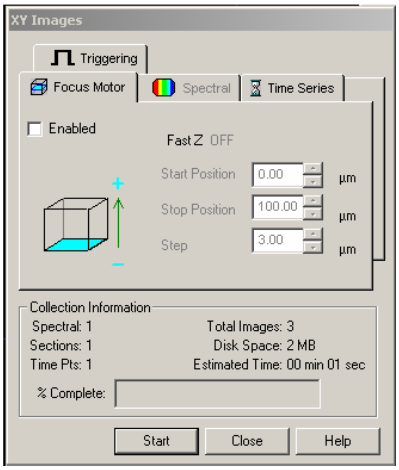

Figure 4-11 Dialog box showing the input data for the focus motor as start position for scanning and the stop position together with the selected step size. It gives the information of the number of images per stack as well as disk space needed and an estimated recording time.

Image processing and analysis functions are possible with this software but for our purposes Image J [18] was used for the analysis of the data obtained.

4.2 Two-photon excited fluorescence microscopy (2PE)

Two-photon excitation fluorescence microscopy is considered the most important advance in optical microscopy since the introduction of confocal imaging in the 1980s [19]. Two-photon excited fluorescence microscopy (2PE) represents a novel application of quantum physics and has proven to be a very useful technique for biologists as it allows deep imaging, avoiding photobleaching, as absorption above or below the plane of focus is eliminated.

4.2.1 Introduction

Based on the Heisenberg uncertainty principle, in 1931 Göppert-Mayer proposed that one atom or molecule was capable of absorbing two photons simultaneously in a single quantized

event (within 10^{-16} -10^{-17} s) but it was not until 1960 that this phenomenon could be observed and confirmed, with the development of lasers as light sources [19].

4.2.2 Basic principles

In a 2PE process two photons are absorbed simultaneously exciting an atom or molecule from the ground state to an excited state. The sum of the energy of the two photons absorbed must be equal to the total excitation energy needed for the transition, as shown in Figure 4-11.

If $h\nu_A$ is the energy needed by one photon to excite an atom or molecule from the ground state (S_0) to an excited state (S_1), and $h\nu_{A1}$ and $h\nu_{A2}$ are the energies of the two photons required to achieve the same transition in a two-photon event then:

$$h\nu_A = h\nu_{A1} + h\nu_{A2} = 2h\nu_{A1} \qquad \textbf{Equation 4-5}$$

(assuming $h\nu_{A1} = h\nu_{A2}$)

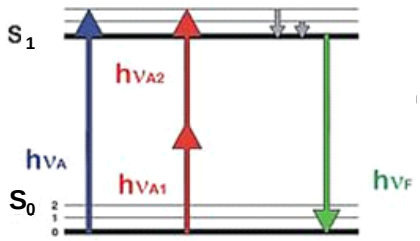

Figure 4-12 Jablonski diagram for a two photon absorption. $h\nu_A$ is the energy required for a one photon excitation, $h\nu_{A1}$ and $h\nu_{A2}$ are the energy of the two photons needed for a two photon excitation and $h\nu_F$ the energy of the induced fluorescence photon.

Since the energy of a photon is inversely proportional to its wavelength, Equation 4-6 can be rewritten as:

$$\frac{1}{\lambda_A} = \frac{1}{\lambda_{A1}} + \frac{1}{\lambda_{A2}} = 2\left(\frac{1}{\lambda_{A1}}\right) \qquad \textbf{Equation 4-6}$$

or

$$\lambda_{A1} = 2\lambda_A \qquad \textbf{Equation 4-7}$$

(where λ_A is the wavelength needed for the one-photon event and λ_{A1} the wavelength needed for the two-photon excitation.).Thus, the laser wavelength required for two-photon excitation is twice that required for a one-photon excitation. For a 2PE process to occur, the two photons must arrive at a certain location at the same time (within ~10^{-16}s) which means that the excitation light must be highly localised and therefore the molecular cross-section for the two-photon absorption (δ_2), is very small, in the order of 10^{-58} m^2s^{-1} [19]. High-power lasers, mostly short-pulse lasers, must be used to achieve a two-photon excitation process. After excitation, the molecule returns to the ground state emitting fluorescence as described in Equation 4-9.

$$I_E = k\,\Phi\ \delta\,(I_{exc})^2 \qquad \textbf{Equation 4-8}$$

(where I_E is the fluorescence intensity, I_{exc} is the excitation intensity, δ is the molecular cross-section, Φ is quantum yield and k is a factor that takes into account the collection efficiency of the set-up.)

Because two-photon excitation depends on the simultaneous absorption of two photons, the resulting fluorescence intensity scales quadratically with the excitation intensity [10].

It has been estimated that the number of photon pairs (n) that a fluorescent molecule can absorb simultaneously during a single event is [19]:

$$n \sim g^2 \frac{\delta \lambda_{exc} P^2}{\tau_p f_p} \left(\frac{NA^2}{2hc\lambda_{exc}} \right)^2 \qquad \textbf{Equation 4-9}$$

(where P is the average power of the beam, NA is the numerical aperture of the microscope objective, τ_p is the pulse duration and f_p is the pulse repetition rate.)

The value of g^2 depends on the shape of the pulse. Equation 4-10 shows that the excitation intensity can be kept below the saturation threshold by controlling the laser repetition pulse rate. If τ_{fl} is the fluorescence lifetime of the molecule, the fluorescence emission will start when n $f_p \sim 1 / \tau_{fl}$, therefore,

if the laser pulse repetition rate is of the order of $1 / \tau_{fl}$ or less, the excitation intensity can be kept under the saturation threshold. The most commonly used fluorophores have a lifetime, τ_{fl}, in the region of 10 ns which is equivalent to a pulse repetition rate f_p of less than 100 MHz, which is the repetition rate that 2PE lasers should have. Equation 4-10 confirms that the probability of an interaction between the excitation laser and the fluorophores depends on the two-photon cross-section (δ), thereby a large cross-section will enhance the probability of a two-photon excitation event succeeding. These cross-sections have been measured for some fluorophores and the values given in GM units ($1GM = 10^{-50}$ cm^4s^{-1} photon) can be found in the literature [19].

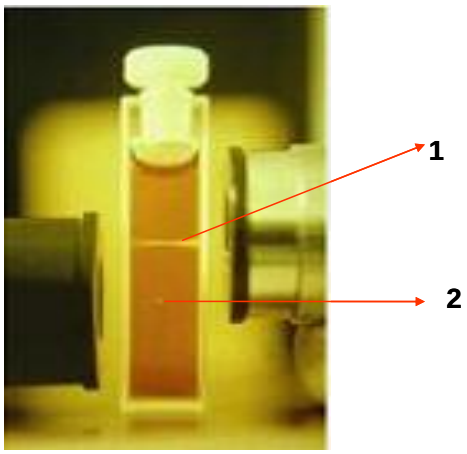

Figure 4-13 Fluorescence emission of a solution of fluorescent molecules excited by a one-photon event (1) and a two-photon event (2). (Diagram courtesy of Brad Amos, MRC, UK))

Figure 4-13 shows the comparison between a one- (1) and a two-photon (2) excitation event showing the spatial confinement (a bright point) that represents the two-photon excitation. This property provides the 2PE technique with an optical-sectioning capability which means there is no need for detection pinholes as used in the CLSM.

The most important advantage of two-photon excitation microscopy is its ability to provide optical sectioning at great depths in thick samples. This capacity of penetrating deeply into a sample is the result of three physical properties of the two-photon excitation microscopy (2PEM).

The photons reach deeper levels within the sample because of the absence of out-of-focus absorption. Red and infrared light commonly employed in 2PEM undergoes less scattering than blue light. Although it is difficult to calculate the exact scattering behaviour in most of

the samples, due to its irregular material distribution, the simplest approximation of Rayleigh scattering predicts that the scattered light is inversely proportional to the fourth power of the wavelength [10]. In 2PEM there is no detection pinhole and therefore a greater fraction of fluorescence emitted by the sample is collected.

Both the lack of out-of-focus absorption and the reduction of scattered light increase the amount of excitation light reaching the focal plane, and the absence of a pinhole in front of the detector increases the contrast of the image detected.

Figure 4-14 shows the comparison between lateral and axial resolution for a CLSM and a 2PEM made by Müller [10]. The calculation of the point of spread function (PSF) was made assuming that the detection and excitation wavelength were identical, the pinhole size was the same as the Airy disk diameter projected and the excitation wavelength employed for the 2PEM was 800 nm. Under these conditions it was found that the lateral and axial resolution for 2PEM is slightly reduced compared with the CLSM.

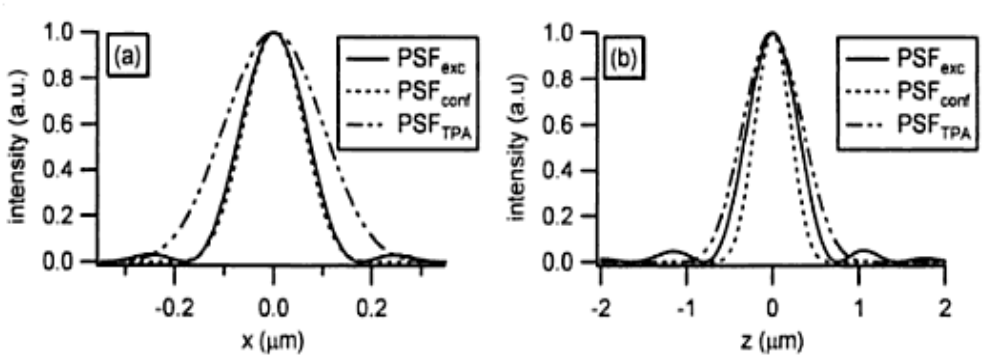

Figure 4-14 Lateral (a) and axial (b) resolution for CLSM, 2PEM. The parameters used were: 1.2 NA, oil-immersion microscope objective, excitation wavelength of 488nm for CLSM and 800 nm for 2PEM. Pinhole equal to the projected Airy disk. (Illustration courtesy of Michiel Müller – Confocal Fluorescence Microscopy) [10] .

4.2.3 Two-photon excitation microscopy set-up

The two-photon excitation microscopy system used was basically the same Biorad Radiance 2000 used for CLSM, but with the continuous wave (CW) lasers replaced by a mode-locked Titanium-sapphire laser.

4.2.3.1 Laser sources

The source of light used in this work was a tuneable Ti:sapphire Coherent Mira laser able to produce pulses of light between 750 nm and 950 nm, with a duration of approximately 200 fs and a repetition rate of 76 MHz (one pulse approximately every 13 ns) and power up to 500 mW.

The pulses of light are produced by the passive mode-locking method. The Ti:sapphire crystal refracts light as a function of intensity. This is called the Kerr-Lens modelocking technique and the process itself is initiated by an optical design that varies the laser cavity length to create short pulse fluctuations by focusing high-intensity light differently than low-intensity light. The Ti:sapphire crystal emits by stimulated emission over a range of wavelengths. These wavelengths are achieved by rotating a birefringent filter that act as a bandpass filter for the polarised intracavity beam.

4.3 Two-photon Fluorescence Lifetime Imaging Microscopy (2P-FLIM)

For the work presented in this thesis, a Time Correlated Single Photon Counting (TCSPC) module, (Becker and Hickl bh SPC-730), coupled with the CLSM and Ti: sapphire laser, was used to perform Fluorescence Lifetime Imaging Microscopy (Figure 4-15).

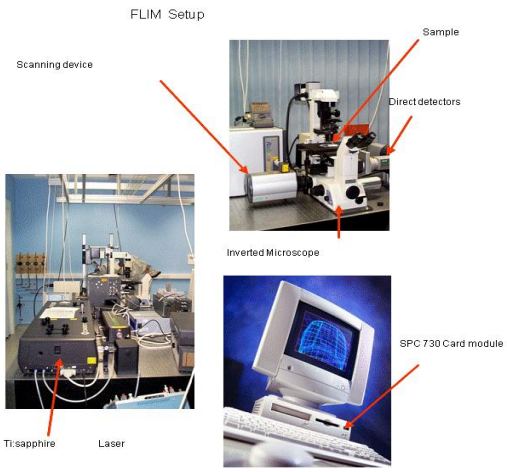

Figure 4-15 Two-photon fluorescence lifetime imaging set-up.

4.3.1 The principles of time-correlated single-photon counting

Time-correlated single-photon counting (TCSPC) is the experimental technique used throughout this work to determine the fluorescence lifetime(s) of some dyes printed in different inkjet papers. In TCSPC, the interval of time between excitation of a fluorophore (dye) with a short pulse of light and detection of the first photon of fluorescence emitted by the sample is measured and by repeating this procedure many times, a distribution of arrival times for individual photons is obtained [20]. This distribution of time data, called the fluorescence decay, allows the calculation of the fluorescence lifetime of the fluorophores present in the sample. The bh SPC-730 module contains all the electronics on a single PCI-compatible PC board.

4.3.2 Detector

The detector head used was the PMH-100 which contains a small and fast PMT, a high-voltage generator, a preamplifier and a photo-sensor module. The PMH-100 is powered directly from the SPC module with a stable timing response function at high count rates. A shutter assembly equipped with a lens for efficient light transfer in the non-descanned beam path of the two-photon laser scanning microscope was used to prevent overload and damage of the detector.

The FWHM of the Instrument Response Function (IRF) of the PMH module varies from about 120 ps to 140 ps [20].

4.3.2.1 Data processing – The SPCM software

The bh SPC-730 TCSPC module has a "Multi SPC Software" package that provides measurement parameters settings, measurement control, scanning control, online calculation and display of data in two-dimensional and three-dimensional modes, loading and saving of results and system parameters. The data stored is analysed by the bh SPCImage data analysis software explained in detail in the following section.

The main panel of the SPCM can be run in different modes. The oscilloscope mode is used initially to establish the optimal experiment parameters while the average fluorescence decay

curve is generated and the configuration used for recording fluorescence lifetime in this thesis is the “Scan Sync In” mode (Figure 4-16).

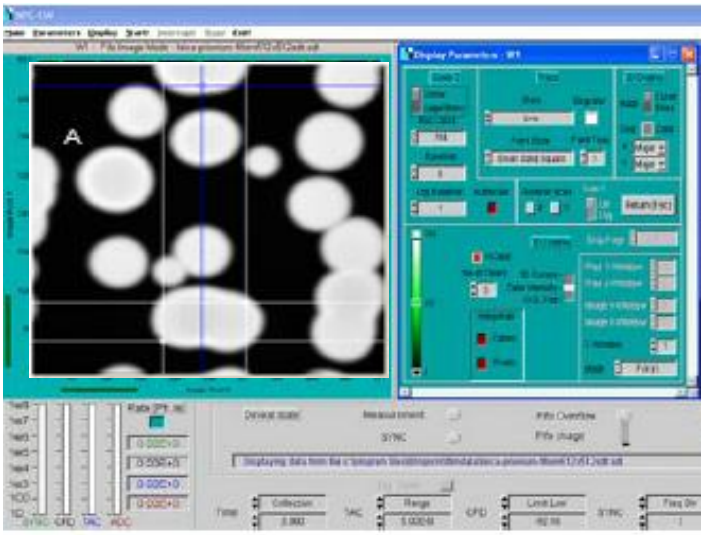

Figure 4-16 Data acquisition panel for the SPCM software. Intensity image in the 3-D display window at the top right, display parameter panel at the top left and control panel at the bottom.

The “Scan Sync In” mode is designed to create images from synchronised pulses from the scanner to the SPC module. The SPC module determines, for each photon or pulse, its arrival time and localisation within the scanning area. These values are accumulated in the memory and build up the photon distribution over X,Y and the fluorescence decay function.

Figure 4-16 shows the SPCM image obtained when a printed sample of the Rhodamine B dye in inkjet paper is observed under the instrument. It was scanned with 256 x 256 pixels, and 256 time channels per pixel. The average count rate over the image was 10^6 photons / s and the total acquisition time was 60 seconds.

The main panel shows the display parameters at the top right, the 3-D display window at the top left, and the count rate display panel at the bottom. The display parameter panel allows the user to define how the results will be shown, as well as the number of pixels in X- and Y-direction.

4.3.2.2 Data Analysis – The SPCImage software

The SPCImage software analyses the fluorescence lifetime imaging (FLIM) data by fitting it to a specific “model”. It is assumed that the decay can be fitted to a sum of exponential components.

The model function for each pixel allows the user to define the number of exponential components selected for the image, up to a maximum of three, but it is necessary to consider that the SPCImage can work only three components.

The fluorescence decay curve is fitted to a multi-exponential decay function, as defined by the following equation:

$$I(t) = B + \sum_i A_i \exp^{(-t/\tau)}$$ **Equation 4-10**

(where B is a constant to account for any background signal and A_i the fraction of the i^{th} lifetime component of the sample, τ_i is the fluorescence lifetime. ΣA_i is normalised to unity. A_i is the number of molecules emitting fluorescence with a lifetime τ_i.)

The fluorescence lifetime τ is determined by minimising the weighted sum of squares of residuals between the fitted function and the experimental data. This is known as least squares fitting and is done by minimising Equation 4-12.

$$\chi_a^2 = \sum_{i=b_1}^{b_2} \left\{ \frac{[I_0(t_i) - Y(t_i)]^2}{I(t_i)} \right\}$$ **Equation 4-11**

(where I_0 (t) is the background corrected intensity, Y (t) is the fitted function and I(t) is the uncorrected intensity. b_1 and b_2 are the first and last channels in the region of analysis respectively.)

The reduced chi-squared function, χ^2, gives an indication of the quality of the fitting procedure and the software minimises it automatically.

$$\chi^2 = \frac{\chi_a^2}{n_2 - n_1 + 1 - p}$$ **Equation 4-12**

(where p is the number of variable parameters in the fitting function.)

Theoretically a perfect fit has been achieved when χ^2 is 1 and higher or lower values mean either a poor fit or 'imperfect' data. In practice, the χ^2 value is used to judge whether adding a decay component gives a significant improvement in the fit to the data.

The goodness of fit of a decay curve can be verified by a plot of weighted residuals. The weighted residual values (r(t)), between experimental and fitted points are determined using Equation 4-14.

$$r(t_i) = \frac{I_0(t_i) - Y(t_i)}{\sqrt{I(t_i)}} \qquad \textbf{Equation 4-13}$$

Equation 4-14 does not take into account the instrument response function (IRF) for the experiment when attempting to fit the decay curve. The IRF is built up by the pulse–width of the laser (which is negligibly small for a femtosecond laser system), the electrical resolution of the TCSPC card and the transit time spread of the detector. This means that the experimentally measured intensity (I(t) is actually the convolution of the model function (F(t)) and the instrument response function (R(t)), such that:

$$I(t) = F(t) \otimes R(t - t_s) \qquad \textbf{Equation 4-14}$$

(where $\otimes$ is the convolution operation.)

The SPCImage software provides an estimation of this response function by calculating the first derivate of the rising part of the fluorescence response as shown in Figure 4-17 [20].

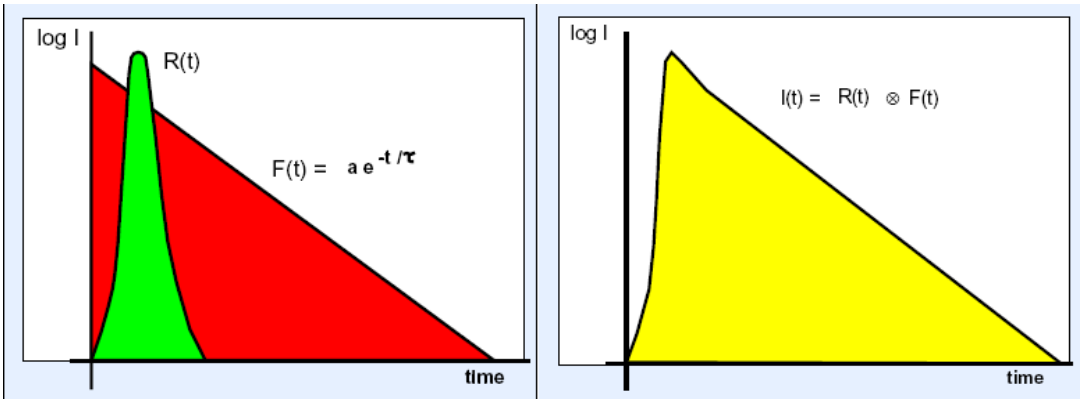

Figure 4-17 Convolution of the instrumental response function (IRF) with a single exponential decay trace [20].

The SPCImage software provides access to the lifetime information of a time- and spatially-resolved dataset measured with the TCSPC card and recorded by the SPCM software.

Figure 4-18 shows the SPCImage data analysis panel which corresponds to a sample of the Rhodamine B dye printed in an inkjet paper. It has an intensity image, a colour-coded lifetime image, a histogram of the lifetime over all the pixels, the decay curve at the selected pixel and its corresponding chi-square (χ^2), the fluorescence lifetimes components and the residuals plot. Due to the complexity of the structure of the inkjet papers studied here, the decay profile was not single but multi-exponential for most of the samples.

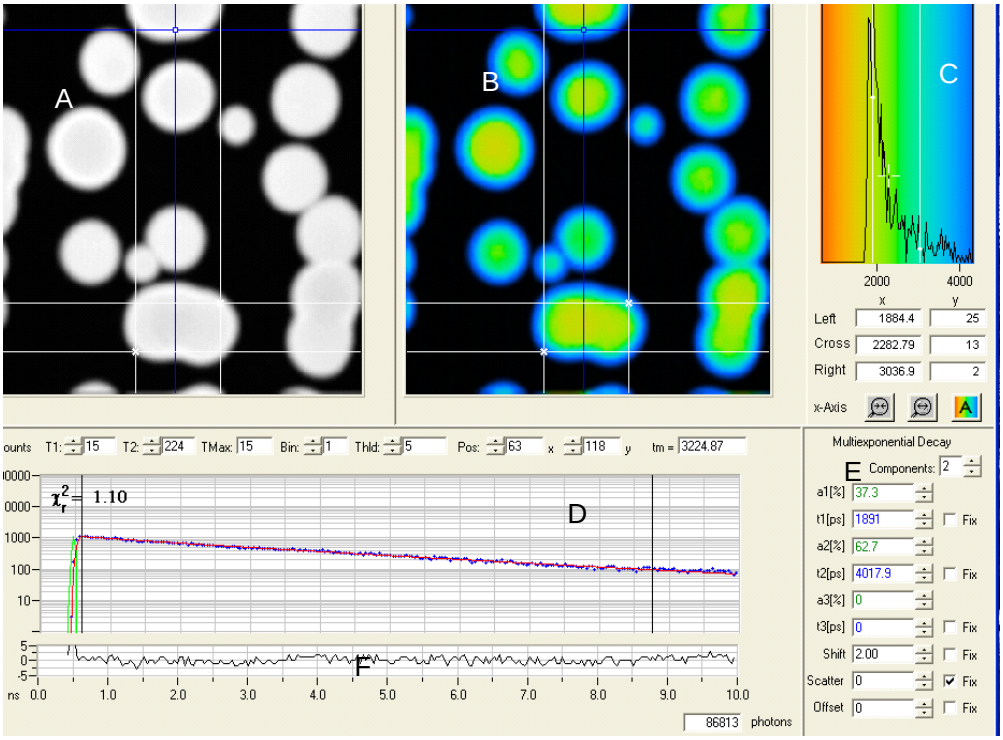

Figure 4-18 SPCImage data obtained for a sample of Rhodamine B printed in an inkjet paper; it has an intensity image (A), colour-coded lifetime image (B), a histogram of the lifetime over the pixels (C) and the decay curve at the selected pixel (D), the corresponding fluorescence lifetime (E) and the residuals (F). Lifetime range shown is between 1.8 and 3.0 ns. A PA x40 air Nikon objective was used, with a pulsed laser at 800 nm wavelength (λ), image size 512 x 512 pixels, 256 time channels and an average count rate of 10 ^{6}photons/s.

After loading the file, the software will indicate with a blue cross-hair the brightest pixel of the image. The location will be given as a numerical position (x,y) in the decay curve window described in the panel (D). The IRF, as explained above, is calculated automatically by the software from the data trace of the selected pixel. The selected pixel can be changed by moving the cross-hair. A defined region of interest (ROI) can be selected also by using two white cross-hair cursors. The decay curve shown in Figure 4-19 contains several numerical parameters such as the experimental photon decay data (blue), a trace of the fitted curve (red) and the instrument response function (green). The residuals graph at the bottom represents the deviations between the experimental and the fit curve.

The software will consider only the data between the two black lines in the graph for the fitting process and these positions are expressed numerically by the T_1 and T_2 values as shown in Figure 4-19.

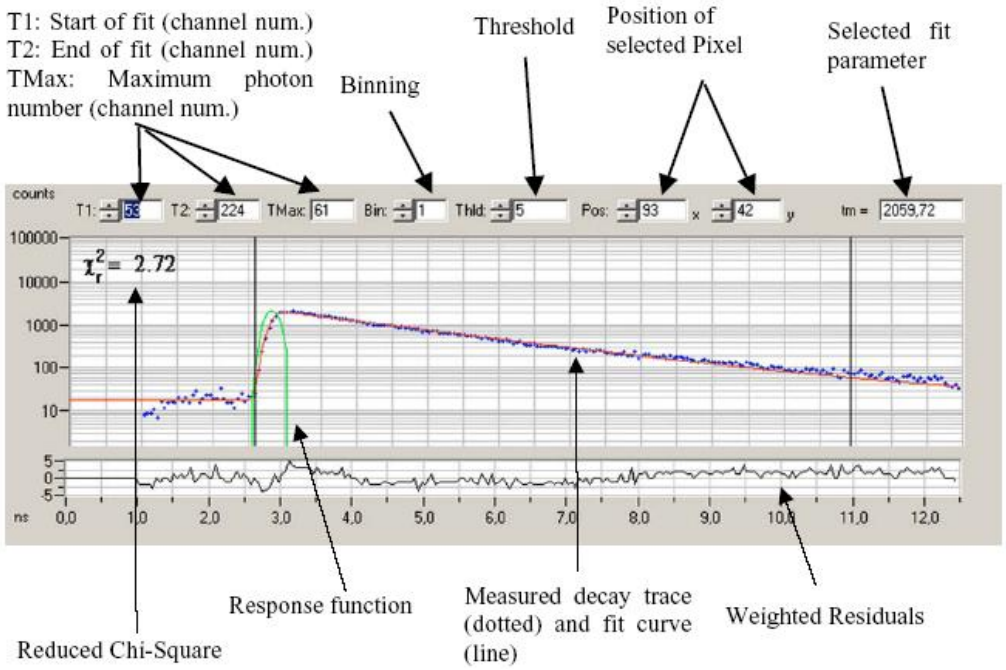

Figure 4-19 Decay curve graph with all the numerical parameters.

All the time channels in front of the first cursor are used to calculate the baseline or "offset". The τ_{max} value indicates the maximum of the fluorescence decay. The threshold-parameter defines the minimum number of photons in the peak of the fluorescence curve which are taken into account. The τ_m is the fluorescence lifetime average in the selected pixel as shown by Equation 4-15 and is the default parameter. There are many other parameters that can be selected such as the individual lifetimes (τ), the fraction of each component (A) and chi-square (χ^2).

The binning factor indicates the number of surrounding pixels considered for the decay trace. In general it is considered that the peak value of the curve should have a minimum value of 100 counts for a single exponential curve, about 1,000 counts for a double exponential curve and 10,000 counts for three exponents [20].

For the image analysis process of the region of interest the analysis is done pixel by pixel and line by line and the result is a colour-coded image of the fluorescence decay as shown in Figure 4-20. This image derives the intensity information from the number of photons in each pixel and the colour information from a selected fit parameter the value of which is coded by a continuous scale that runs from the red to the blue.

Next to the colour-coded image, a histogram is presented which shows the distribution of the parameter selected and the relative frequencies. Three white cursors (two vertical lines and one cross- hair) are provided to quantify the values given in the histogram. The cross-hair indicates the mean value of the distribution and the two white vertical cursor lines include 66% of all values found in the ROI. These numerical values are given below the histogram.

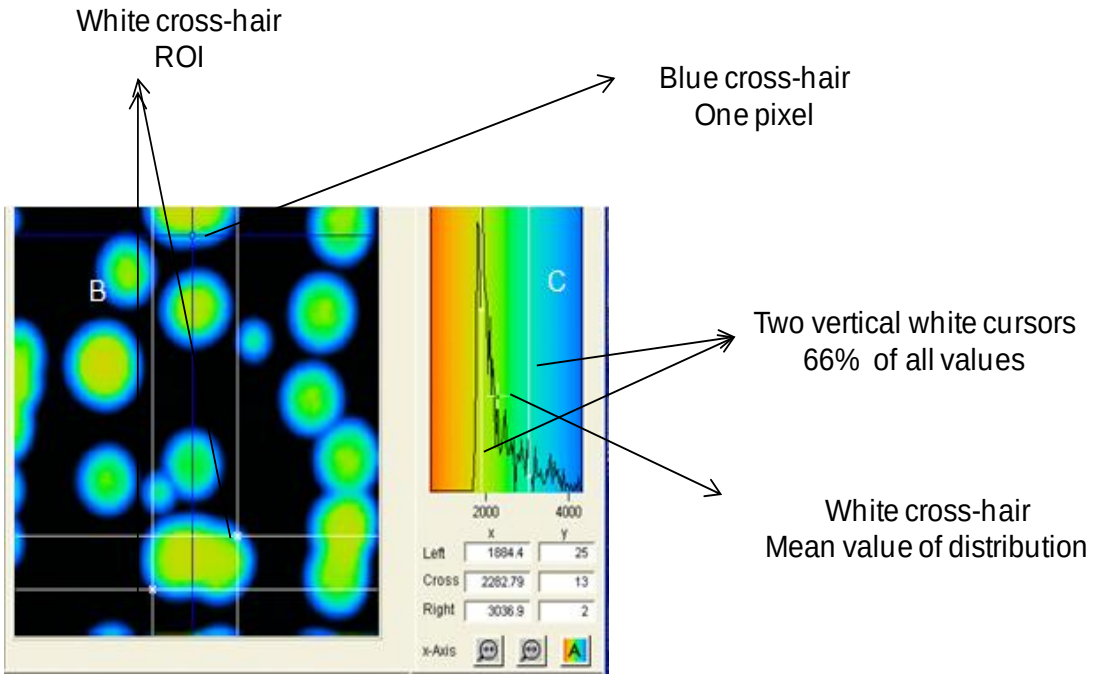

Figure 4-20 Colour-coded image and histogram for a Rhodamine B printed on an inkjet paper sample. Showing the blue cross-hair (one pixel) and two white cross-hairs selecting the ROI in the colour-coded image and the two vertical white cursors that contain 66% of the histogram values and cross-hair indicating the mean value of the distribution.

The default setting for the fit model is a single exponential decay which corresponds to the simplest model to analyse a FLIM image and if the value of χ^2 is around 1.4 or less, this is an acceptable model. If the χ^2 is higher than 1.4, it is necessary to consider a bi-exponential decay model and if necessary repeat the process for a three-exponent decay model.

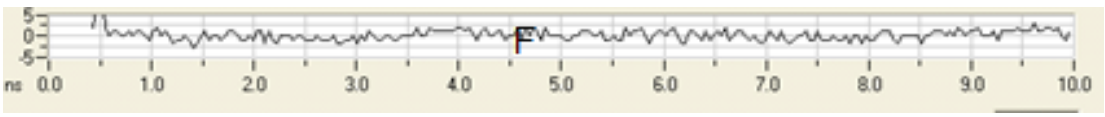

Figure 4-21 The residuals from fitting a bi-exponential decay curve to FLIM data for Rhodamine B dye printed on an inkjet paper sample.

The residuals plot, as shown in Figure 4-21, is an indication of the goodness of the fluorescence fitted curve. If the values of the peaks are not very high and the distribution looks random, it is a good fit.

5 Confocal Laser Scanning Microscopy of Inkjet Dyes

5.1 Introduction

Inkjet technology is one of the main digital imaging technologies used in homes and offices due to its print quality and affordable price. Inkjet prints must offer a large colour gamut, sharp detail rendering and long-term fastness properties [19, 21, 22]. As discussed in Chapter 1, the quality of an inkjet print depends on the technology of the printer, the properties of papers and ink, along with their physico-chemical interactions. Physical paper–ink interactions will govern the setting and drying of the ink whereas chemical interactions will influence the final attachment of dye to paper and therefore the light fastness or long-term stability of the prints. To achieve good quality prints, the formulation of the ink together with the coating of the paper, must tend to fix the dye close to the surface of the paper and make the drying process, or solvent absorption, very fast.

Although inkjet technology has developed rapidly over recent years, the fixation mechanism of the ink into the substrate is not completely understood. In this chapter, the intrinsic fluorescence of the inkjet dyes and papers is exploited in combination with confocal laser scanning fluorescence microscopy (CLSM) to measure the spread and penetration of dye droplets in different inkjet papers. With these aims several types of inkjet dyes and inkjet coated papers are analysed. The ability of the CLSM to optically slice the sample in z-direction and generate 3-D images that show the vertical and radial distribution of the dye inside the paper will be assessed as an approach to evaluate print quality.

5.1.1 Print quality

Inkjet technology is the fastest-growing technology in the printing industry [3]. The reason for this is that these printers can create high-quality photo images, at a reasonable price, with a resolution that exceeds the ability of the human eye to resolve it [1]. Therefore, understanding the factors that affect print quality is imperative. Inkjet printing quality is determined by the printer, the paper and the ink as explained above: the printer controls the ejection of the ink, the size of the droplet and the technology that creates secondary and

tertiary colours; the paper controls the absorption and fixation of the ink droplet; and the ink is responsible for producing the colour by selectively absorbing and scattering the light.

In this study a qualitative analysis of the print quality is done by studying the shape and size of the observed fluorescent ink dots, therefore the radial spread when printed. Sarafano [23] defined "dot fidelity" in terms of dot area and shape, and confirmed that these characteristics are essential in image analysis. In inkjet technology, colour images are formed by combinations of greyscale images of cyan, magenta, yellow and black. The greyscale images are formed by certain dot patterns and the faithful reproduction of the image will depend on the ability to reproduce print dots of the same size and shape. The theoretical dot shape produced by inkjet printers is circular, since the dots are obtained by impact of nucleated drops [24]. Consequently dot fidelity can be measured in terms of circularity and size [25].

To evaluate dot fidelity the roundness of the dot is calculated as a measure of the circularity of a dot and is defined as $4\pi A/p^2$, where A is the area and p is the perimeter of the dot. A good print quality requires circular dots [25] or values of roundness near to one which corresponds to a circle.

Another important measure of print quality is given by the absorption or fixation of the ink, since it is proved that ink penetration has a significant effect on the chroma and hue of the printed colours. Several studies, have concentrated on finding an appropriate method of measuring ink penetration with the purpose of developing the optimum paper coating–inkjet ink combination. The common way of measuring the depth of inkjet penetration is by cutting a thin cut or cross-section of the paper previously encapsulated in a resin, followed by the observation of the section under a microscope [26]; this is not only very time consuming and costly but it is also a destructive and intrusive method that can alter the results observed. Several methods have been investigated during recent years with the aim of finding a useful, non-destructive technique of measuring depth of penetrations as a tool for print quality evaluation and troubleshooting. Enomae et al. [27] analysed some paraffin-impregnated inkjet printed samples under a confocal laser scanning microscope and reported the three-dimensional distribution of the dye inside the paper and some values of depth of penetration, nevertheless the sample was impregnated with a substance that could affect the results. Yang [28] used experimental techniques together with theoretical simulations to study ink penetration effects on the reflection spectra. Vikman [29] studied the applicability of FTIR and Raman spectroscopic methods to understand the mechanisms that contribute to the light-

and water-fastness of inkjet prints. Lozo et al. [26] studied the applicability of confocal Raman, CLSM and Fourier-transform infrared in the analysis of penetration depth on diverse inkjet prints, concluding that despite the limits of all the methods used, the combined information is useful for the analysis of printed samples. The samples for the CLSM were immersed in oil and the depth profiles calculated were obtained from the orthogonal views; the depth of the ink relative to the surface of the paper was not determined.

5.1.2 Confocal Laser Scanning Microscopy (CLSM)

The fluorescence of some dyes and papers makes CLSM an attractive technique to investigate the behaviour of dyes within coated inkjet papers. Thanks to the ability of CLSM to optically slice the sample in the z-axis, a three-dimensional distribution of an inkjet dye can be acquired; high-contrast images are obtained, allowing the observation of the radial and vertical spread of the dye. For this study the intrinsic fluorescence of some dyes and paper components was exploited to obtain the three-dimensional ink distribution and depth profile without the need of adding fluorescent probes. One of the main advantages of this technique is that it is non-destructive, as fluorescence from inside the paper can be detected without affecting the sample; in addition, the analysis can be carried out over sizeable areas of the sample.

The aim of this study is to understand the behaviour of the ink when printed by investigating the spread and penetration of the ink inside the paper using CLSM.

The study in this chapter has been divided in three sections: Section 5.3 describes an image analysis of the dots in an xy plane or radial spread; Section 5.4 reports the study of the vertical penetration or depth profile; and Section 5.5 is a comparison of the *in situ* depth profile with the values obtained from a physical cross-section of the same printed sample. Microscopic and spectroscopic methods previously used in depth profiling by Enomae [27] and Lozo [26] did not give any information regarding the position of the dye with respect to the surface of the paper and neither considered the effects of the refractive index of the paper. Considering the fact that at the surface of the paper the light is reflected and exploiting the ability of the CLSM to detect the reflected light at the same time as the fluorescence, the surface can be located relative to the position of the dye. For this purpose a method was developed for the CLSM, with one detection channel to collect only reflected

light and another channel to collect simultaneously the fluorescence emitted by the ink. The surface of the paper was identified and localised by plotting a graph of intensity versus depth of the reflected image. It is known that the dye must be fixated, as near as possible to the surface of the paper, in order to achieve good print density images; therefore the localisation of the dye with respect to the surface of the paper is a measure of print quality.

5.2 Methods and Material

5.2.1 Confocal Laser Scanning Microscope

The Biorad 2000 CLSM assembled with an inverted Nikon T-300 microscope, described in Chapter 3, was the equipment employed in this study. A sample with dimensions of about 35 mm x 35 mm was cut from a print and placed in a metallic ring holder, specially manufactured for this purpose, with a clamp on top to hold the sample flat. As explained previously, care was taken when choosing the printer driver so as to print single dots of pure colour.

For radial spread imaging (Section 5.3) a method was created to visualise the fluorescence of the magenta dyes. The objective lens selected was a Nikon PA 20X dry with a numerical aperture (NA) of 0.75 with a resolution of 0.50 μm. All the magenta dyes were excited at 488 nm using an Argon laser and the emission was collected using a long pass filter above 600 nm (E600LP). Under these conditions and working with a 1.5 zoom, the xy pixel size is 0.8 μm and one xy-plane image corresponds to 411 μm x 411 μm. The thickness of each optical slice or resolution in the z-direction was 1.97 μm and the step chosen was 1.0 μm. The speed of laser scanning was 500 lines per second per single image of 512 x 512 pixels. All the images were scanned and averaged three times. Using this method, the magenta dyes were studied in terms of geometry, appearance and spreading. For this qualitative analysis, image binarization, count and measure of dots were performed using digital image analysis software in the public domain called Image J, which is a Java image processing software developed by Wayne Rasband and others at the National Institute of Health, USA [18].

For depth profiling (Section 5.4**)** a method involving two sequences was created; in the first one, the image is illuminated with a 457 nm laser (Ar) and through an open emission filter the reflected light is directed to PMT 1, in the second sequence the sample is excited with a 488 nm wavelength laser (Ar) and the emitted fluorescence is collected through a long pass

filter (E 600LP), above 600 nm in PMT 2. The objective lens used was a Nikon PA X 20 / NA 0.75 dry. A pinhole size of 1.0 was used which corresponds to the ideal value for these conditions giving a thickness of a single confocal plane or optical slice of 1.7 μm and the step between slices was 1.0 μm. Under these conditions and working with a 1.5 zoom, the xy pixel size is 0.8 μm and one xy-plane image corresponds to 411 μm x 411 μm. The speed of laser scanning was about 500 lps per single image of 512 x 512 pixels. All the images were scanned and averaged three times. The step used to record the optical slices was 1 μm. The software used to measure depth profile was Image J [18].

For the measurements of physical cross-sections of different prints (Section 5.5), the method created consisted of two sequences; the first illuminates the sample with the 457 nm laser and collects the transmitted light in PMT 1 and the second one excites the dye at 543 nm and collects the emitted fluorescence, through a long pass filter (E 600LP), above 600 nm in PMT 2. The objective lens used was a Nikon PA X 20 / NA 0.75 dry. Under these conditions and working with a 1.5 zoom, the xy pixel size is 0.8 μm and one xy-plane image corresponds to 411 μm x 411 μm. The speed of laser scanning was about 500 lps per single image of 512 x 512 pixels. All the images were scanned and averaged three times. The depth profile was measured through the line profile availability of Image J [18] .

5.2.2 Materials

5.2.2.1 Inkjet inks and dyes

The inkjet inks were prepared by Fuji Film Imaging Colorourants (FFIC), using water-soluble dyes. The molecular structures of most of them are not in the public domain. The formulation of the ink consists of a solvent, in this case water, and small amounts of other additives as explained in Chapter 1. These additives are formulated to control factors such as: dot gain, drop formation, print-head corrosion, pH, light and water resistance, and colour intensity.

For the present report only magenta dyes were studied. Table 5-1 shows the dyes used for radial-spread studies (Section 5.3).

Dye	FFIC Ref	Colour
1	Ar52	Magenta
2	192332/2	Magenta

Table 5-1 Dyes used in radial-spread studies.

Table 5-2 shows the dyes used in depth-profiling studies (Section 5.4).

Dye	FFIC Ref	Colour
1	Ar52	Magenta
2	S192332/2	Magenta
3	S071397	Magenta
4	S155198	Magenta
5	S192164	Magenta

Table 5-2 Dyes used in Section II.

In the physical cross-sections only one dye, the magenta-OAM was analysed.

5.2.2.2 Inkjet papers

All the papers used in this study were coated inkjet papers manufactured with a series of layers; the ink-receiving layer, followed by the barrier, the cellulose, the back barrier and finally the back-coat layer with the exception of the plain paper used for the physical cross-sections.

For imaging of radial spread, the two main types of inkjet coating were studied, the microporous and swellable type of paper. Additionally, two different microporous papers were considered, silica and alumina-based papers, these being the most common type used.

Table 5-3 lists the different inkjet papers studied.

Paper	Type	Number of layers	Composition of ink-receiving layer
A	MICROPOROUS	5	40 µm Alumina + trace organics.
B	MICROPOROUS	4	37 µm Silica + polythene binder with traces of alumiunium.
C	MICROPOROUS	4	35 µm Silica + polythene binder.
D	MICROPOROUS / SWELLABLE	5	Gelatin + silica (no thickness given).
E	SWELLABLE	UNKNOWN	N/A

Table 5-3 Coated inkjet papers used in radial imaging.

The depth of penetration was measured in two types of paper, the microporous and the swellable listed in Table 5-4.

Paper	Type	Number of layers	Composition of ink-receiving layer
B	MICROPOROUS	4	37 µm Silica + polythene binder with traces of aluminium.
F	SWELLABLE	4	30 µm Acrylate + a polyether.

Table 5-4 Coated inkjet papers used in depth profiling.

The cross-sections analysed were produced from prints of papers listed in Table 5-5.

Paper	Type	Number of layers	Composition of ink-receiving layer
A	MICROPOROUS	5	40 µm Alumina + trace organics.
B	MICROPOROUS	4	37 µm Silica + polythene binder with traces of alumiunium.
G	PLAIN		

Table 5-5 Coated inkjet papers from which physical cross-sections were prepared.

5.2.2.3 Printed samples

There is a great variety of printers, papers and inkjet inks available in the market. The purpose of this study was to evaluate dye-based inkjet inks printed on various types of commercially available inkjet paper. The printing was done in the FFIC laboratory in advance so all the prints analysed were settled and completely dry.

5.2.2.4 Printing considerations

The printer used was a Canon S800, a colour bubble digital inkjet printer, with a print head containing 1.536 (256 x six colours) nozzles and a 2,400 x 1,200 dpi resolution. The patches were all printed under the same conditions using special software (property of FFIC) that guarantees only one colour on the print, not a mixture of colours. The patches analysed were printed with primary magenta with a colour intensity of 10 % and 100 % as shown in Figure 5-1. In the 10 % colour intensity patch the individual dots are visible under the CLSM.

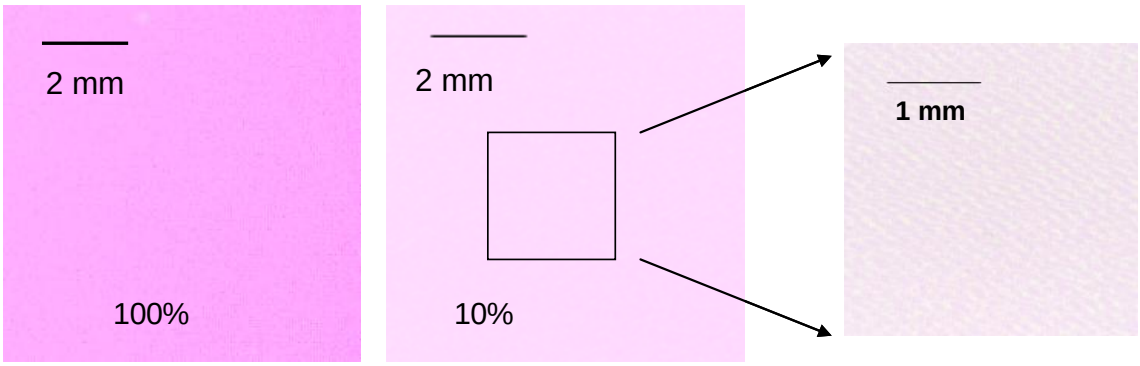

Figure 5-1 Schematic of 100% and 10% colour intensity samples.

5.3 Radial spread of inkjet dots

In this Section, the radial spread of the inkjet droplet on the paper is analysed in terms of shape and size of the formed dots. Two magenta dyes, the Ar52 and S19232/2, printed in five different papers (A, B, C, D and E) were studied (Table 5-1 and 5- 3). The fluorescence spectra of the dyes are given in Appendix I.

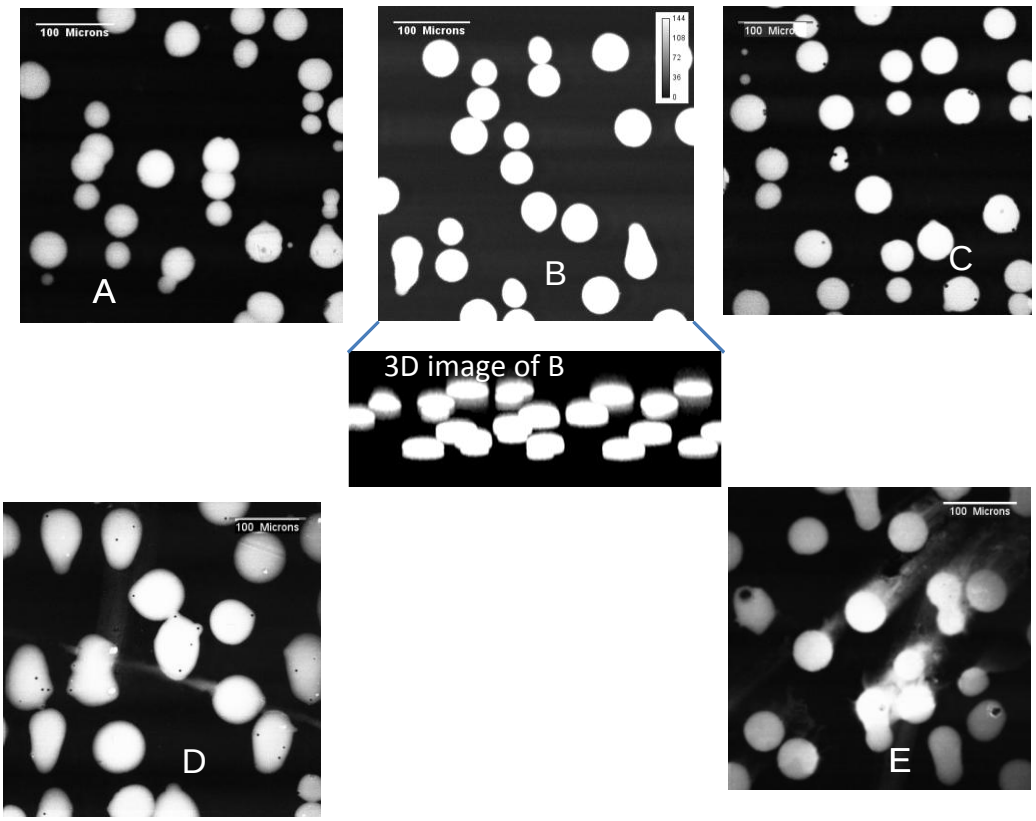

Figure 5-2 Ar52 ink printed on five different coated inkjet papers. A, B, C, D, E and 3-Dimensional projection of image in paper B.

Figure 5-2 shows CLSM images obtained for samples of 10% colour intensity of Ar52 ink printed on five inkjet papers using the method described previously. It can be observed that the Ar52 dye is absorbed in a very homogeneous way in the microporous types of papers A, B and C, forming very well-defined and sharp dots with a "coin shape" [27]. The colour distribution or intensity in each dot is uniform suggesting an even spreading of the dye in the ink-receiving layer. The ink appears to have been properly formulated for these papers, as dots maintain a circular geometry, after the medium has been absorbed, indicative of a good ink quality. In papers D and E the dye shows a greater radial spreading, making the edge transition not very sharp. This can produce fuzzy images [25] and can be the consequence of both chemical and physical properties of the coating molecules of these two papers and their reaction with the dye. These papers have swellable character, and therefore dyes and ink medium are absorbed by a different mechanism which seems to prevent the droplet from settling uniformly. The contrast in these papers will not be as good as in the microporous papers.

Figure 5-3 shows CLSM images obtained for samples of S192332/2-based ink printed in the same five inkjet papers. The dot edges for papers A, B and C are well defined, while in papers D and E some dots look incomplete. This can be caused by bigger or aggregated particles of the coating that prevent the dye from occupying the precise location. It is interesting to note that although papers B and C have a silica-type ink-receiving layer and have been printed under the same conditions, they behave differently in terms of edge roughness. This is because several types of silica are used for ink-jet papers, such as colloidal silica, fumed silica, fused silica, precipitated silica, silica gel and high-purity ground silica, differing mainly in pore volume, pore distribution and pore diameter [3]. The results shown in Figure 5-2 and 5-3 proves that the ink-receiving layer of these two papers is manufactured with different types of silica.

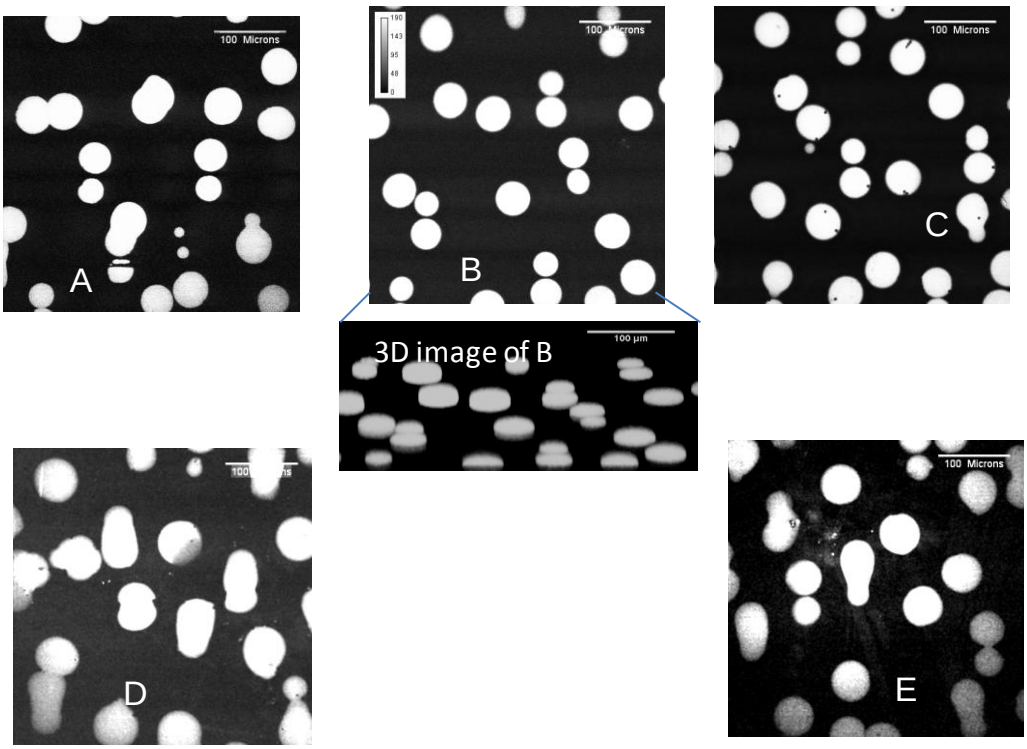

Figure 5-3 S192332/2 ink printed on different coated inkjet papers. A, B and C are microporous; D and E have swellable character.

The images obtained for both inks are similar. In the microporous papers, the dots are well defined, round and bright, which suggest that a good print quality would be obtained with papers A, B, and C. In papers D and E, the dots have better defined edges with S192332/2 ink than those obtained with Ar52. The bright, small and round dots observed in Figure 5-2 and 5-3 confirm that the smallest dot that can be obtained from an inkjet printer is circular,

as expected as a result of the impact of a spherical nucleated drop on the surface of the paper [24]. The average dot area, perimeter, diameter and roundness of dots in the images were calculated by converting the images first, into a binary image (Table 5-6) and then measuring the dots using the Image J software.

All the complete dots (approximately 20) were selected from each image and the average area, diameter, perimeter and roundness were calculated as shown in Table 5-6 for both dyes printed on five different inkjet papers. Roundness, R, is a measure of the circularity of a dot and is defined as:

$$R = \frac{4\pi A}{p^2}$$ **Equation 5-1**

(where A is the area and p is the perimeter.)

For a circle:

$$R = \frac{4\pi(\pi r^2)}{(2\pi r)^2} = 1$$ **Equation 5-2**

A good print quality requires circular dots [25]; if the value of roundness is near one, the dot shape is very close to a circle.

The best values of roundness are obtained for papers B and C for the Ar52 ink and A, B and C for the S192332/2 ink. In the case of S192332/2 ink in paper D, it seems that the dots are overlapping each other and this is the cause of the low value of R obtained.

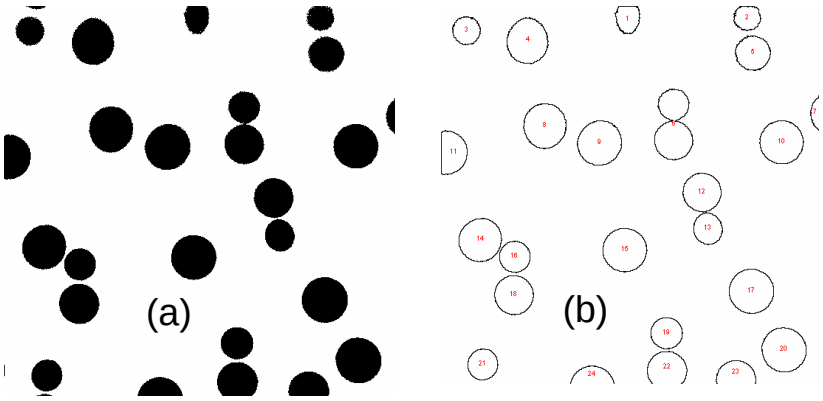

Figure 5-4 Image processing for determining dot area and perimeters (a) Binary image (b) Processed image for extraction of parameters in Table 5-6.

Dots printed on commercially available inkjet papers (same resolution), with silica as the coating pigment, have been reported to have an area between 1400 to 1700 μm ^{2} when analysed under a CLSM [30], which is in accordance with the data obtained in our analysis (1400–1500 μm ^{2}) for papers B and C with both inks.

Paper	Dye	Area μm^2	Perimeter μm	Diameter μm	Roundness
A	Ar 52	1115	184	37	0.41
B	Ar 52	1420	141	42	0.90
C	Ar 52	1439	146	42	0.85
D	Ar 52	2990	240	62	0.69
E	Ar 52	1887	227	49	0.46
A	S192332/2	1570	152	44	0.85
B	S192332/2	1381	142	41	0.86
C	S192332/2	1538	150	44	0.86
D	S192332/2	2405	340	55	0.32
E	S192332/2	1944	247	49	0.40

Table 5-6 Average area, perimeter, diameter and roundness of printed dots obtained for Ar52 and S192332/2 dye inks.

Although the dots in silica- and alumina-coated microporous papers, with both dye-inks, present a much more circular shape, their diameter is not uniform, which means the spreading of the dots is being affected by other factors, which could be the roughness or porosity of the coated paper [28], the viscosity or the surface tension of the ink [24].

Papers A and C show some very small dots which are considered as “inkjet spray”, and are caused by the breakage of the droplet when leaving the nozzle [31]. This inkjet spray or “satellite dots” are described by Bohorquez [24] as small unwanted spots near the printed zone, that cause distortion of the images. They are currently under investigation at the Inkjet Research Centre at the University of Cambridge [2] as they are an important issue in inkjet quality.

In summary, it has been found that the dot behaviour is highly dependent on the paper coating. Print quality for these two dyes, evaluated in terms of contrast, roundness and consistency, proved to be better in the microporous papers A, B and C.

5.4 Depth profile measurement

CLSM is not only useful for radial-spread analysis, because its ability to optically slice the samples provides information of the ink fluorescence inside the paper, but also provides information about the position of the dye with in the paper. This section is focused on measuring the distribution of the dye inside the paper. It is desirable that the dye remains, as close to the surface of the paper as possible, to reflect the light and create a good-quality image [24]. Consequently it is important not only to establish the thickness of the dye layer within the paper but to also determine its position relative to the surface of the paper. As described in Section 5.1.2, the surface of the paper could be located by reflectance imaging.

5.4.1 Validation of fluorescence depth profiling

To measure the depth profile of ink in the paper, the intensity of fluorescence as a function of depth is determined from a z-stack of confocal images. However, the measured intensity profile will not correspond to the distribution of ink if the fluorescence intensity falls off with depth due to re-absorption and/or scattering of the emitted light or attenuation of the excitation light as it passes through the sample.

Therefore to validate the method, test measurements were made on a hollow rectangular cross-section borosilicate capillary, with a depth similar to that of most of the inkjet-receiving coating layers, filled with an aqueous solution of inkjet dye. The dimensions of the capillary are shown in Figure 5-5 and the solution used was a 1.6×10^{-4} M Ar52 in water.

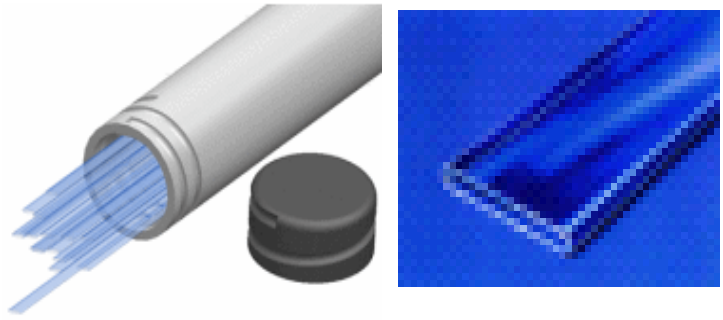

Depth	40 µm
Width	400 µm
Length	50000 µm
Wall thickness	40 µm
Tolerance	10%

Figure 5-5 Photographs (A and B) and dimensions of borosilicate rectangular capillaries (C) with 10 % of tolerance in the measurements.

Figure 5-6 shows the total field of view of an optical slice of the capillary filled with Ar52 solution. For the study only a small part of the image was analysed to avoid errors due to possible imperfections or bending of the capillary walls.

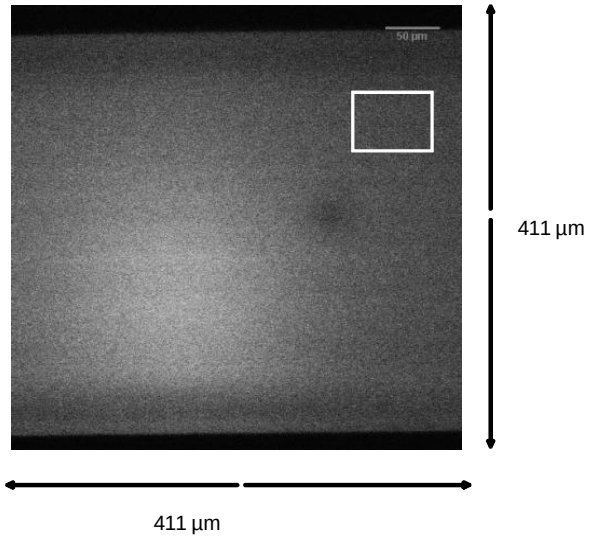

Figure 5-6 Fluorescence image of Ar52 solution in the capillary observed by a PA 20 objective; the area over which the depth profile was measured is indicated.

From the optical slices recorded, a graph of the fluorescence intensity versus depth of penetration (z-axis profile) can be plotted using Image J, as shown in Figure 5-7.

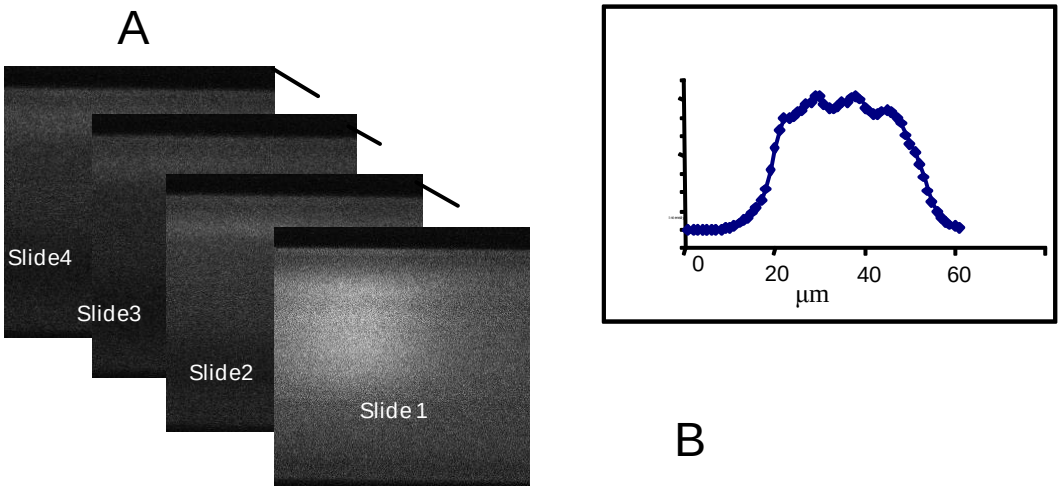

Figure 5-7 Optical slices obtained with the CLSM for a solution of Ar52 in a rectangular capillary (A) and a plot of intensity versus depth of penetration within the capillary (B).

The intensity profile shows steep rising and falling edges corresponding to the walls of the capillary, but it is not quite flat topped; there is a slight fall of intensity with depth across the top of the profile. Figure 5-8 shows an orthogonal view, obtained with the Ortview plug-in [32] from Image J, of fluorescence in XZ and YZ plane. Some distortion can be observed as expected at the walls of the micro slide.

The fluorescence collected along the z axis shows a penetration of 40 µm approximately, which corresponds to the whole depth of the slide, confirming that there is no loss of fluorescence when working at this depth under these conditions.

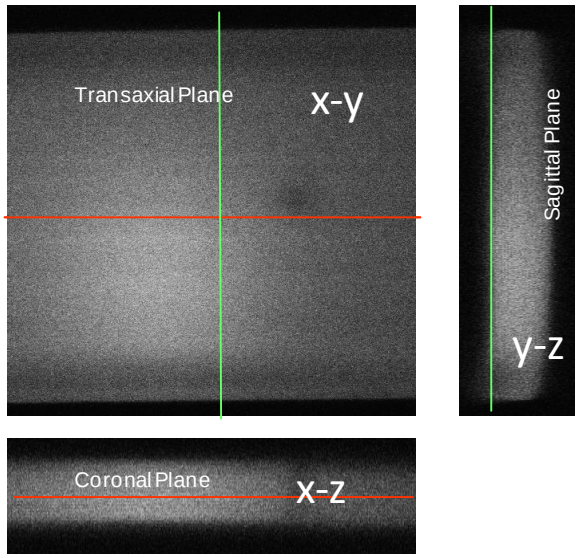

Figure 5-8 Orthogonal views obtained with Image J of an Ar52 solution in a 40 µm depth slide.

To overcome this possible distortion, only a small central section of the image is considered for the purpose of this experiment as shown in Figure 5-9.

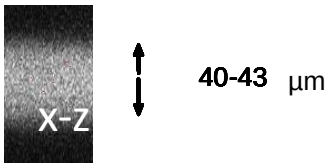

Figure 5-9 Fluorescence intensity in XZ plane of capillary with Ar52.

From the z-profile (Figure 5-10) the FWHM obtained was 28.8 µm. However, this needs to be corrected to take account of the difference in refractive index between water (n=1.33) and air (n=1.00). When the correction factor of 1.33 is applied, the FWHM obtained is 38.3 µm which is in accordance with the depth of the capillary reported as 40 µm +/- 10%.

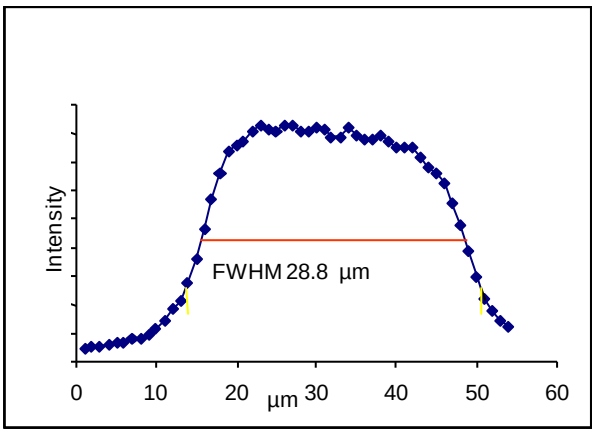

Figure 5-10 Uncorrected Z-axis depth profile (intensity versus depth in µm) of an Ar52 solution in a (40 µm depth) rectangular capillary.

Having confirmed that the fluorescence intensity is conserved over a depth similar to that of the ink-receiving coating layer of the paper and the FWHM of the intensity profile is a good measure of depth, the next step is to measure the depth of penetration of different dyes within inkjet papers.

5.4.2 Depth of penetration of ink in paper

A sample of Ar52 ink printed in paper B was analysed under the CLSM with the aim of determining the depth of penetration of the dye within the paper. The method used in the CLSM was explained in section 5.2.1 of this chapter, the magenta dye was excited at 488 nm and the fluorescence emitted was collected above 600 nm. With the purpose of identifying

the position of the surface of the paper at the same time as localising the dye within the paper, a reflection image was recorded as well as a fluorescence intensity image. Figure 5-11 shows the reflection image (a) and fluorescence intensity image (b) of a 100% colour-intensity print of Ar52 dye ink printed in paper B. The reflection image is bright at the surface allowing the observation of some imperfections of the paper. The intensity of the ink fluorescence observed at this location is not uniform, which could suggest that there are some parts of the coating layer that absorb more ink than others. This phenomenon could be what is called "mottle" [24] and is considered as a cause of quality printing defects.

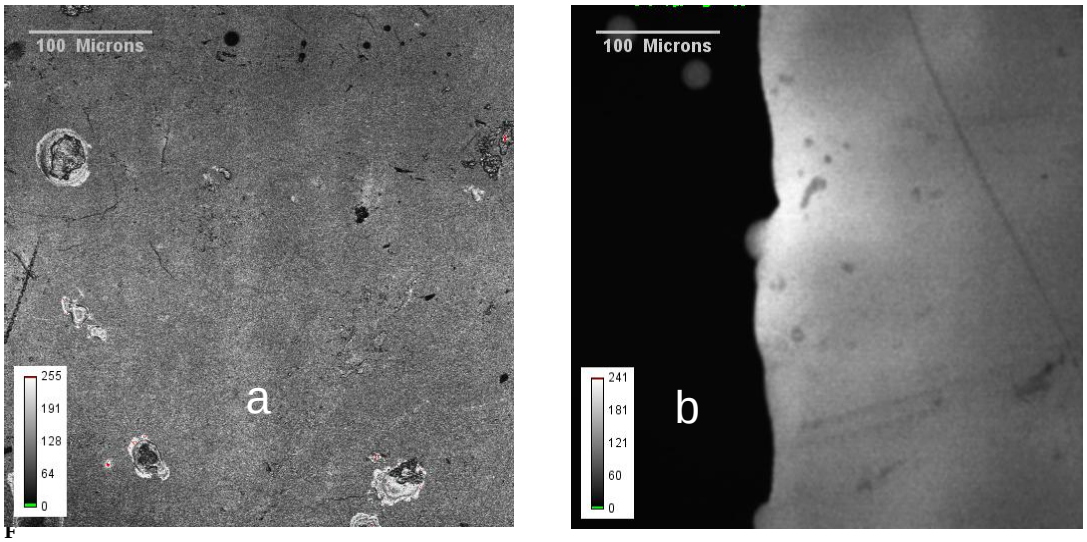

Figure 5-11 View of a full-tone printed patch of Ar52 printed in paper B. (a) Reflection image showing paper surface; (b) Fluorescence image showing the dye.

The stack of optical slices obtained when the sample is scanned in the z direction recreates the way the ink penetrates the paper.

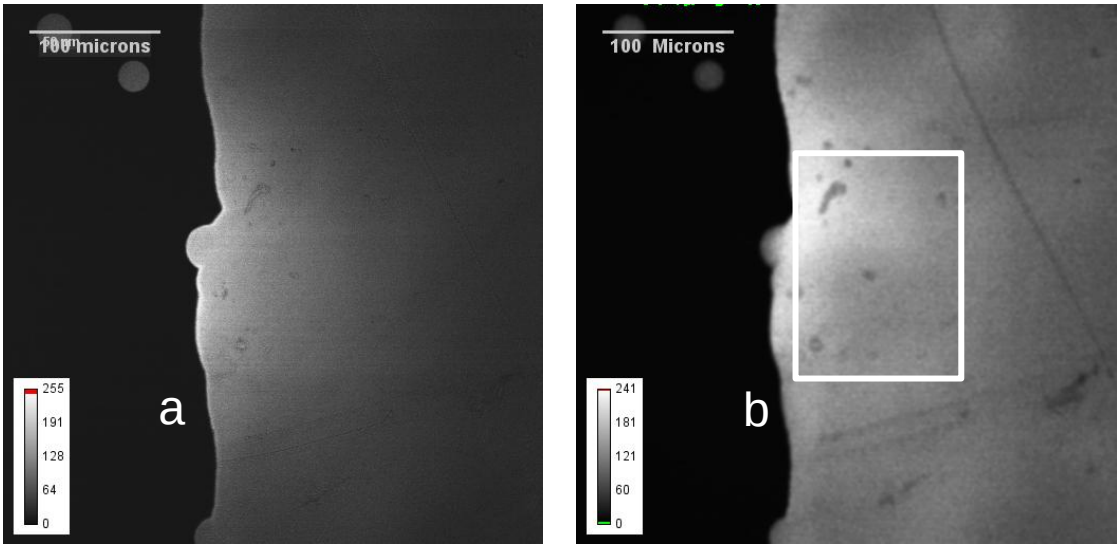

Figure 5-12 Fluorescence emitted at the surface of the paper (a) and fluorescence emitted 6 µm deeper within the paper (b) showing the region of interest (ROI) analysed.

Figure 5-12 illustrates how the dye distribution changes as it penetrates the paper. At the surface of the paper the dye is mainly located at the edge of the printed patch, where the printer starts each row, while at approximately 6 µm from the surface the fluorescence image with maximum intensity is observed which suggests that the majority of the dye settles in this region.

A three-dimensional projection can be created with Image J, as shown in Figure 5-13, illustrating the uniformity of penetration.

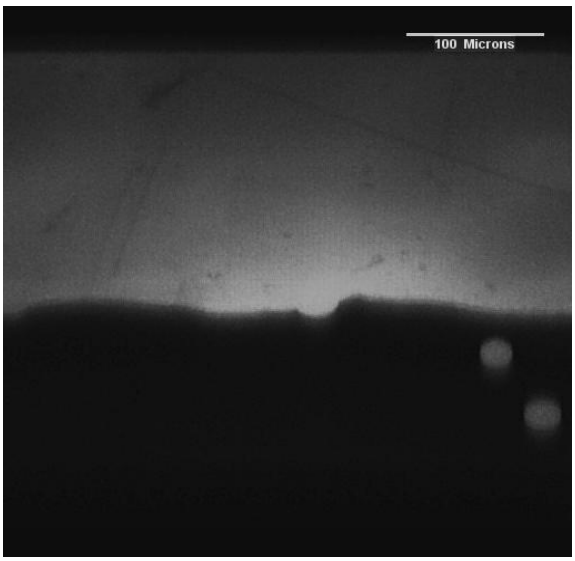

Figure 5-13 Three-dimensional projection of Ar52 print (Mirror image of Figure 5-12).

To measure the depth of penetration of the dye within the paper, the depth profile of the fluorescence and reflection image are plotted as shown in Figure 5-14. The area over which depth profiles are measured (ROI) is shown in Figure 5-12b. The position of the maximum fluorescence intensity can be established with respect to the position of the maximum intensity of the reflection image, a measure that corresponds to the distance between the surface and location of the majority of the dye. Paper B represents a special case as the reflectance depth profile (Figure 5-14) shows a second peak at approximately 30 µm from the first one, possibly indicating the position of the boundary of the second layer of the paper as indicated in its structure in Appendix II. It is interesting to note that the dye is contained between these two peaks, corresponding to the first layer of the paper or ink-receiving layer.

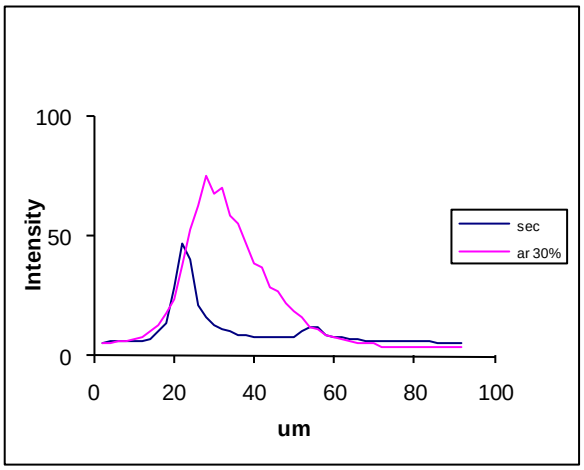

Figure 5-14 Plot of fluorescence intensity recorded from an Ar52 dye print in paper B (pink) and intensity of reflected light from the same paper (blue).

Figure 5-15 shows a reflection and a fluorescence image together with the XZ section of both images cut at the position indicated by the red line. The XZ sections illustrate that the emitted fluorescence lies between the two intensity lines observed for the reflected image in Figure 5-14.

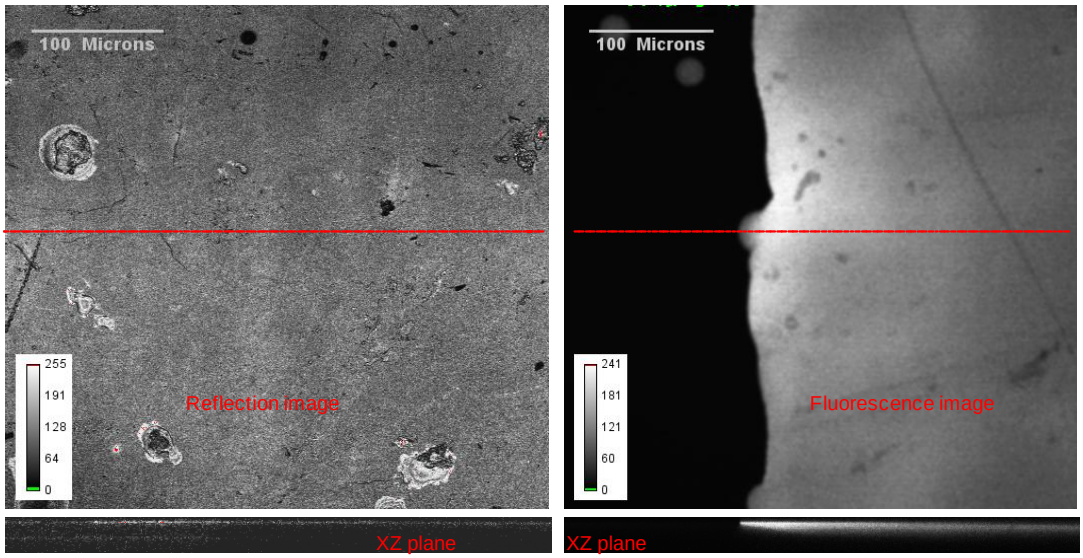

Figure 5-15 View of a full-tone printed patch of Ar52 printed in paper B. a) Reflection image and an XZ section b) Fluorescence intensity image and an XZ section. XZ sections are cut at the position indicated by the red line.

For this study the dye penetration is defined as the full width half maximum (FWHM) of the depth-profile curve. In order to find if the amount of ink printed influences the depth of penetration, three samples printed with the same dye-ink, in the same paper, but with different amounts of ink, were studied. The three samples had 100, 50 and 10% colour intensity.

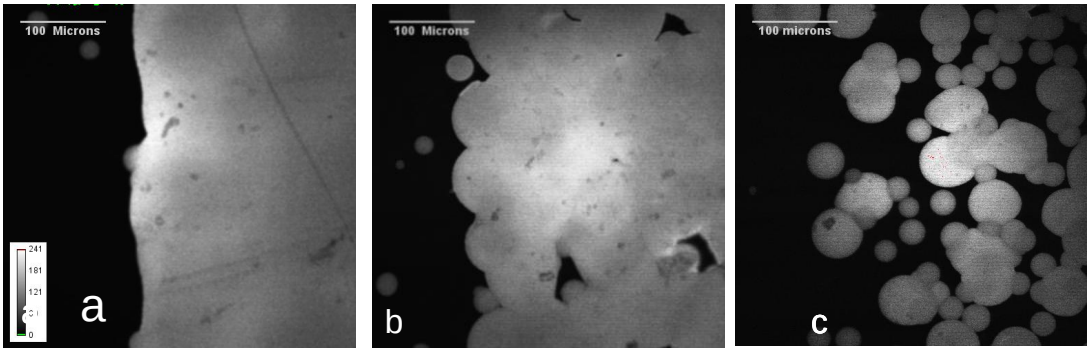

Figure 5-16 Ar52 printed in paper B at different concentrations: (a) 100%, (b) 50% and (c) 10% colour intensity.

The fluorescence intensity images obtained for these samples are shown in Figure5-16. As expected, in the 10% colour-intensity sample, the individual dots are visible while in the 100% the whole region is covered with ink.

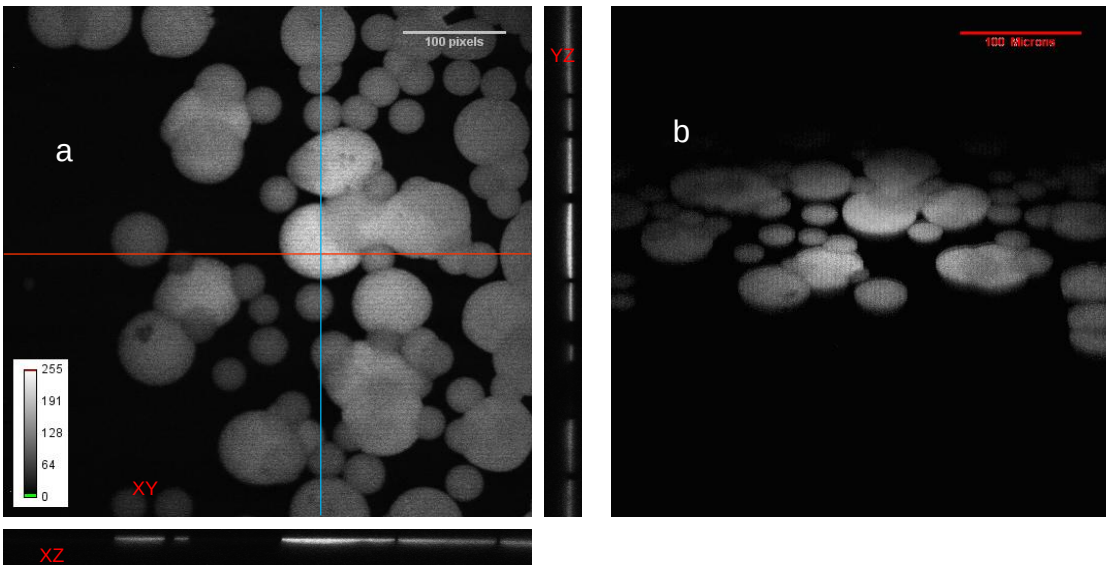

Figure 5-17 Orthogonal views (a) and 3-D projection (b) of Ar52 printed in paper B.

The depth of penetration of most of the dots is uniform as observed in the orthogonal sections and the 3-D projection of the Ar52 print in Figure 5-17.

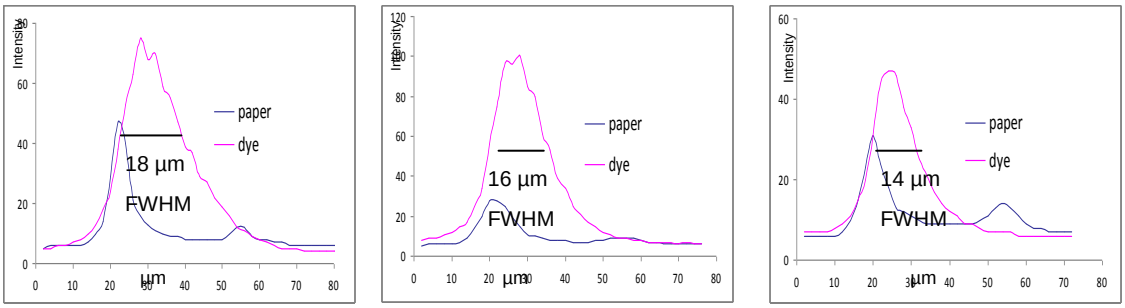

Figure 5-18 Depth profiles of Ar52 ink printed in paper B at the three different colour intensities (a) 100%, (b) 50% and (c) 10% with the corresponding FWHM.

The depth profiles obtained for these printed areas are shown in Figure 5-18 together with the values of the FWHM for each one. The depths of penetration (FWHM) obtained are in accordance with the data reported by Enomae [27] of 15 µm for commercial inkjet papers using silica as the pigment and 14.8 µm obtained by Lozo [26].

The value of the FWHM is a good measure of depth of penetration when comparing behaviour of dyes in different papers but to obtain a more realistic measure of penetration it is necessary to take into account that, in the printed samples, the light has to travel through a complex substrate, the paper, with a refraction index different to the refraction index of the air, distorting the angle of the light.

Paper	Colour Intensity	FWHM	FWHM*	Distance between ink and surface
		μm	μm	μm
	%	-/+ 2 μm	-/+ 2 μm	-/+ 2 μm
B	30	18	25.0	8
B	20	16	22.2	10
B	10	14	19.5	6

Table 5-7 FWHM of depth profiles obtained for three samples of Ar52 ink on paper B at three different colour intensities; at three different concentrations, FWHM* corrected for refractive index of paper (n=1.39); and the distance between the maximum fluorescence intensity of ink and the surface of the paper.

Bakker et al. [33] studied the refraction index (n) of different inkjet dyes printed in coated inkjet papers, using spectroscopic ellipsometry, and reported a refractive index (n) of 1.39 for magenta dyes absorbing light at 488 nm. If the value of the FWHM is corrected by the rate of difference in the refraction index (1.39 / 1.00), a more realistic measure of depth of penetration is obtained and is shown in Table 5-7.

The same study was performed with a swellable type of paper, F, and the fluorescence images collected for these samples are shown in Figure 5-19.

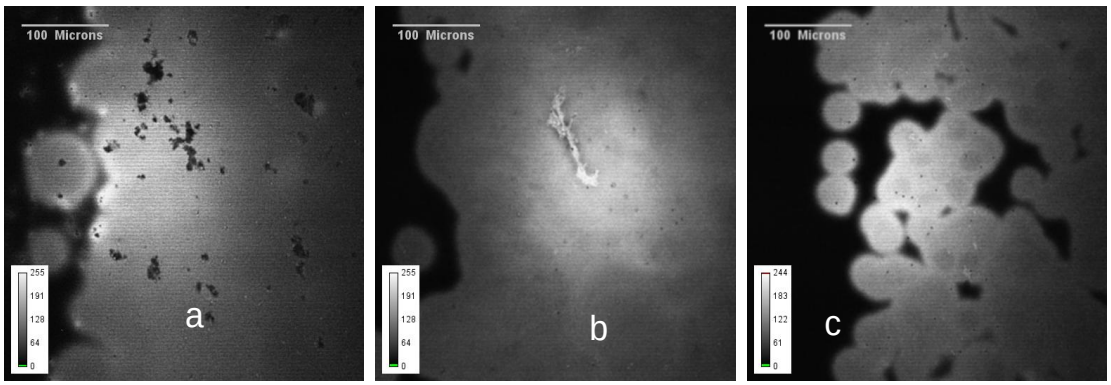

Figure 5-19 Ar52 printed in paper F at different concentrations: 100% (a), 50% (b) and 10% colour intensity (c).

In contrast to the behaviour observed for the microporous paper, the depth of penetration of Ar52 ink in paper F does not change with concentration as shown in Figure 5-20. Additionally comparing the data obtained from the two papers, it can be observed that the penetration in paper B, or microporous paper, is higher than in paper F. However, the

maximum fluorescence peak of the dye in paper F is nearer to the surface of the paper which means that the dye in these samples is closer to the surface, ensuring good colour images.

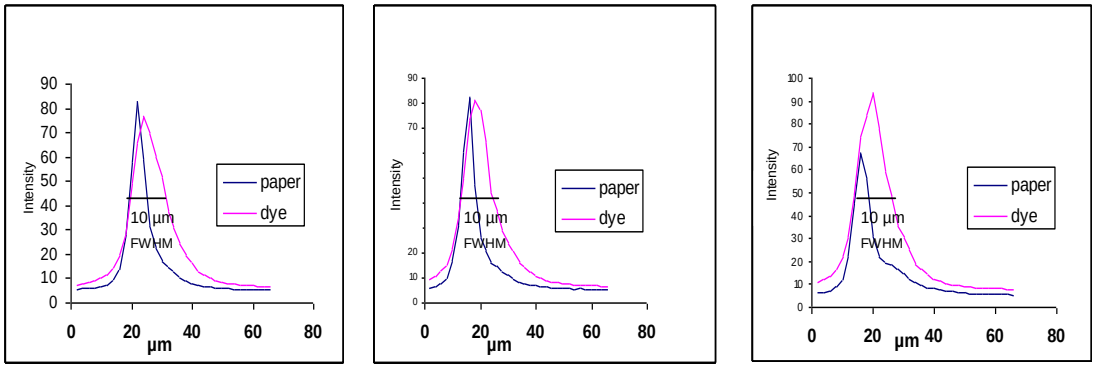

Figure 5-20 Depth profiles of Ar52 ink printed in paper F at three different concentrations.

The depth of penetrations in terms of FWHM and the position of the dye with respect the surface of the paper are summarised in Table 5-8.

Paper	Colour Intensity %	FWHM µm -/+ 2 µm	FWHM* µm -/+ 2 µm	Distance between ink and surface µm -/+ 2 µm
F	30	10	13.9	2
F	20	10	13.9	2
F	10	10	13.9	2

Table 5-8 FWHM of depth profiles obtained for three samples of Ar52 ink on paper F at three different colour intensities, FWHM* corrected for refractive index; and position of the maximum fluorescence intensity of the ink with respect to the surface of the paper.

The same experiment was performed with four other dyes (Table 5-2) and the depths of penetration obtained together with the position of the maximum ink fluorescence peak, with respect to the surface of the paper, are shown in Table 5-9.

Dye	Paper	FWHM*	Distance between	FWHM*	Distance between
Colour intensity		10%	ink and surface	100%	ink and surface
		+ / - 1.39 µm	µm	+ / - 1.39 µm	µm
Ar 52	B	19.5	6	25.0	8
Ar 52	F	13.9	2	13.9	2
S174744	B	16.7	4	16.7	2
S174744	F	13.9	2	11.1	2
S071397	B	16.7	4	22.2	6
S071397	F	13.9	2	12.5	2
S155198	B	16.7	4	22.2	4
S155198	F	13.9	2	11.1	2
S192164	B	16.7	4	19.5	4
S192164	F	16.7	0	13.9	2

Table 5-9 FWHM of depth profiles obtained for five different magenta dye ink samples at two different colour intensities: 10% and 100%, FWHM* corrected for refractive index; and position of the maximum fluorescence intensity with respect to the surface of the paper.

The depth of penetration is slightly higher in the microporous paper than in the swellable paper but in the swellable paper the dye is fixated nearer to the surface. The ink layer of most of the dyes printed at 100 % colour density, in the microporous paper, is between 20 to 25 µm with the exception of the S174744 dye that showed an ink-layer thickness of 16.7 µm. Nevertheless the ink layer thickness obtained for all the dyes when printed, in the same paper at 10 % colour intensity, was very similar with a value between 17 to 19 µm.

5.5 Measurement of physical cross-sections

In order to validate the measurements of depth of penetration obtained *in situ* by direct fluorescence imaging of a printed sample under the CLSM, some physical cross-sections of printed samples were prepared by FFIC to be imaged (in the xy plane) and analysed under the CLSM.

The ultra-thin cross-sections were produced with a microtome blade after the sample was embedded in a resin. Paper and dye manufacturers currently used this method to observe the inside of the paper under an SEM microscope, for analysis of absorbency and ink penetration, critical in the paper- and dye-manufacturing process. The information obtained in this way is used for quality control and optimisation of the printing characteristics of both paper and dye. Nevertheless the process by itself is very tedious, time consuming and costly.

It can also alter the sample and often smears the interface layers, making such observations somewhat ambiguous.

The cross-sections received from FFIC were printed with an OAM magenta dye printed in three types of paper at two different concentrations, 100% and 10% colour intensity. They were observed under the CLSM exciting the dye at 543 nm and collecting the emission above 600 nm, as the emission spectra suggests (Appendix I), at the same time that a transmission image of the full cross-section was collected for comparison.

Figure 5-21 shows a transmission image merged with the fluorescence image (a) and a fluorescence image (b) obtained for the cross-section of an OAM ink printed in paper A with 100% colour intensity. The transmission image allows the identification of the different layers of the paper. The ink-receiving layer coincides with the fluorescence image while the boundary between the barriers, the cellulose and back-coat layers are clear.

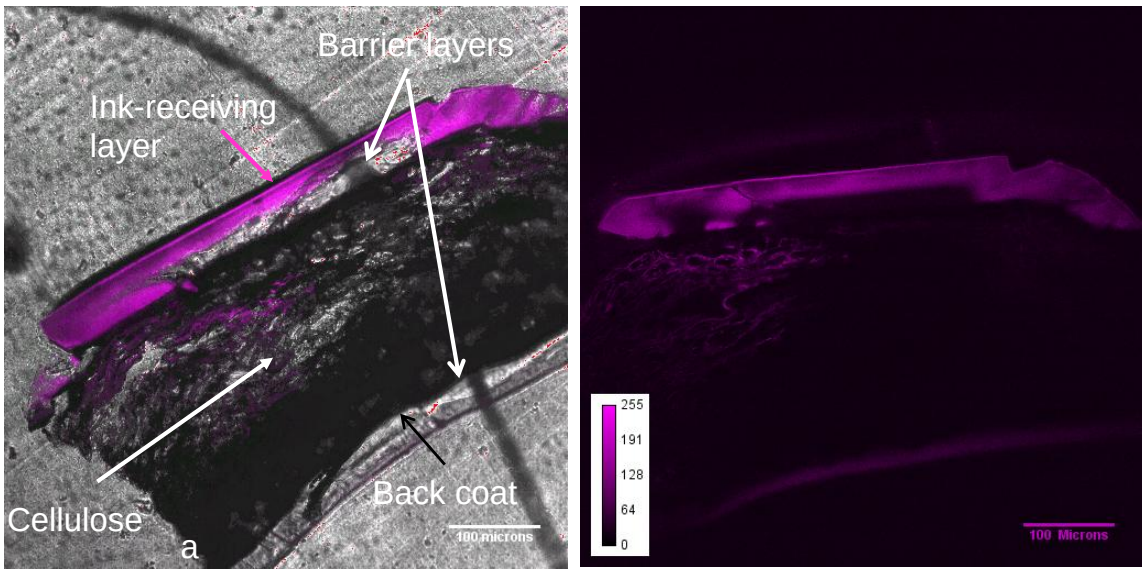

Figure 5-21 Cross-section of a sample of an OAM ink printed in paper B. Transmission image merged with fluorescence image (a) and fluorescence image (b).

Using Image J [18] analysing tools it is possible to measure the line profile at different points of fluorescence image of the cross-section as shown in Figure 5-22 and therefore the width of the ink layer section. The thickness measured for the ink layer varies from 24 to 21.5 µm with an average of 22.9 + / - 0.8 µm.

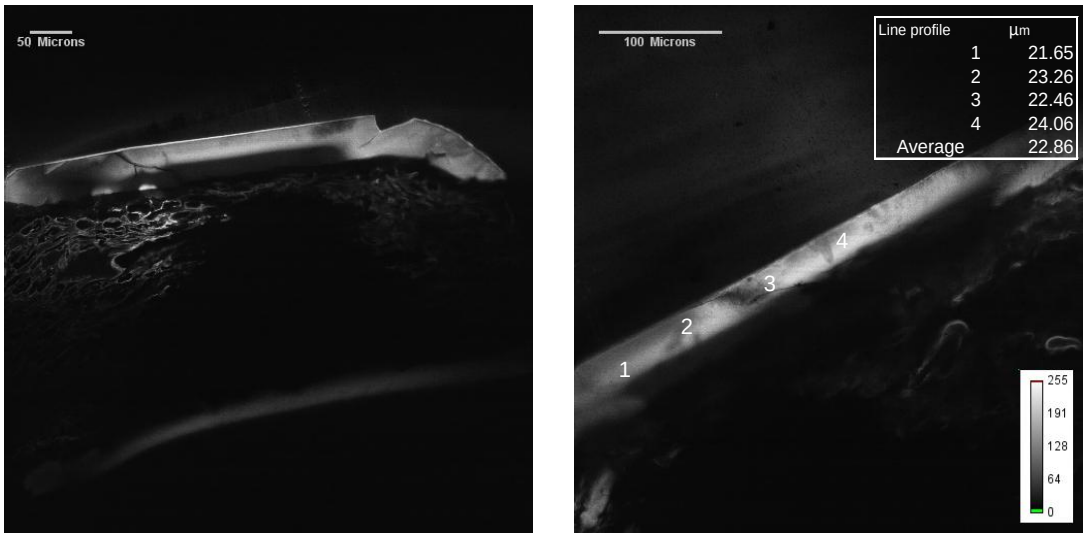

Figure 5-22 Fluorescence intensity image of a cross-section of an OAM ink print in paper A and line profiles of a magnified image.

In order to verify the applicability of the *in situ* method, the same print was observed under the CLSM. Figure 5-23 shows the fluorescence image of the 100% colour intensity sample and its depth profile. The FWHM measured is 14 µm + / -1 µm, which corresponds to 20.7 + / - 1.5 µm when corrected with respect to the refraction index, which in this case is 1.48 according to Bakker [33] for a magenta dye printed in an inkjet paper and absorbing at 543 nm. This is in very good agreement with the value of 22.9 +/- 0.8 µm measured directly from the cross-section.

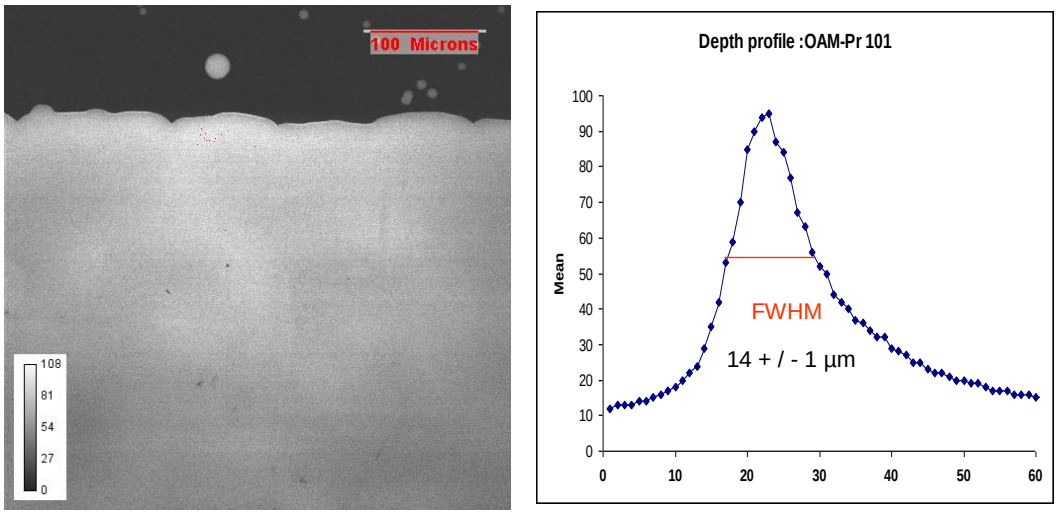

Figure 5-23 Fluorescence intensity image obtained from an OAM ink printed in paper A sample (a) and depth profile of the same sample with an FWHM of 14 + / - 1 µm.

When the cross-section of the 10% OAM printed sample was observed under the CLSM, images as illustrated in Figure 5-24 were obtained. The ink layer observed has a uniform width and the line profile values obtained were similar. The average line profiles value of the fluorescence cross-section image was 12 .9 + / - 1.2 µm.

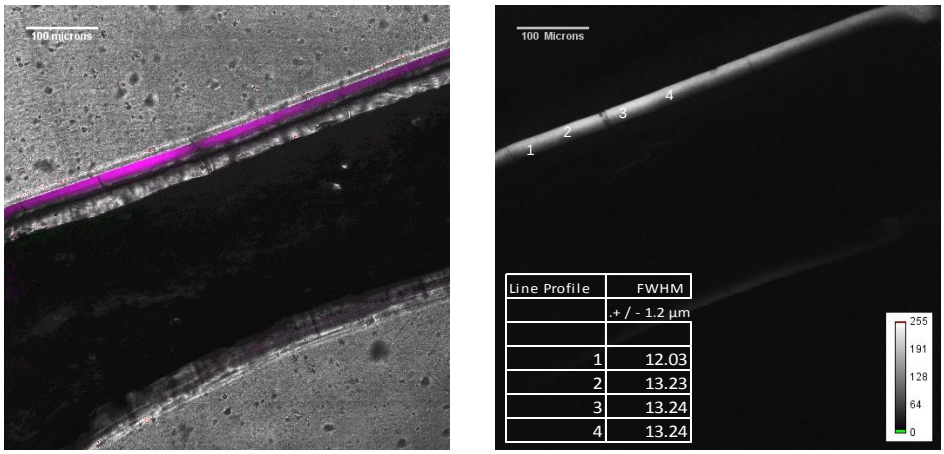

Figure 5-24 Cross-section of a sample of an OAM ink print (10%) in paper A. Transmission image merged with fluorescence image (a) and fluorescence image (b).

Figure 5-25 shows the image obtained for the 10% colour-intensity print in paper A when observed under the CLSM. The depth profile was calculated for each dot as well as a total dot average (11.8 + /- 1.5 µm). It is noticeable that the penetration of the dots is uniform.

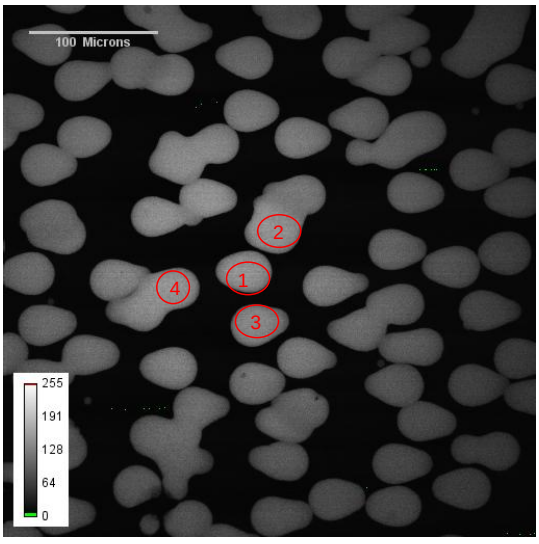

Dot	FWHM µm + / - 1	FWHM* µm + / - 1.5
1	6.0	8.9
2	6.0	8.9
3	7.0	10.4
4	6.0	8.9
Average all dots in the image	8.0	11.8

Figure 5-25 Fluorescence intensity image of an OAM ink print in paper A with 10% colour intensity, depth profiles of various dots and average of all dots in the image.

This uniform penetration can be confirmed by observing the 3-D images as illustrated in Figure 5-26.

Figure 5-26 3-D projection (Image J) of an OAM print in paper A.

The depth profile results obtained *in situ* (11.08 + / - 1.5 µm) are in good agreement with the depth profile obtained from the cross-section (12 .9 + / - 1.2 µm).

The cross-section of the paper B print sample has an average line profile of 17.2 + / - 0.8 µm as is shown in Figure 5-27. On the transmission image (a) illustrated in the same figure, the different layers of this inkjet coated paper are clearly visible, nevertheless it is the fluorescence intensity image which clearly shows the ink layer.

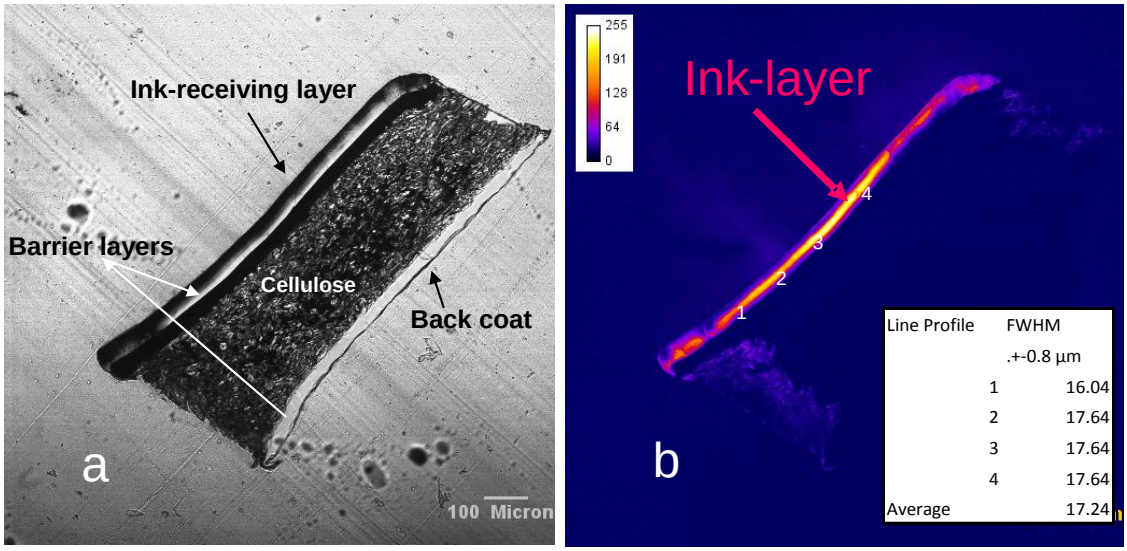

Figure 5-27 Transmission image of the cross-section of an OAM ink printed in paper B at 100 % colour intensity (a) and fluorescence image of the same sample with some line profiles (b).

The fluorescence images obtained for the 100% colour-intensity samples and the corresponding depth profiles are shown in Figure 5-28. The FWHM obtained for this sample was 12 +/- 1 µm or 17.8 + / - 1.5 µm when corrected.

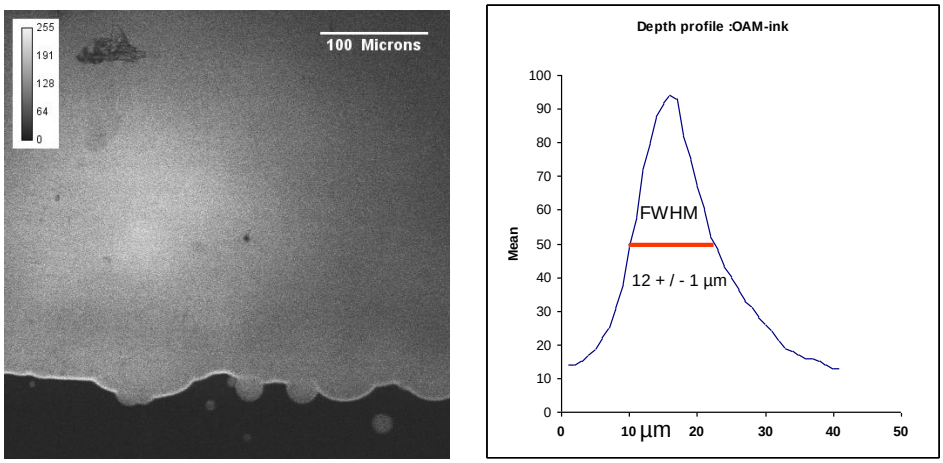

Figure 5-28 Fluorescence intensity image obtained from an OAM ink print in paper A (a) and depth profile with an FWHM of 12 + / - 1 µm.

The results obtained for the paper B samples further supported the validity of the *in situ* CLSM technique as the results obtained from the cross-section (17.24 + / - 0.8 µm) and *in situ* (17.8 + / - 1.5 µm) were in accordance.

The images obtained for the cross-section of the sample with 10% colour intensity were interesting as the individual dots seem to be recognisable in the fluorescence intensity image. Figure 5-29 shows the transmission image as well as the fluorescence image.

In both images the position of the dye is visible and the depth of penetration of the dots seems uniform with an average line profile of 11.07 + / - 1.2 µm.

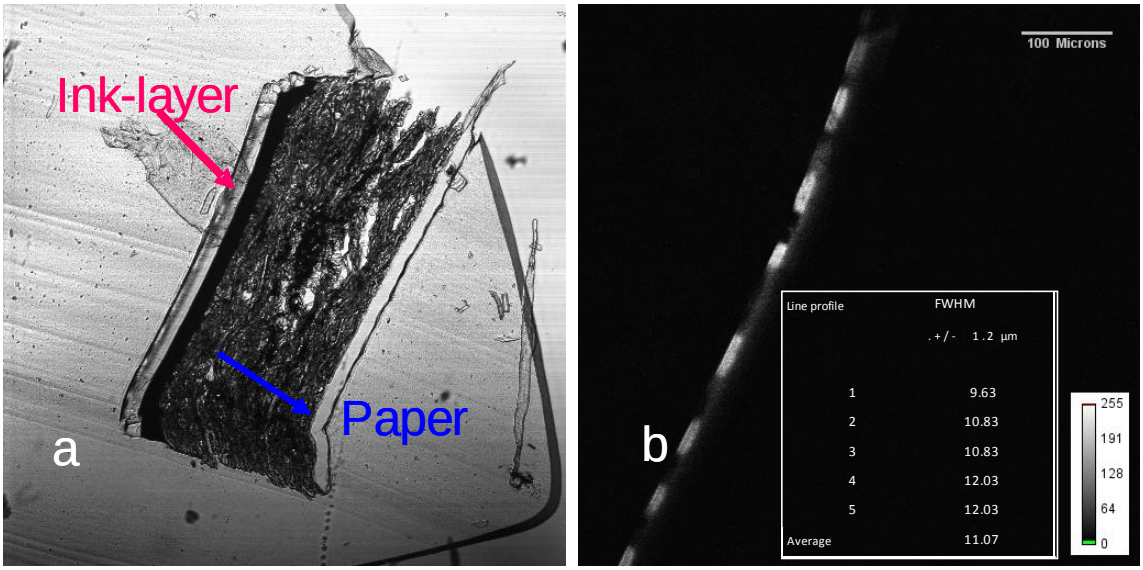

Figure 5-29 Cross-section of a sample of an OAM ink printed in paper A at low concentration. Transmission image (a) and fluorescence image (b).

The depth profile obtained *in situ* for this paper was 11.8 + / - 1.5 µm as shown in Figure 5-30, in good agreement with the value obtained from the cross-section.

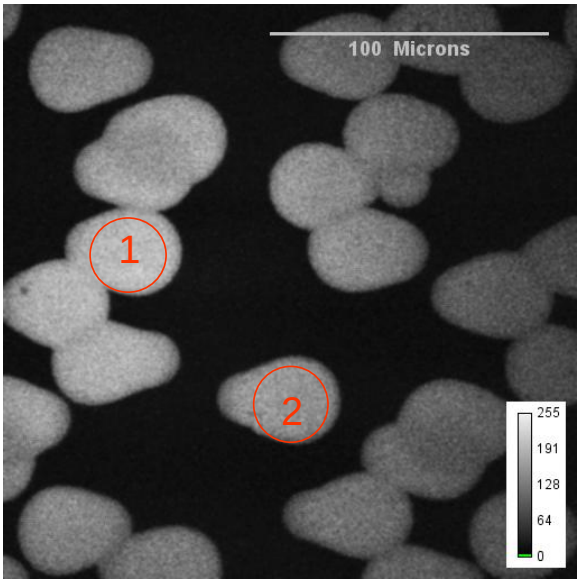

Dot	FWHM	FWHM*
	µm +/ - 1	µm +/- 1.5
1	7	10.4
2	6	8.9
Total Average	8	11.8

Figure 5-30 Fluorescence intensity image of an OAM ink print in paper A at 10% colour intensity and depth profiles of various dots and the average of all the dots in the image.

And finally we consider the results obtained for the cross-section of paper G, a non-coated inkjet paper with a non-uniform ink penetration as shown in Figure 5-31. The ink is not visible in the transmission image alone, therefore it is necessary to merge the transmission image with the fluorescence image to observe the position of the dye with in the sample.

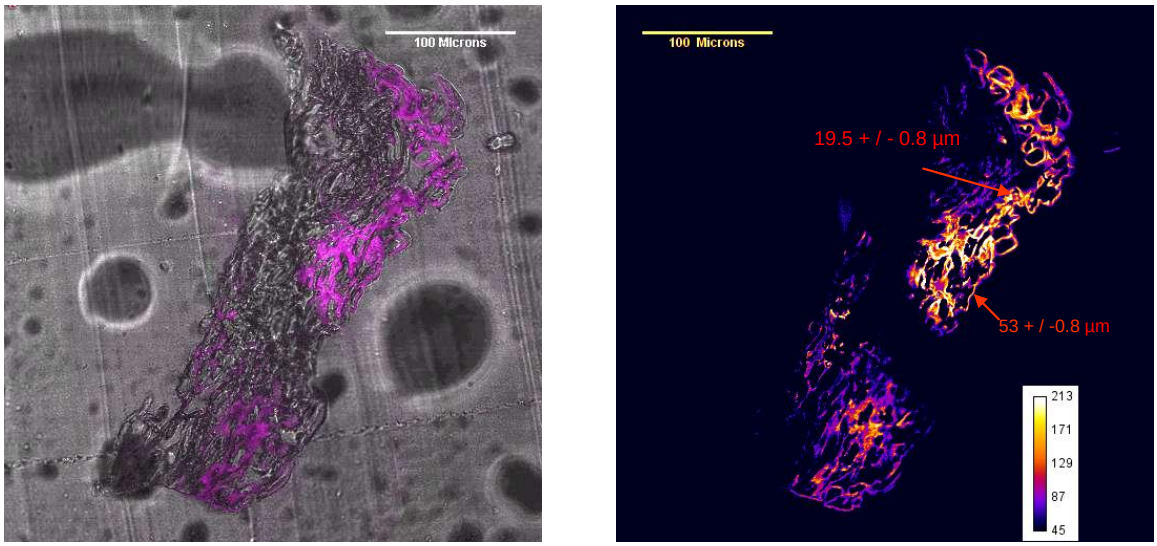

Figure 5-31 Cross-section of a sample of an OAM ink printed in paper G at full concentration. Transmission image (a) and fluorescence image (b).

The sample itself looks deformed maybe due to the difficulty in handling this type of paper. The depth of penetration could not be defined because of the non-uniform distribution of the dye some regions showed a penetration around 20 µm and in others the penetration was of the order of 50 µm.

The analysis of the printed sample suggests a different fixation mechanism from the previous papers as the dye seems to adhere to the cellulose fibres with a random approach as Figure 5-32 illustrates.

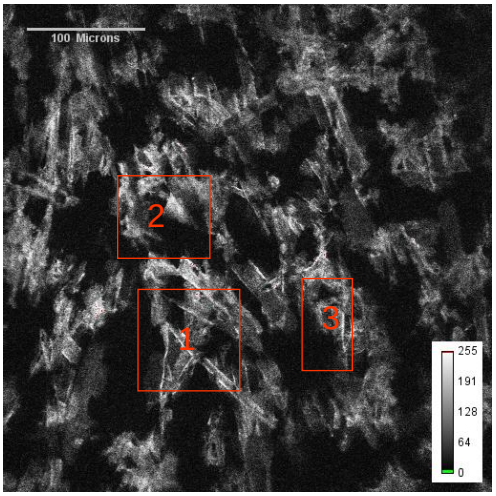

Dot	FWHM	Refraction index
	µm + /- 1	n= 1.48
1	14	20.7
2	16	23.7
3	18	26.6
Average all image	19	28.1

Figure 5-32 Fluorescence intensity image of an OAM ink printed in paper C with 100% colour intensity and depth profiles of various sections with overall image average.

5.6 Conclusions

The CLSM proved to be a very useful technique to observe and measure printed inkjet dots as high-contrast images were obtained due to the high fluorescence intensity of the analysed dyes and the absence of fluorescence from the paper at the wavelength studied. Print quality depends on the shape and size of single dots, therefore the possibility offered by the CLSM to show the shape and measure the area of single dots converts it in an important tool for print quality control.

The capillary technique employed to validate depth profiling proved that within the range of interest there is no substantial loss of fluorescence intensity and therefore the measurements of depth can be taken with good accuracy.

Being able to detect and localise the surface of the paper by using the reflectance mode at the same time as the fluorescence images in the CLSM is of great importance, as the position of the dye relative to the surface of the paper is an important print quality property.

The CLSM proved to be a powerful technique to measure depth of penetration of the inkjet dyes within the papers thanks to its ability to slice the sample in the z-axis. The FWHM values obtained from the depth profiles are a useful tool to compare the behaviour of a dye in different prints. Although depth profile can be approximate to the FWHM it is important to consider the difference in refractive index of the media in which the light travels. Therefore it is necessary to correct the value of the FWHM by considering the refractive index of the print. In this way a more real value of depth of penetration is obtained.

The fluorescent intensity images obtained from the physical cross-sections illustrate very clearly the thickness of the ink layer within the paper and by merging this fluorescence image with the transmission image, it is possible to observe the position of the dye within the structure of the paper. Being able to measure the thickness of the ink layer in the physical cross-section allowed the validation of the *in situ* depth profile.

In general it can be concluded that the CLSM is a very useful, non-destructive, non-invasive, easy and fast technique to evaluate the print quality of a printed sample as it can measure the position of the ink layer relative to the paper surface, and the vertical and radial distribution of the ink droplets on the paper.

6 Two-Photon Laser Scanning Microscopy (2PLSM)

6.1 Introduction

Two-photon excitation occurs when two photons are absorbed in a single coherent event. The energy of both photons is combined to excite a molecule from ground state to an excitated state, and since the energy is inversely proportional to the wavelength, each photon absorbed must have double the wavelength required for one photon excitation. This means that a fluorophore that absorbs UV light (350 nm) can be excited by two photons of near infrared light (700 nm).

Two-photon laser scanning microscopy (2PLSM) is intrinsically confocal; the absorption is limited to a very small volume at the focus of the objective lens at one time, eliminating the need for confocal apertures, and collecting all the fluorescence emitted by the sample while providing optical sections similar to those obtained in the CLSM. It uses longer wavelengths (IR) which suffer less scattering when penetrating deeper into the samples. Although it is difficult to calculate the level of scattering precisely, the simplest approximation of Rayleigh scattering establishes that the amount of light scattered is inversely proportional to the fourth power of the wavelength of the light. This difference in scattering allows investigation of deeper depth of penetrations than one-photon CLSM.

Another advantage of 2PLSM is the ability to excite UV-absorbing fluorophores, such as those found in inkjet paper. Therefore it offers the possibility of the analysis of the fluorescence emitted by the paper and how the dye can affect it.

6.2 Materials and Methods

6.2.1 Materials

Three different papers printed with the same dye were studied. The papers are commercially available coated and plain inkjet papers and the chosen dye for this analysis was the OAM dye (see Chapter 4).

The papers analysed were the subject of those studied in Chapter 4: microporous silica-based, a microporous alumina-based and a plain paper as listed in table 6-1.

Table 6-1

MEDIA NAME	TYPE	NUMBER OF LAYERS	COMPOSITION OF INK-RECEIVING LAYER
A	MICROPOROUS	5	40 µm Alumina + trace organics.
B	MICROPOROUS	4	37 µm Silica + polythene binder with traces of aluminium.
G	PLAIN	N/A	None available

Table 6-1 Inkjet papers, type, number of layers and composition of ink-receiving layer.

6.2.2 2PLSM

The Biorad 2000 CLSM assembled with an inverted Nikon T-300 microscope and coupled with a Ti: sapphire femtosecond pulsed laser was the equipment employed in this study as described in Chapter 3. The printed pattern was the same as the one used in Chapter 4.

2PLSM at 750 nm (excitation of paper and dye)

The method created visualises the fluorescent paper molecules and the dye at the same time in two different channels. The objective lens selected was a Nikon PA 20X dry with a numerical aperture (NA) of 0.75. The molecules were excited using a Ti: sapphire pulsed laser (Coherent Mira) at 750 nm, a repetition rate of 76 MHz, pulse length of 200 fs and power of 400 mW. In PMT 1 the emission from the fluorescent paper molecules is collected through a 500 nm dichroic mirror, between 410–490 nm (emission filter HQ450 / 80) using a blocking filter E625SP and in PMT 2 the emission from the dye molecules is collected with a long pass emission filter above 570 nm (E570LP), using a blocking filter E625SP. Under these conditions and working with a 1.5 zoom, the xy pixel size is 0.8 µm and one

xy-plane image corresponds to 411 μm x 411 μm, the step chosen was 1.0 μm. The speed of laser scanning was 500 lines per second per single image of 512 x 512 pixels. The data analysis was performed using digital image-analysis software in the public domain called Image J, which is a Java image-processing software developed by Wayne Rasband and others at the National Institute of Health, USA [18].

2PLSM at 920 nm (excitation of dye only)

The method created involved two sequences: the first one excited the sample with the Ti: sapphire laser tuned at 920 nm and collects the fluorescence through a long pass emission filter (E570LP) using the blocking filter HQ 575/150. The second sequence uses a He-Ne laser (543 nm) to excite the dye, in a one-photon process, and collects the fluorescence emitted through a long pass filter above 570 nm (E570LP). The objective lens used was a Nikon PA X 20 / NA 0.75 dry. For the confocal image a pinhole size of 1.0 was used giving a thickness of a single confocal plane or optical slice of 1.7 μm and the step between slides was 1.0 μm. Under these conditions and working with a 1.5 zoom, the xy pixel size is 0.8 μm and one xy-plane image corresponds to 411 μm x 411 μm. The speed of laser scanning was about 500 lps per single image of 512 x 512 pixels. All the images were scanned and averaged three times. The step used to record the optical slides was 1 μm in both sequences. The software used to measure depth profile was Image J [18].

6.3 Results and Discussion

6.3.1 Excitation – Emission Spectra

The excitation and emission spectra of the three papers are shown in Figure 6-1. Paper A and B can be excited in the region between 350–400 nm and the emission can be collected between 420 and 500 nm. Paper G is less fluorescent than A and B but it can still be excited at 400 nm and the emission can be collected between 450 and 500 nm.

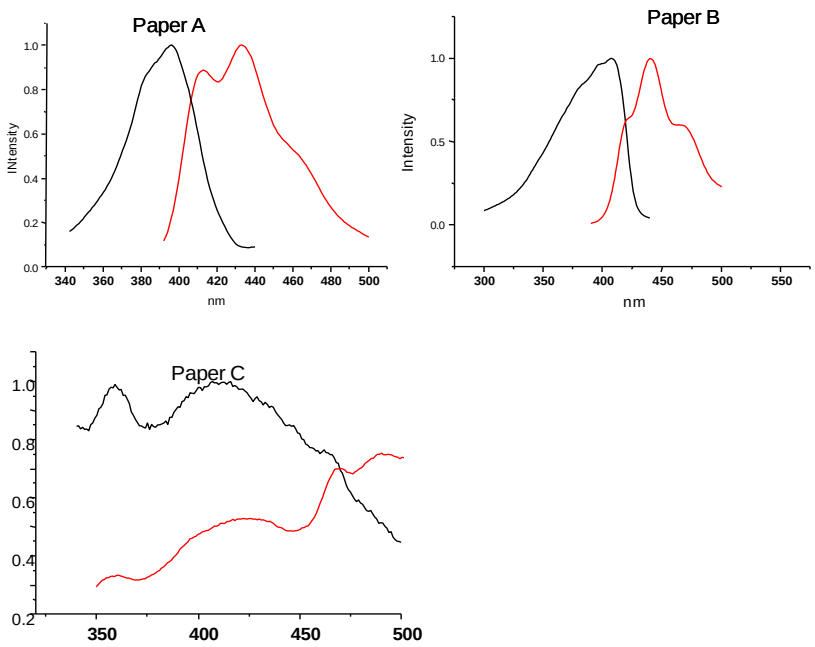

Figure 6-1 Excitation (black) and emission spectra (red) of unprinted paper A, B and G excited at 375 and emission collected between 390–500 nm

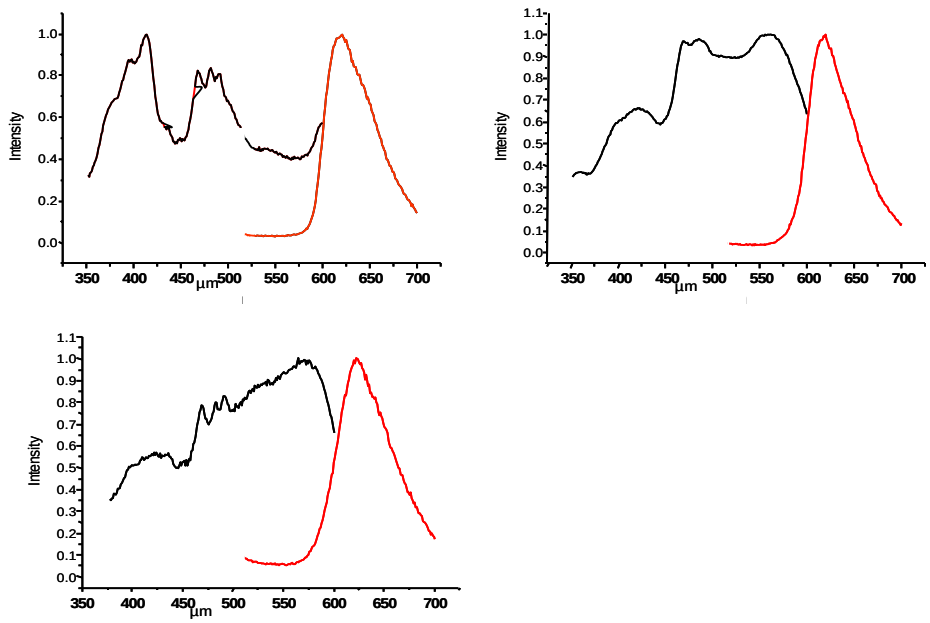

Figure 6-2 Excitation (black) and emission spectra (red) of printed paper A, B and C excited at 375 nm and emission detected above 600 nm.

As shown in Figure 6-2, when printed paper is excited at 375 nm, not only the fluorescent molecules from the paper are excited but the dye is excited as well. The emission can be collected, between 600 and 700 nm, offering the possibility of analysing the paper and the dye at the same time in the same location but in different wavelengths regions. The maximum emission of printed dye is shifted to a longer wavelength (620 nm) when printed.

The absorption spectra of the OAM dye shown in Appendix I shows no absorption at 375 nm so it is possible that the dye is excited by an energy transfer process or by re-absorption of the fluorescence emitted by the paper.

6.3.2 2PLSM exciting at 750 nm

6.3.2.1 Paper A

Two-photon excitation at 750 nm allows both the paper and the dye to be detected by collecting the fluorescence in two different wavelength regions at the same time, as Figure 6-3 shows. The fluorescence from the paper, between 410–490 nm, seems attenuated in the region where the ink is located due to an energy-transfer process or re-absorption of the fluorescence of the paper by the ink. The fluorescence of the dye observed, in the region between 570–650 nm, gives high-contrast images where sharp edges and paper defects are visible (Figure 6-3 and 6-4).

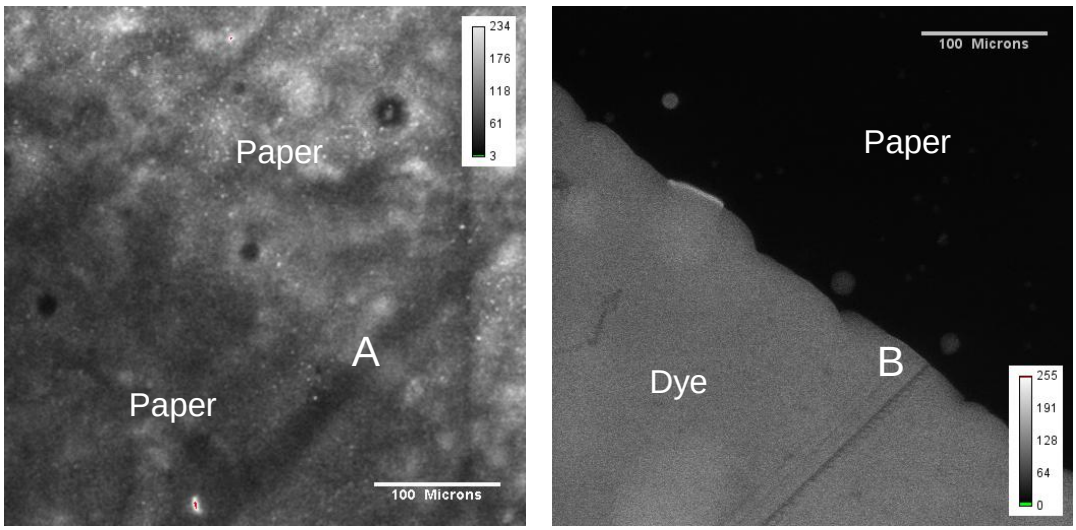

Figure 6-3 2PLSM images excited at 750 nm and emission collected at (a) 410–490nm (paper fluorescence) and (b) 570–650 nm (ink fluorescence).

The 3-D surface plot images shown in Figure 6-4 of the fluorescence emitted by paper and dye, show how the fluorescence of the paper is attenuated in the printed region (Figure 6-3a) while in the case of the dye fluorescence image (b), there is no fluorescence in the non-printed region.

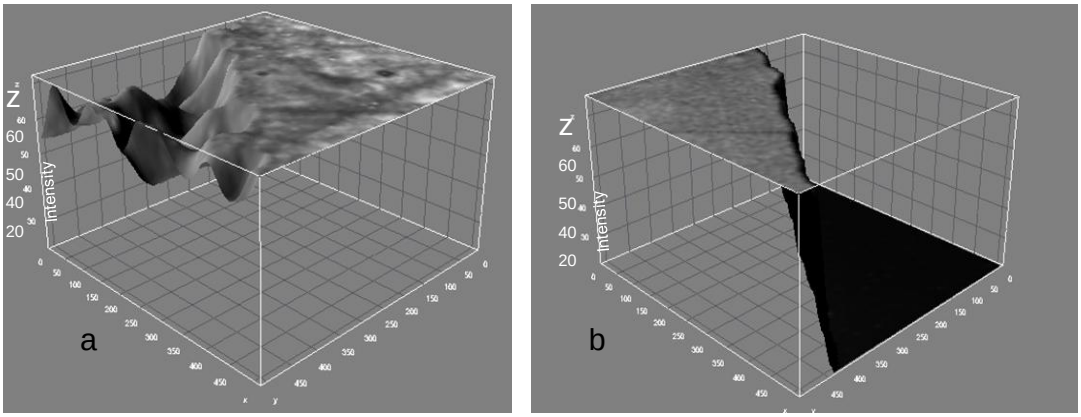

Figure 6-4 3-D Surface plot images for (a) the paper and (b) the dye.

The sectional views of the fluorescence images (Figure 6-5) show the fluorescence of the paper and the dye within the paper (xz plane) at the position indicated by the white line. It is interesting to note, that the fluorescence from the dye seems located nearer to the surface than the fluorescent molecules of the paper as it is indicated in the xz plane.

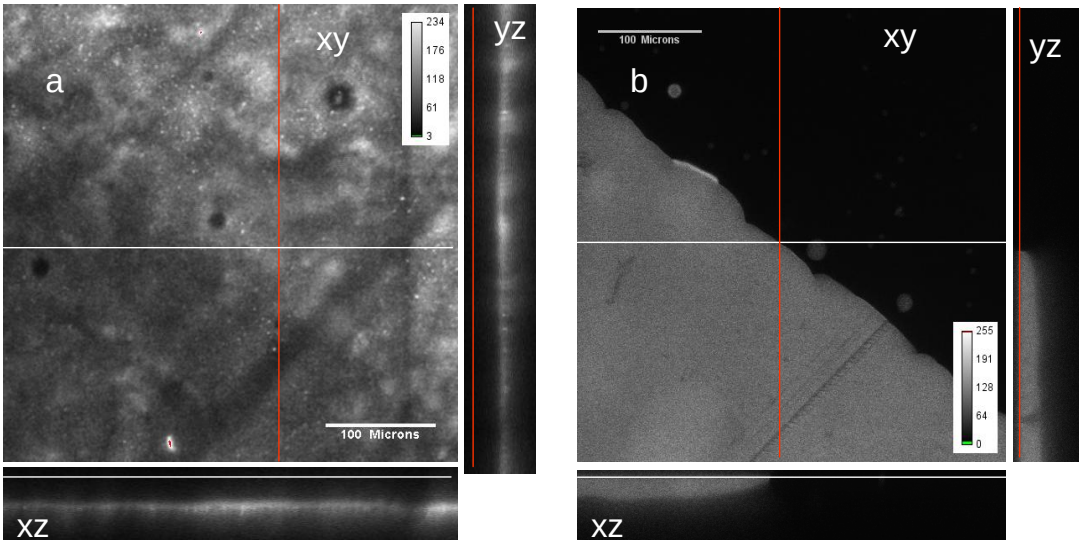

Figure 6-5 Orthogonal cross-sections of the paper (a) and ink (b).

The fluorescence intensity depth profile for the paper illustrated in Figure 6-6, shows that the maximum fluorescence peak is situated near the boundary of the second layer at 40 μm depth. (Appendix II). This indicates that the fluorophores being detected are concentrated in this region.

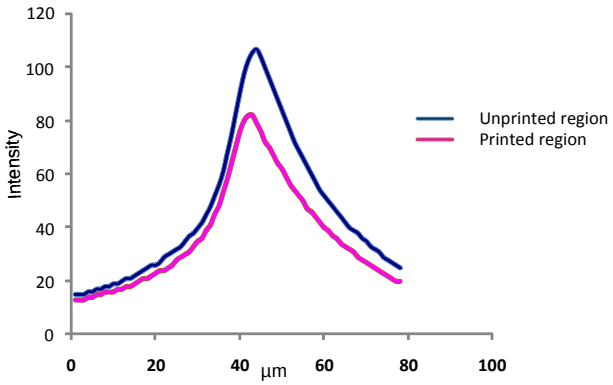

Figure 6-6 Depth profile of fluorescence emitted in the region between 410–490nm for paper (blue) and printed paper (pink).

The intensity profile of the printed and unprinted region is similar but the attenuation of the paper fluorescence intensity by the ink is evident.

Figure 6-7 shows the depth profiles of the paper and the dye. It can be seen that the dye is positioned near the surface while the fluorescence from the paper comes from a greater depth. The form of the curve of the depth profile obtained for the dye is different to the ones obtained in CLSM. 2PLSM gives a flat-topped fluorescence profile, whereas the one-photon excitation CLSM profile shows a sharp peak. This reflects the better ability of the two-photon excitation to penetrate into the paper and suggests that this may be a more accurate representation of the ink distribution. It can be inferred that the shape of the one-photon excitation profile is distorted by attenuation of the excitation intensity with depth, rather than an effect on the emission intensity. A more detailed comparison between one-photon and two-photon depth profiles will be presented in Section 6.3.3.

When the depth of penetration of the ink is taken as the length of the flat surface (16 μm) corrected for the corresponding refractive index (1.62) at 750 nm, the value obtained is 26.08 μm and the FWHM (21 μm) of the paper depth-profile curve corrected for refractive index (1.4) at 488 nm is 29.4 μm.

The exact position of the surface was not identified because a reflection image was not created.

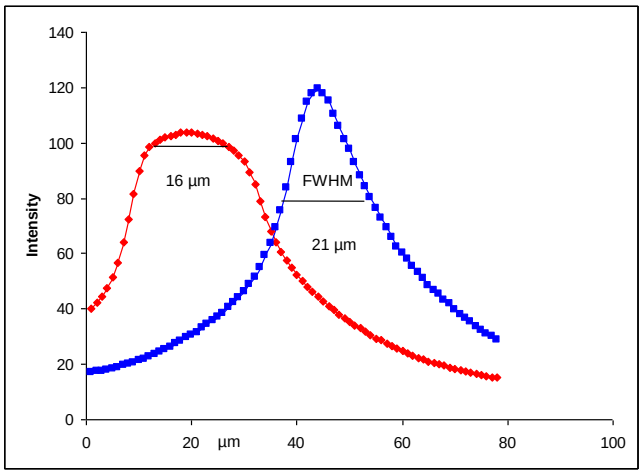

Figure 6-7 Depth profiles for the paper fluorescence (blue) and ink fluorescence (red). The FWHM for the paper is 21 µm and the length of the flat-topped curve of dye is 16 µm.

6.3.2.2 Paper B

The images obtained when analysing paper B, under the same conditions used for paper A, are shown in

Figure 6-8. As in the case of paper A, the fluorescence of the paper is attenuated by the presence of the dye in the printed region of the sample, and at greater depth the effect of the dye vanishes and almost all fluorescence of the paper can be observed once more at 49 µm. The image obtained for the fluorescence of the dye has a high contrast and is very clear. The edges of the printed patch, where the printer starts each row, shows a high intensity due to an excess of dye or ink in this place.

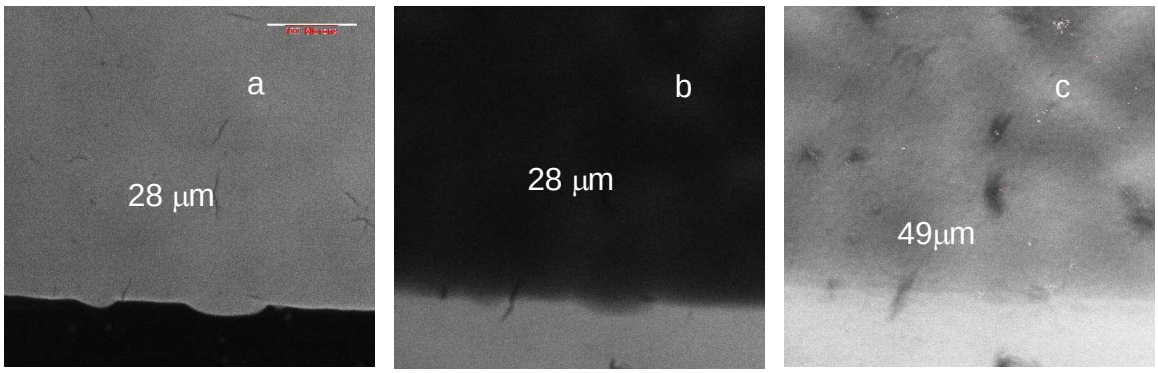

Figure 6-8 2PLSM images of paper B: (a) the dye fluorescence at a depth of 28 µm; (b) & (c) the paper fluorescence at a depth of 28 µm and 49 µm respectively.

The depth profile in Figure 6-9 shows the maximum fluorescence peak of the paper at approximately 40 µm from the onset of the fluorescence of the dye, coinciding with the boundary of the second layer of the coating of the paper. As for paper A the depth profile of the dye suggests a uniform distribution of the dye.

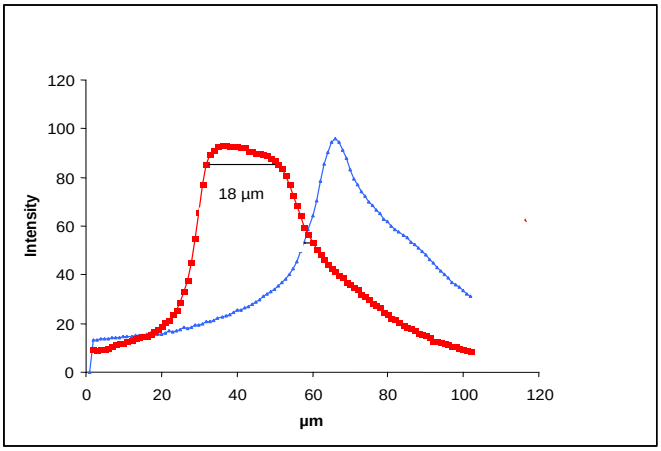

Figure 6-9 Depth profiles for the paper fluorescence (blue) and ink fluorescence (red). The length of the flat-topped curve of the dye is 18 µm.

The length of the flat-topped surface of the depth profile observed for the dye is 18 µm, and when corrected for the refractive index (1.62) at 750 nm, is 29.6 µm.

Figure 6-10Figure 6-10 shows the images obtained when a 10% intensity colour print was analysed. The behaviour is similar to the 100% intensity colour print assessed previously; the ink attenuates the fluorescence of the paper so that the dots can be clearly seen on the fluorescence image of the paper.

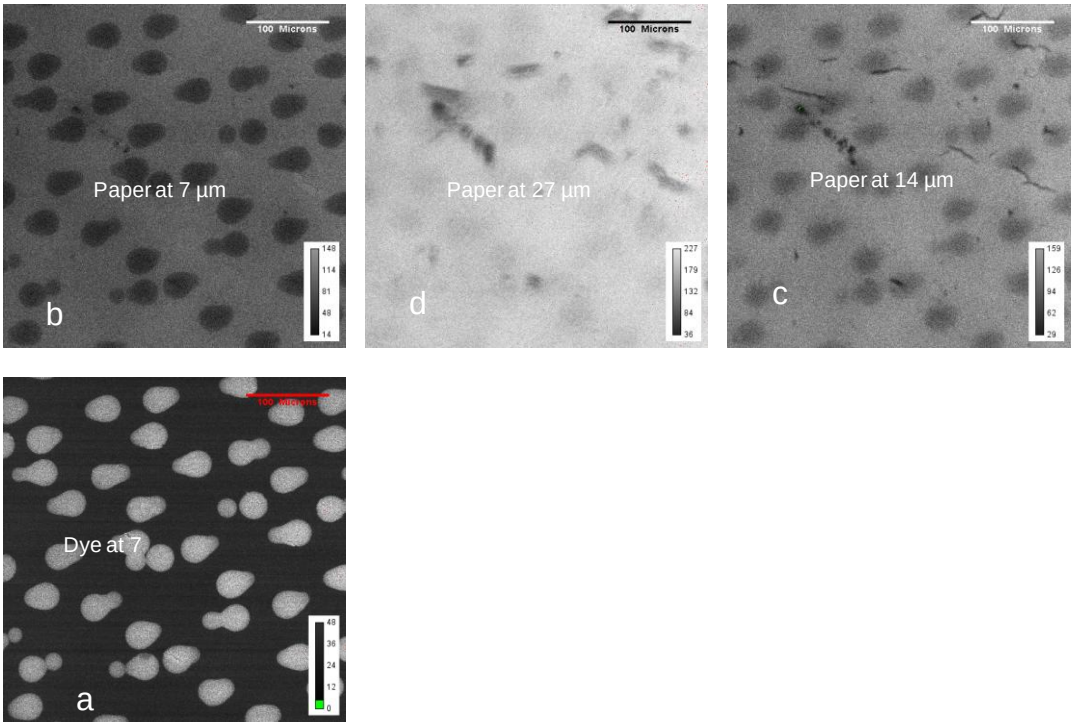

Figure 6-10 2PLSM images of 10% print (a) dye fluorescence; (b), (c) & (d) paper fluorescence at 7, 14 and 27 µm respectively.

The 3-D projection images for the 10% colour-intensity print, shown in Figure 6-11 confirm that the dye is positioned at a higher level (nearer the surface) than the fluorescent molecules from the paper. The 3-D projection obtained for the paper shows "holes" at the dot sites, marked in red, due to the attenuation effect.

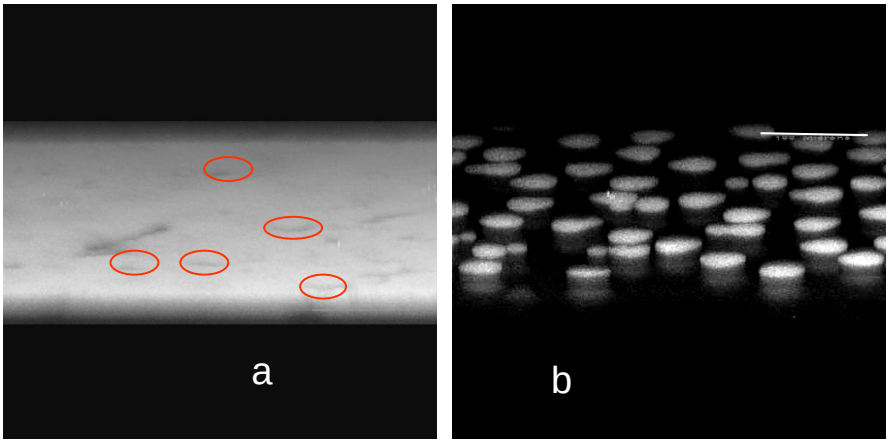

Figure 6-11 3-D fluorescent images for (a) paper and ink (b).

6.3.2.3 Paper G

Paper G does not have an ink-receiving layer as such; it is a type of paper in which the cellulose fibres have the function of fixating the dye.

Although the fluorescence of the paper is low, between 410–490 nm, it was possible to observe the unprinted fibres. Figure 6-12 shows the images and cross-sections of the paper and dye fluorescence. The fluorescence of the paper is present in the whole region analysed as shown in XZ and YZ sections and the distribution of the fluorescence signal from the dye is not homogeneous as it is localised in the fibres. This non- uniform penetration will affect the print quality as the dye will reflect light from different angles and depths.

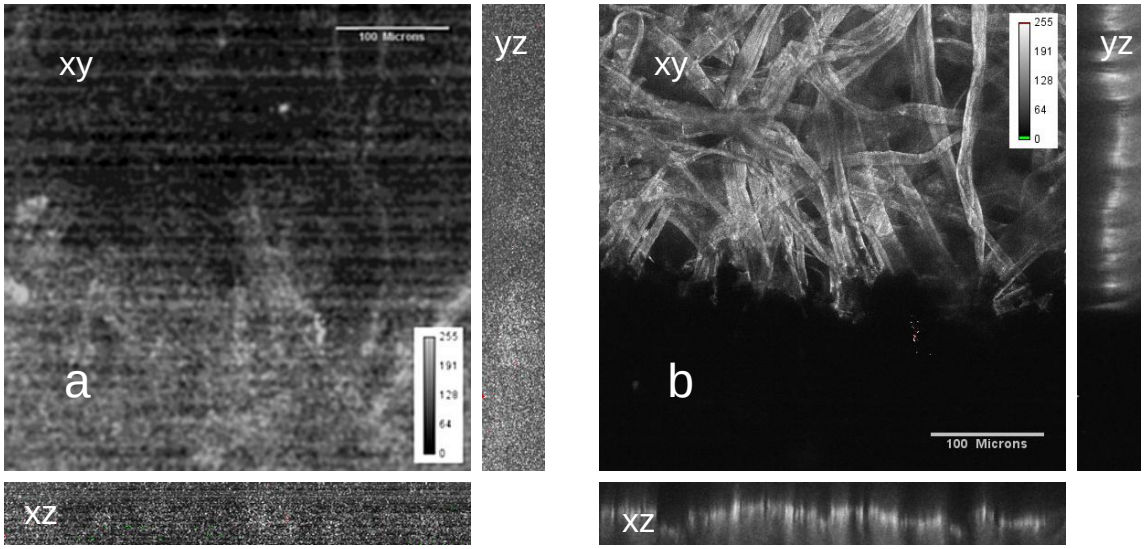

Figure 6-12 2PLSM images and cross-section of the paper (a) and the ink (b).

Microporous paper (silica and alumina-based), behave in a similar way in terms of fluorescence lifetimes of the paper and interaction with the dye.

6.3.2.4 Observation of non-fluorescent ink

Because the dye attenuates the fluorescence of the paper, some non-fluorescent dyes can be observed indirectly by exciting the paper. Figure 6-13 shows the fluorescence image collected from an inkjet paper printed with a blue (non-fluorescent) dye and its 3-D projection image illustrating the holes where the dye is placed.

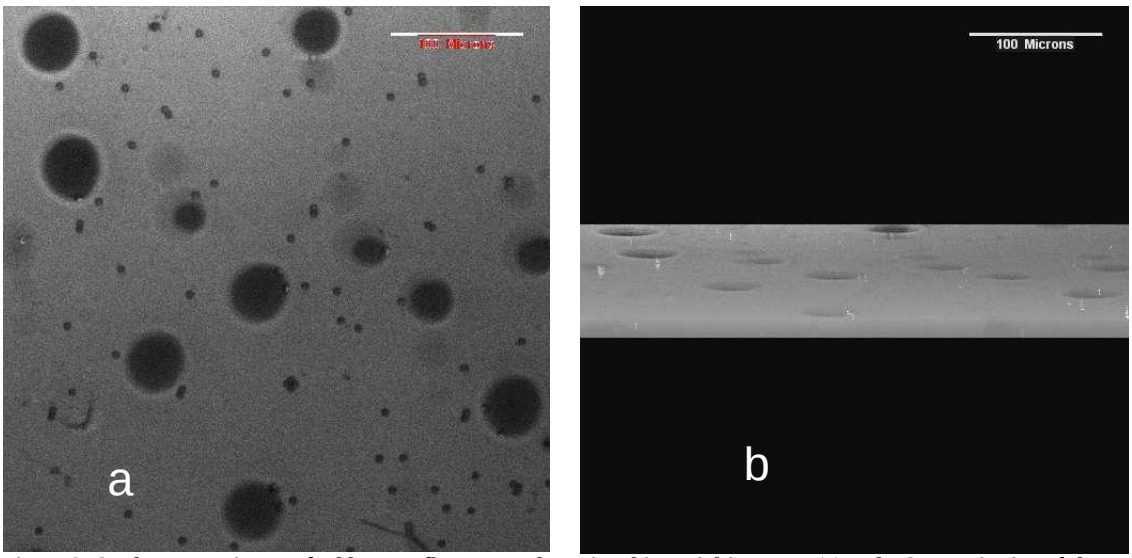

Figure 6-13 Fluorescent image of a blue non-fluorescent dye printed in an inkjet paper (a) and a 3-D projection of the same print (b).

Although non-fluorescent dyes were not studied in this work it is possible to use the CLSM to look at their behaviour through the fluorescence of the paper.

6.3.3 2PLSM – exciting at 920 nm

2PLSM excitation at 920 nm selectively excites the ink. Although the depth of penetration of the dye within inkjet papers is not greater than 40 μm, and therefore is ideal to be analysed and measured by CLSM, a comparison was made between two- and one-photon images, since in the two-photon technique no out-of-focus fluorescence is excited and there is less scattering of the excitation light, the image created may be of better quality. All measurements were done on the OAM ink, on each of the three paper types. The method used has been described in Section 6.2.2.

Validation of fluorescence depth profiling was performed doing the same test measurements as in Chapter 4, in the rectangular cross-section borosilicate capillary with a depth of 40 μm + / - 10% filled with an aqueous OAM solution. The depth profile was done under a CLSM and a 2PLSM, and the images obtained are shown in Figure 6-14. The image obtained with the 2PLSM shows very sharp edges of the capillary and the defects of the solution; the image has a higher contrast than that obtained with the CLSM.

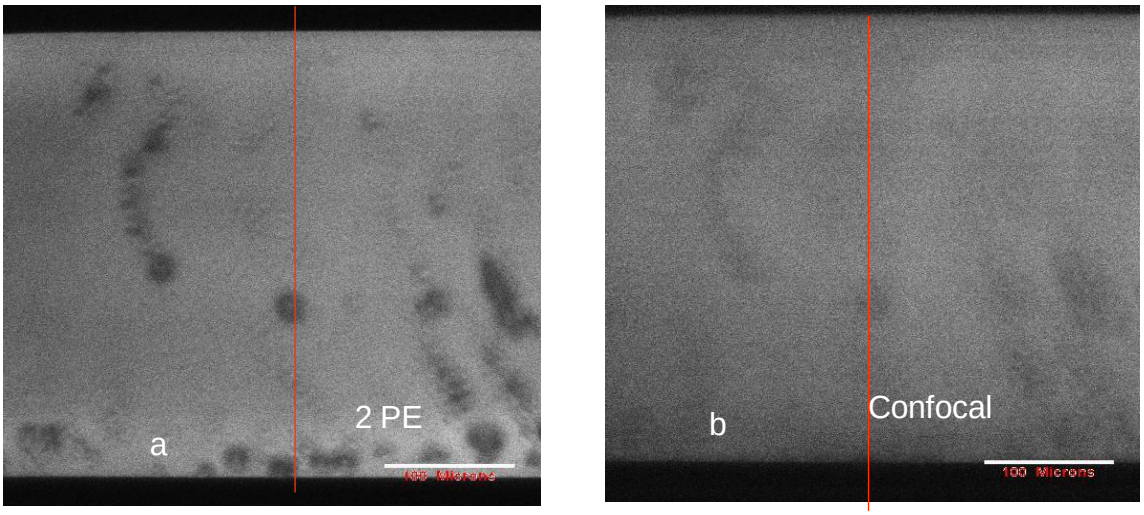

Figure 6-14 Fluorescence images of an OAM solution in the rectangular capillary obtained under (a) 2PLSM and (b) CLSM.

When the width of the capillary is measured along the red line shown in Figure 6-14, results as shown in Figure 6-15 are obtained where the sharpness of the capillary edges obtained with 2PLSM is evident as the line profile graph shows steep rising and falling edges.

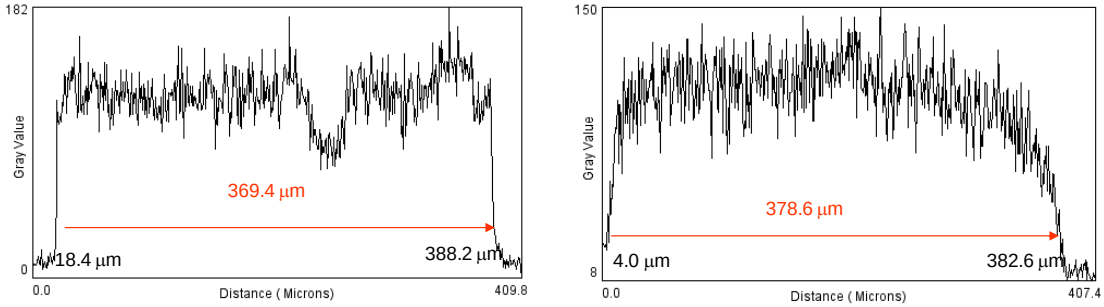

Figure 6-15 Line profile in the xy section of fluorescence images of an OAM solution in a rectangular capillary obtained with (a) 2PLSM and (b) CLSM.

The width of the rectangular capillary is 400 µm + /- 10% (Chapter 5) therefore the experimental values are within the limit permitted.

The depth profiles obtained for the rectangular capillary filled with OAM solution are shown in Figure 6-16. The curve obtained for the 2PLSM (a) is flat topped contrary to the CLSM (b) depth-profile curve. When the depth of penetration is taken as the length of the flat surface (21µm), and is corrected for the corresponding refractive index (1.6) at 920 nm, is 33.6 µm, compared with the FWHM (27 µm) of the CLSM depth-profile curve corrected for refractive index (1.4) at 488 nm which is 37.8 µm.

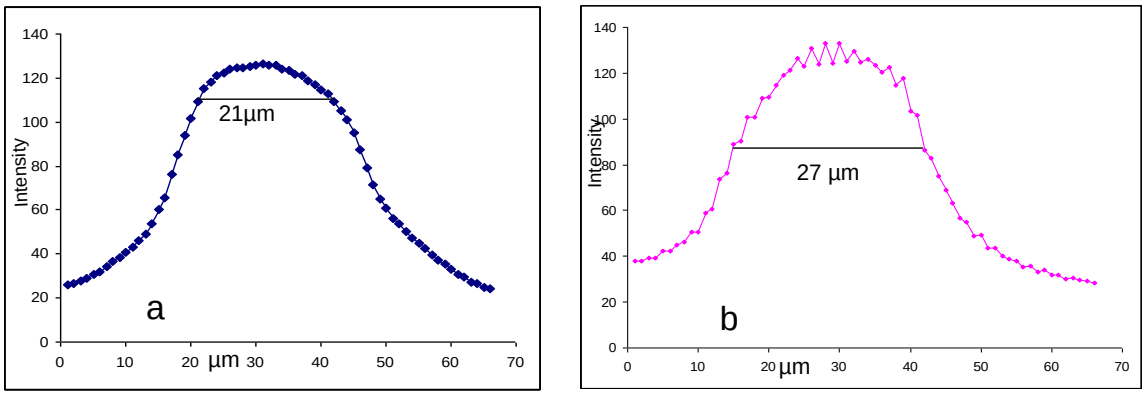

Figure 6-16 Depth profile of fluorescence images of an OAM solution in a rectangular capillary obtained with (a) 2PLSM and (b) CLSM.

6.3.3.1 Paper A

The image obtained with 2PLSM, proved to be of better quality than the image obtained with CLSM, as shown in Figure 6-17. The borders are sharp and the effects of the defects of the paper on the ink distribution are visible.

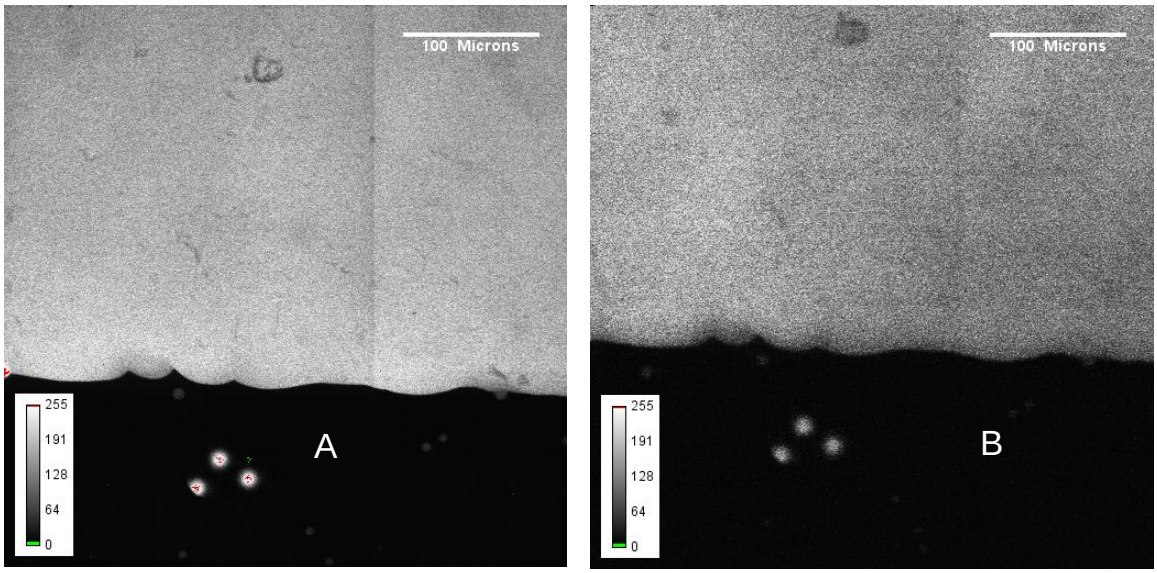

Figure 6-17 Fluorescence image obtained with 2PLSM (a) and with CLSM (b) for paper A.

To measure the depth profile using this method and compare it with the depth profile obtained with the CLSM, it has to be taken into account that the focal point of the Ti:sapphire laser is not at the same position as the focal point of the He-Ne laser in the CLSM. Figure 6-18 shows the depth profile of paper A printed, obtained with one photon excitation (CLSM) (b) and two photon excitation (2PLSM) (a). The curve shown for the CLSM has a peak and then the intensity decreases because of the scattering effect as the laser radiation penetrates into the sample. For two-photon excitation a flat-topped intensity profile is obtained (as observed when exciting at 750 nm), showing that the long wavelength radiation can penetrate deeper into the paper without loss of intensity. This indicates a homogeneous penetration of the dye.

When the depth of penetration obtained by the 2PLSM is taken as the length of the flat surface (16 μm) corrected for the corresponding refractive index (1.6) at 920 nm, is 25.6 μm, which is comparable with the FWHM (19 μm) of the CLSM depth-profile curve corrected for refractive index (1.4) at 488 nm which is 26.6 μm.

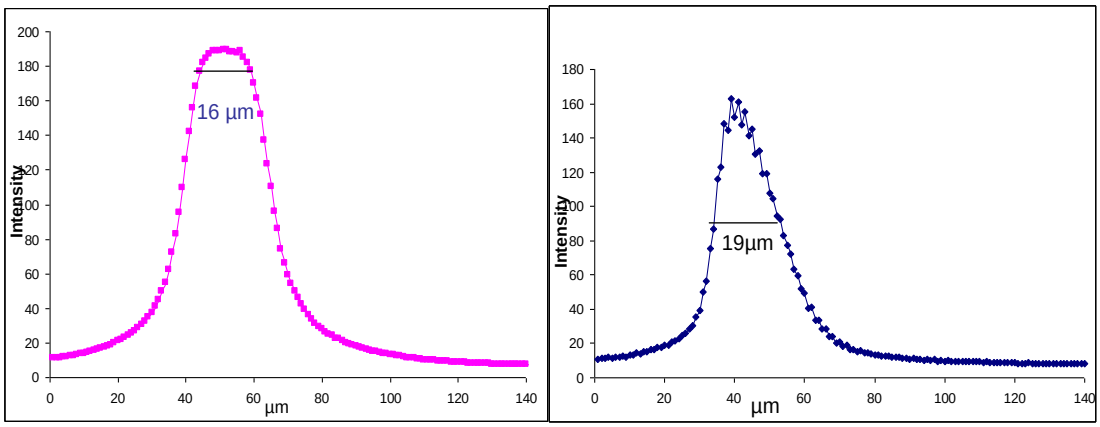

Figure 6-18 Depth profile of a paper A print, obtained with one-photon (blue) and two-photon (magenta) excitation methods.

In order to validate these measurements taken *in situ*, a physical cross-section of the same printed sample was observed (in the xy plane) using the 2PLSM and CLSM under the same conditions as used *in situ*.

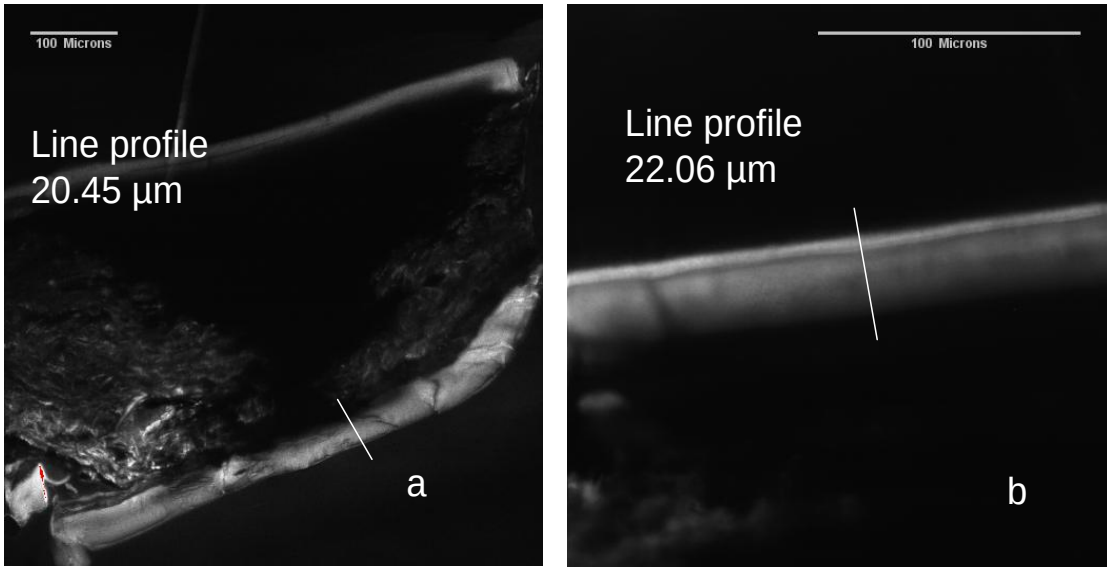

Figure 6-19 Fluorescence intensity image of an OAM ink printed in paper A cross-section and line profile obtained with 2PLSM (a) and a magnified image with the correspondent line profile obtained with CLSM (b).

Figure 6-19 shows the cross section of an OAM print, observed under the 2PLSM (a) and the CLSM (b). The ink layer thickness measured in the 2PLSM image was 20.45 µm and 22.06 µm in the CLSM image. The values obtained for the cross-section are in good agreement with the *in situ* results considering that the cross-section shows variations in the thickness of the ink layer across its total length.

Figure 6-20 shows the images obtained when a sample of paper A with 10% of colour intensity was analysed. The definition obtained in the two-photon image was much better than that obtained for CLSM.

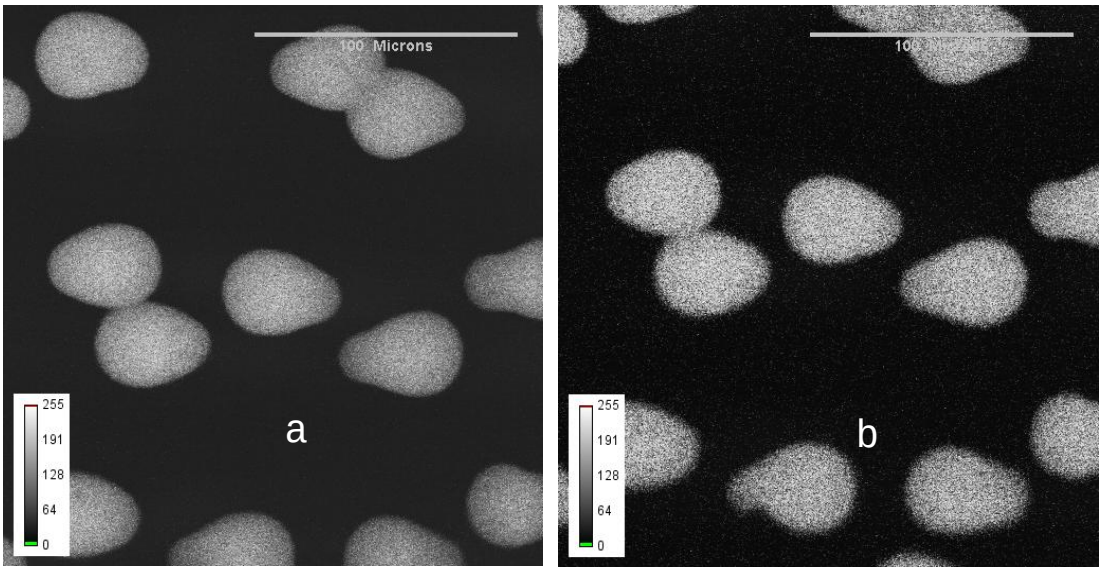

Figure 6-20 Fluorescence image obtained with 2PLSM (a) and with CLSM (b) for paper A.

6.3.3.2 Paper B

The results obtained when inkjet paper B was observed under the 2PLSM and CLSM, were similar to those obtained with paper A as both of them are inkjet coated papers and therefore have a special ink-receiving layer.

Figure 6-21 shows the cross-sections [32] of the images obtained with two- and one-photon excitation. It is interesting to note how the defects of the inkjet paper are observed along the z-axis in the two-photon excitation images denoting the better definition of the image.

The depth profiles obtained with 2PLSM and CLSM are illustrated in Figure 6-22. The depth profile for the two-photon excitation for paper A is much more symmetrical.

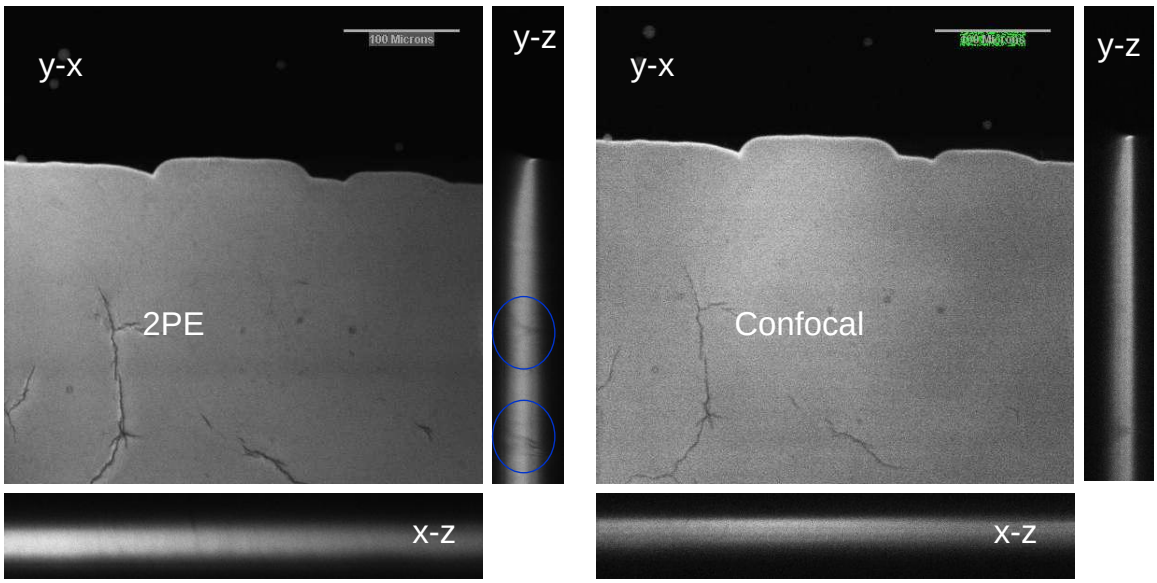

Figure 6-21 Orthogonal views of the fluorescence images obtained with 2PLSM (a) and CLSM (b) for paper A printed at 100% colour intensity.

If the length of the flat-topped curve obtained with one photon (16 µm) is corrected for the refractive index (1.6) the value obtained is 25.6 µm and the FWHM corrected for the refractive index (1.4) is 28 µm, values that are in good agreement.

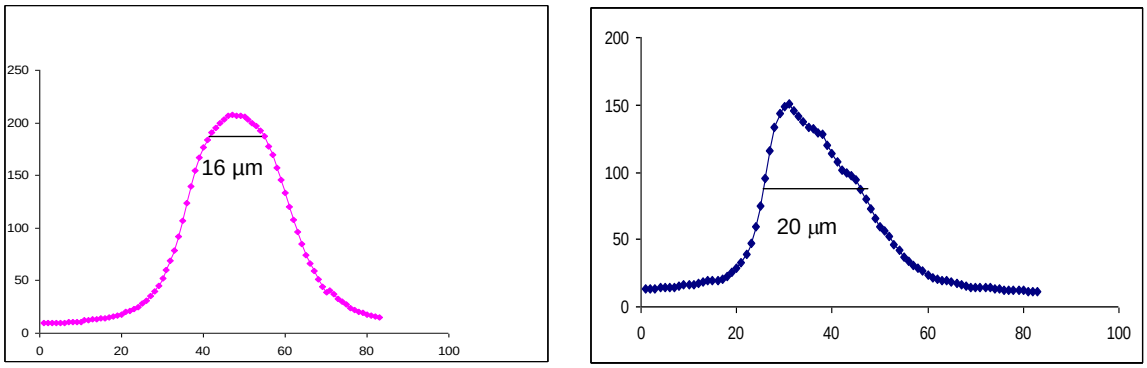

Figure 6-22 Depth profile of a printed sample of paper B obtained with two photon (magenta) with a length of the flat-topped curve of 16 µm and one photon (blue) with a FWHM of 20 µm excitation methods.

6.3.3.3 Paper G

Two-photon excitation proved to be very effective to observe the fibres of paper G. Figure 6-23 shows the fluorescence images obtained with two-photon and one photon fluorescence technique.

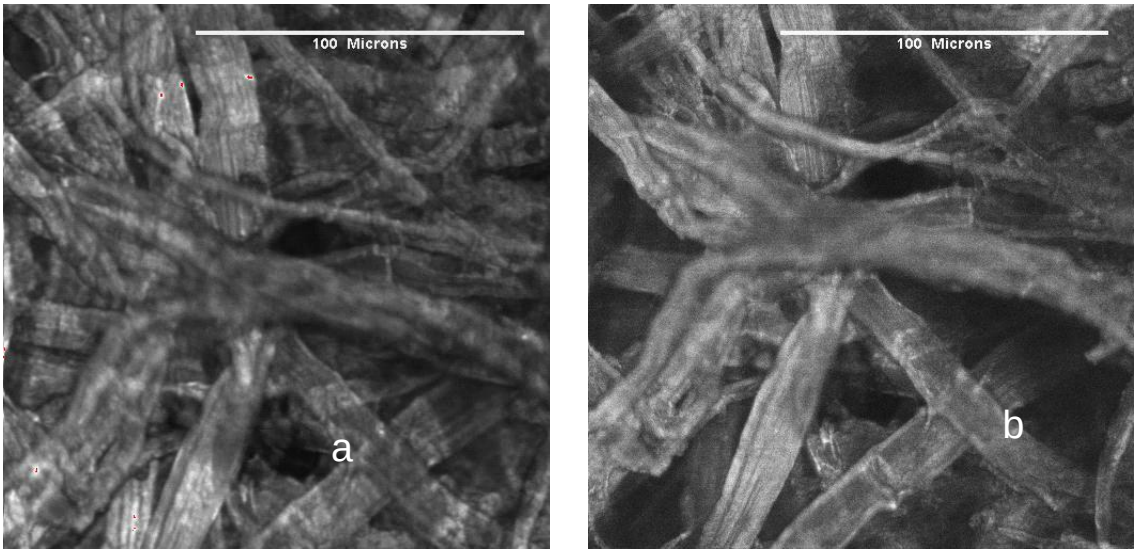

Figure 6-23 Fluorescence image obtained with 2PLSM (a) and with CLSM (b) for paper G.

The image created by two-photon excitation shows the paper with more detail, as more fibres can be observed. Not all the fibres have the same fluorescence intensity and some of them are not detected by the CLSM. It is important to verify that the fibres themselves are not intrinsically fluorescent in this wavelength region, and that the images are only the result of the absorption of the dye by the fibres. Figure 6-24, obtained when a 10% colour intensity print is analysed under the same conditions, confirms that this is the case as the fibres are visible only in the printed regions.

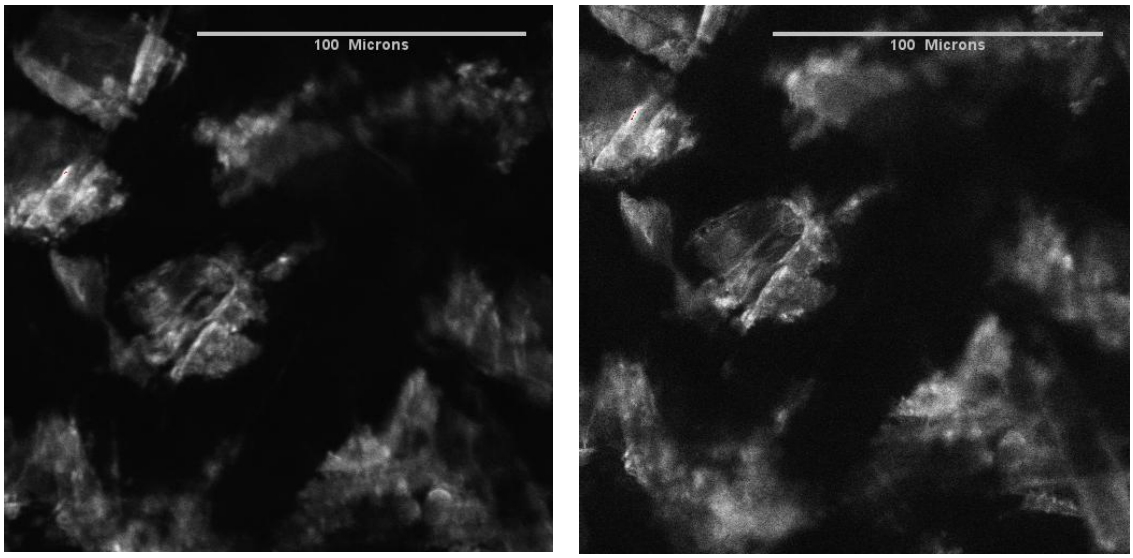

Figure 6-24 Fluorescence image obtained with 2PLSM (a) and with CLSM (b) for paper A at 10% colour intensity.

All these results prove that, the CLSM or one-photon excitation technique is enough to measure the depth of penetration of the printed inkjet papers, but to have a good detailed image of the print 2PLSM should be used.

6.4 Conclusions

It has been demonstrated that 2PLSM improves the quality of the images obtained allowing the observation of the defects of the paper and the effects of them in the fluorescence emitted. The edges of the features are very sharp, as shown for the rectangular capillary, the printed sample and the dots.

The ability of two-photon excitation to produce better-quality optical sections at greater depths was demonstrated by the shape of the depth profiles obtained for the inkjet papers analysed. The depth profile obtained with 2PLSM is much more symmetrical than that obtained with CLSM. The flat-topped curve obtained is due to less scattering suffered by the excitation light when penetrating, the absorption occurs only in the focal plane with no absorption in the optical pass, and the signal is kept constant throughout the depth of the sample. The absence of out-of-focus absorption and the lack of emission pinhole make it possible for all the emitted fluorescence to be collected by the detector, creating better defined and sharper images. The length of this flat-topped profile has been shown to indicate depth of penetration of the ink.

Another advantage of the 2PLSM is the possibility of exciting UV fluorophores as the ones present in inkjet papers. The attenuation of the paper fluorescence, in the printed region, suggests energy transfer is occurring or re-absorption of the emitted fluorescence of the paper by the dye. As a consequence of this effect, the depth profile obtained by excitation of the paper does not help in the identification of the position of the surface of the paper relative to the dye, as the maximum intensity of the paper fluorescence is below the position of the dye. Therefore the reflectance mode described in Chapter 5 continues to be the best method to locate the surface of the paper. This attenuation effect of the dye can be used to advantage, however, in the observation of non-fluorescent dyes and their location within the paper.Non-fluorescent dyes can be detected indirectly as a result of the attenuation of the fluorescence emitted by the paper, CLSM can be used to measure depth of penetration, although it does not accurately report the shape of the dye profile. In general, two-photon excitation (2PLSM) provided better quality images compared to CLSM.

7 Two-photon Fluorescence Lifetime Imaging Microscopy of Inkjet Dyes and Inkjet Papers (2P-FLIM)

7.1 Introduction

In inkjet printing the absorption mechanism that governs the distribution of ink on the paper, depends on the chemical and physical properties of the ink, paper and print head. It has been proved that the distribution of the ink inside the paper is an indication of print quality, print durability, image stability, optical density, and light and water fastness [26]. Driven by the need to understand this mechanism, several groups have been trying to comprehend the relation between paper and ink on print quality by using different approaches.

7.1.1 Ink–paper interactions

As explained, in Chapter 2, inkjet technology has been growing and developing very fast during recent years, forcing the ink and paper manufacturers to develop new products that meet the required demands. To obtain good print quality, printer, ink and paper manufacturers must work together in the understanding of ink–paper interactions which will guide them towards new developments and formulations of ink and paper coatings.

The coating of the inkjet paper plays an important role in the absorption of ink and consists basically of a pigment, normally alumina or silica, a binder which is usually polyvinyl alcohol (PVOH) and dye fixation agents which are normally cationic polyelectrolytes. The latter are expected to enhance the anchoring effect of the coating by electrostatic attractions as dye molecules normally have a negative charge. However, Svanholm in his dissertation [3] suggested that the effect of the cationic polyelectrolytes is due to a change in coating structure and not to any electrostatic interaction, and Vikman in her doctoral thesis [21] reported that evidence was found to prove that in anionic coatings, hydrogen bonds were responsible for the link between dye and paper coating, whereas FTIR spectroscopic data for cationic coatings gave indications of ionic bonding between the dye and the coating [29].

Other groups studying ink–paper interactions have used other approaches such as Yang [28] who performed a theoretical analysis of the effect of ink penetration on the reflectance of the printed sample and Lindqvist et al. who used techniques such us X-Ray Photoelectron Spectroscopy, profilometry, dynamic contact angle and critical surface tension measurements [34] to characterise the printing substrate in terms of surface energy and roughness, two important factors influencing ink-setting profile and ink adhesion.

Although a great effort is being made in this area, still the ink absorption mechanism is not completely understood and more studies have to be carried out to be able to discover the truth about paper–ink interactions.

7.1.2 Fluorescence Lifetime Imaging Microscopy (FLIM)

In this Chapter, the intrinsic fluorescence of the dyes and some paper-coating components is exploited to study their fluorescence lifetime using Confocal Fluorescence Lifetime Imaging Microscopy (FLIM). The aim of this study has been to evaluate the effectiveness of the FLIM technique to study dye-paper interactions and therefore help ink and paper manufacturers formulate new products, by understanding the fixation mechanism. This technique allows us not only to map fluorescence lifetimes in an X–Y area but at different depths within the sample. Because the fluorescence lifetime is sensitive to the environment, the analysis and interpretation of the fluorescence lifetime results can give an idea of the possible dye–paper interactions in different regions of the printed sample.

To explore the usefulness of the FLIM technique for studying inkjet ink–paper interactions, sets of printed samples were prepared using a well studied dye, Rhodamine B (RhB), as the principal component of the ink. Six different types of inkjet papers were chosen for this study, two commercially available inkjet papers and four specially manufactured by FFIC, with different values of pH. Five of these papers had a silica-based coating and the sixth had an alumina-based coating.

The fluorescence lifetime (τ) of the RhB has been reported by Ryder et al. [35] to be independent of pH, in the 6.0 to 8.0 range, with a value of 1.8 ns in aqueous solution and by Magde [36] as 1.68 ns. A time-resolved fluorescence anisotropy study done by Smith et al. [37] showed that the fluorescence lifetime of RhB when adsorbed into colloidal silica

(Ludox) exhibits a two-component fluorescence decay curve with values of 1.6 ns and 3.65 ns. This suggested that some of the RhB molecules exist as free RhB in solution with a fluorescence lifetime of 1.6 ns and some are adsorbed or dynamically restricted by the silica, increasing the fluorescence lifetime to 3.65 ns. When the amount of silica added increases the pre-exponential factor A indicates a higher contribution from the component with longer lifetime. These results were in agreement with previous photophysical studies [38] showing that restriction on intra-molecular dynamics of RhB can reduce non-radiative processes and therefore increase the fluorescence lifetime. They measured fluorescence lifetimes (τ) of RhB in solvents with different viscosity, obtaining a τ of 3.6 ns for a solution of RhB in glycerol and 5.1 ns for a film of RhB and PVA. Qian et al. [39] state that RhB molecules lose mobility and are isolated when adsorbed into the tiny pores of the microporous silica network which reduce the rotational diffusion of the RhB molecule and therefore increase the τ. They reported a τ of 4.2 ns after heating the silica gel and trapping the RhB. El-Rayyes [40] reported a fluorescence lifetime value between 2.2 and 3.4 for RhB absorbed in a meso-porous silica network. Negishi [41] reported that the lifetime of RhB in silica obeys a bi-exponential function with τ_1 0.9 ns and τ_2 3.48 ns showing a similar behaviour to that observed by Smith [37]. Mchedlov-Petrossyan [42] reported a τ of 5.1 ns for RhB adsorbed in substrates rich in OH- groups as PVA, and del Monte [43] reported J-Dimers of RhB with values of τ between 4.1 and 5.5 ns within doped gel glasses with high dye concentrations. Kemnitz et al. [44] studied the site-dependent fluorescence lifetime of isolated RhB molecules adsorbed on organic single crystals and other substrates such as fused quartz plates and reported a bi-exponential decay for RhB when absorbed by these crystals with a τ_1 of 0.7 ns and τ_2 of 3.2 ns. They suggested that the crystal surface itself is not homogeneous and has some distorted (not flawless) and some ideal sites for the RhB to be adsorbed. The longer fluorescence lifetimes were attributed to the adsorbed molecules at the ideal sites, as in these locations the interaction between dye and substrate seems to be the maximum.

The fluorescence lifetime of RhB in alumina was studied by Itoh et al. [45] and reported to be mainly 3.5 ns but occasionally a second component was detected with a higher fluorescence lifetime value of the order of 6.7 ns or even longer. No literature was found with information regarding fluorescence lifetimes of inkjet coatings.

7.2 Experimental details

7.2.1 Inkjet ink

Rhodamine B was used as an environmental probe to study the micro-structural behaviour of an inkjet system. Rhodamine is a xanthene dye and was chosen for this study, because it is a very well studied fluorescent dye due to its multiple applications such as a staining probe in biology, sensitizer, tracing agent, and as a photo-chromic and thermo-chromic agent, among many more [36]. The chemical structure of this organic dye, shown in Figure 7-1, is similar to some of the dyes used in the manufacture of inkjet inks.

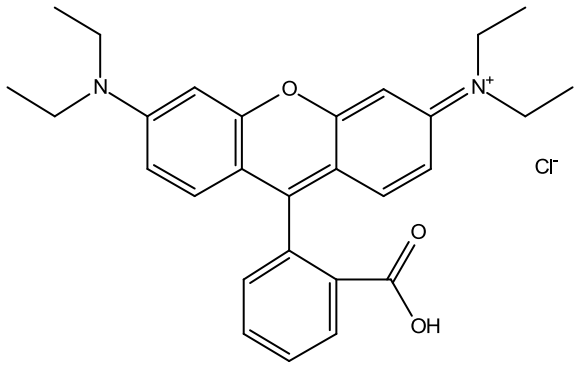

Figure 7-1 Chemical structure of Rhodamine B.

The Rhodamine B (RhB) was obtained from Sigma-Aldrich, Inc. The solutions used to measure the lifetime of RhB at different pH, were made with deionised water at a concentration of 3.8×10^{-6} M. The pH of the solutions was adjusted with either HCl (0.12M) or NaOH (0.02M).

The fluorescence spectrum of RhB in water shows a fluorescence emission maximum at 625 nm when excited at 540 nm.

The ink was formulated and prepared at Fujifilm Imaging Colourants (FFIC). A typical ink formulation is described in Table 7-1.

Ink Vehicle	
	%
Glycerol	7.50
Ethylene glycol	7.50
Urea	7.50
Surfynol 465	1.00
water	76.50
total	100.00
Ink	g
Ink vehicle	9.65
dye	0.35
total	10.00

Table 7-1 Composition of the RhB ink.

7.2.2 Inkjet coated papers

Six different papers were analysed, two commercially available and four manufactured by FFIC for research purposes.

PAPER	TYPE	NUMBER OF LAYERS SUGGESTED BY ANALYSIS		COMPOSITION		pH
A	MICROPOROUS	5	1	40 μm Alumina + trace organics		6.2
			2	5 - 10 μm Ti, O, Al, Si, C and possibly Na present could suggest and organic with TiO2 and mixed inorganics as fillers		
			3	160 mm Cellulose		
			4	5 - 10 μm Ti, O, Al, Si, C and possibly Na present could suggest and organic with TiO2 and mixed inorganics as fillers		
			5	25 μm Alumina + trace organics incl. Cl + possibly Na		
B	MICROPOROUS	4	1	37 μm Silica + polythene binder with traces of aluminium		3.4
			2	37 μm Cellulose with fine dispersion of titania		
			3	230 μm Cellulose		
			4	37 μm Polythene		
Fuji 8.0		n/a		Silica		8.0
Fuji 6.2		n/a		Silica		6.2
Fuji 4.8		n/a		Silica		4.8
Fuji 3.8		n/a		Silica		3.8

Table 7-2 Inkjet papers used in this work, type, composition and thickness of layers and pH.

Paper A had an ink-receiving layer based in alumina and paper B based in silica, representing the most common commercially used substrates. The FFIC papers are silica based, specially chosen for this work to allow the comparison between different pH media.

7.2.3 Inkjet printed samples

All the samples were printed using a Canon S 800 printer. The printed samples analysed had 100% and 10% colour density. The 10% colour density sample, allows the observation of the single ink dots under the microscope.

7.2.4 Experimental set-up: 2P-FLIM

The 2P-FLIM equipment described in Chapter 4, consisting of a CLSM Biorad 2000 System, a Becker and Hickl card SPC_730, a tunable Ti: sapphire laser and a PMT detector, was used.

The fluorescence lifetime of a solution of RhB in water (3.8×10^{-6} M) was measured initially and this value was compared with that obtained within the samples. Both types of printed samples were analysed, in the RhB fluorescence wavelength range, creating maps indicating fluorescence lifetime values in each pixel of the image. Additionally fluorescence lifetime measurements were made at different depths within the sample. These fluorescence lifetime maps will show how the environment affects the excited state decay mechanisms of the RhB.

The fluorescence lifetime maps were acquired for all the inkjet papers printed with the RhB-based ink using an excitation wavelength of 920 nm, two-photon excitation, and an emission filter between 600 and 650 nm with the aim of collecting the emission suspected to be of the RhB dye (emission spectra of printed papers in Appendix III). The laser energy was 1 mW, an acquisition time of 60 s/frame and the final image was the average of three cycles. The average count rate was of the order of 10^6 photons/s. The inverted microscope was used with a PA x 20 dry objectives. For the 100% colour intensity samples, various fluorescence intensity images were recorded at different depths within the sample. The surface of the paper was identified using the confocal microscope in the reflectance mode.

The lifetime data was analysed with the SPCImage software provided by Becker and Hickl (BH) using the non-linear least squares analysis and the selection of the best fit is based on

the value of χ^2 (chi square) and randomness of the residuals. A maximum χ^2 value of 1.45 is considered acceptable for this study.

7.3 Results and Discussion

7.3.1 FLIM of Rhodamine B in solution

The fluorescence lifetime of Rhodamine B in aqueous solution (3.8×10^{-6} M) was recorded in the 2P-FLIM equipment by placing the solution in a hollow rectangular capillary manufactured in borosilicate glass. The image size was 512 x 512 pixels, had 256 time channels and an average count rate of 10^6 photons / s. The data was recorded by the 2P-FLIM system and analysed using the SPCImage software is shown in Figure 7-2. The top left image corresponds to an intensity image; the top middle is a fluorescence lifetime colour-coded map which has a blue cross-hair pixel indicator and the top right, shows the associated histogram indicating the distribution of the lifetime values. The mean value of the distribution, marked by the small white cross-hair and the two white vertical cursor lines, includes 66% of all values found in the region of interest [46]. The lifetime measured for the RhB was between 1.64 and 1.70 ns with an average value of 1.67 ns +/- 0.03 ns which is in good agreement with the τ of 1.6 ns reported by Smith [37] and 1.68 reported by Magde [36], and smaller than that reported by Ryder of 1.8 ns [35]. The "Decay Graph" located beneath illustrates the photon decay data (blue), trace of the fit (red) and response function (green), and the deviations between these, are represented by the residuals at the bottom of the image. The decay curve for the pixel marked by the blue cross-hair has a χ^2 value of 1.30 and a τ of 1.67 ns. The residuals shown under the decay curve illustrate the satisfactory fit of the curve, evident by the evenness of the residuals across the whole decay.

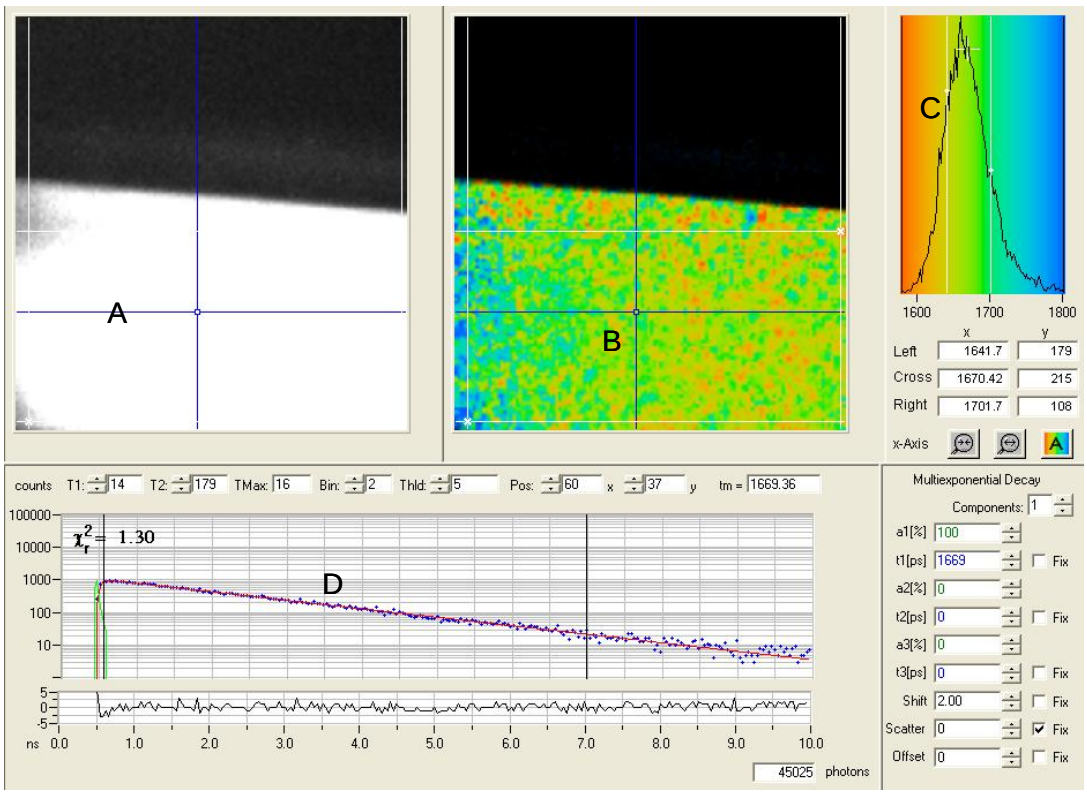

Figure 7-2 SPCImage data obtained for Rhodamine B; intensity image (A) in solution, colour-coded lifetime image showing the cross-hair indicator in blue and the ROI in white (B), associated histogram (C), decay curve at the selected pixel (blue), the best fitted curve (pink) (D), the response function in green and residuals (E). Lifetime range shown is between 1.64 and 1.70 ns with an average of 1.67 ns +/- 0.03 ns.

7.3.2 RhB-based ink on paper

7.3.2.1 Paper A

Paper A has a microporous ink-receiving layer based in alumina with a thickness of 40 µm. A fluorescence lifetime map of the sample was recorded for various depths starting from the surface considered as 0 µm and finishing at 40 µm. The best fluorescence lifetime decay curve fitted, for all the images, corresponds to a bi-exponential function decay. Fluorescence lifetime maps and their associated histograms for the image recorded at 20 µm are shown in Figure 7-3, where the FWHM for τ_1 lies between 1.19 and 1.71 ns and for τ_2, the histogram, shows three peaks: the predominant one between 3.24 and 3.55 ns, the second one between 3.78 and 4.03 ns and the third one with very low counts between 4.42 and 4.69 ns.

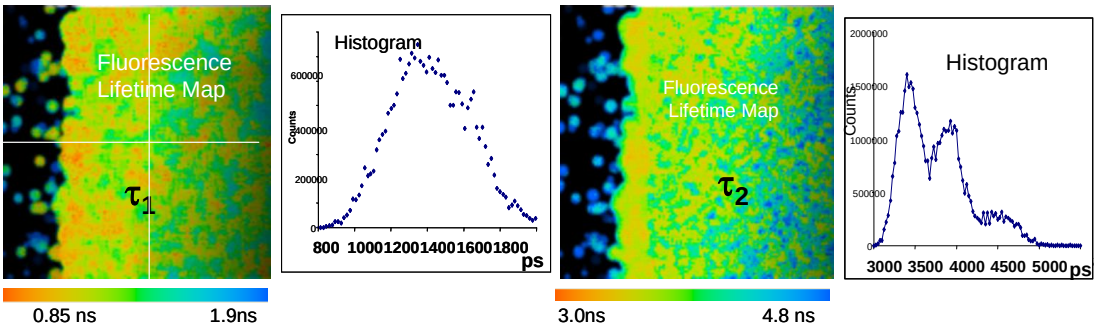

Figure 7-3 Fluorescence lifetime map of a printed sample of paper A: for τ_1 and τ_2 and associated histograms recorded at 20 µm.

Figure 7-4 shows the decay curve and the residuals at the pixel indicated in Figure 7-3 (white cross-hair), with two lifetimes τ_1 (1.34 ns) and τ_2 (3.33 ns). The value of χ^2 (1.1) together with the randomness of the residuals corroborates the goodness of the fit.

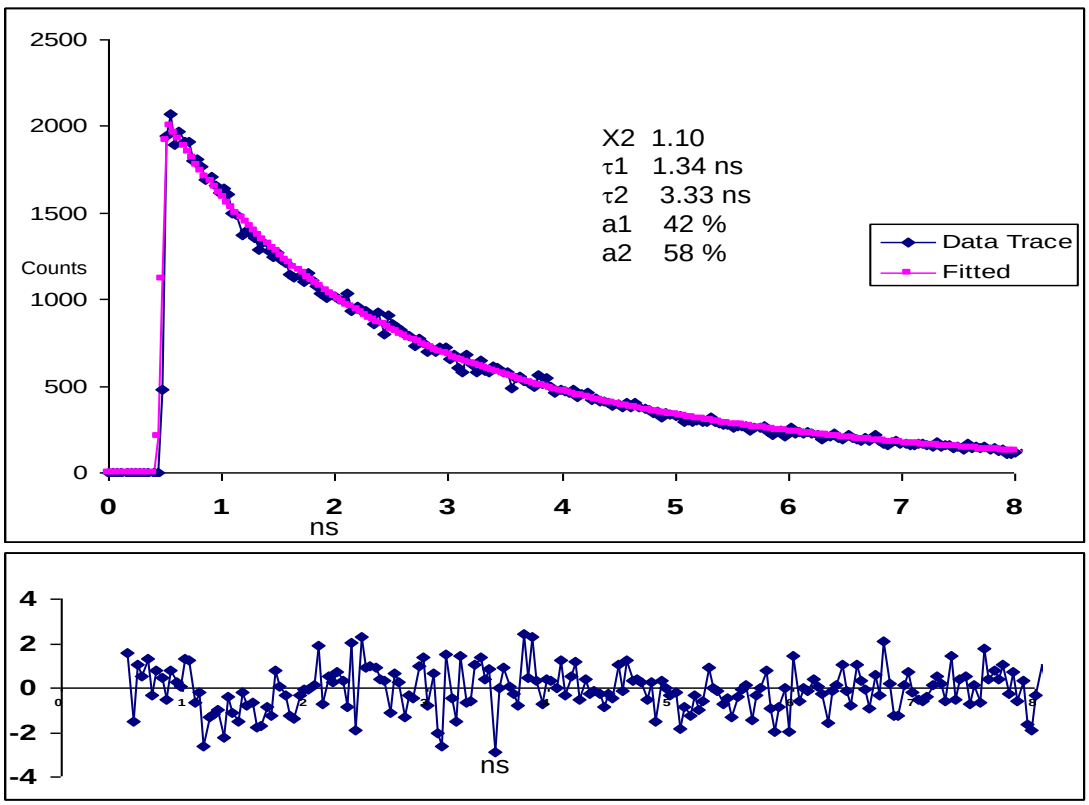

Figure 7-4 Fluorescence decay curve (blue), best fitted curve for two components (pink) and residuals. Sample of paper A printed at a single point (cross-hair in Figure 7-3).

As a heterogeneous microporous system the lifetime map shows the spatial variation in lifetimes. Although it seems that a very narrow blue line delimits the edge of the sample,

with a high fluorescence lifetime, the line is not as pronounced as it is for paper B analysed in the next section.

Figure 7-5 shows the decay parameters at three locations. It is important to note that the shorter values of τ_1 and τ_2 are found mostly near the edge.

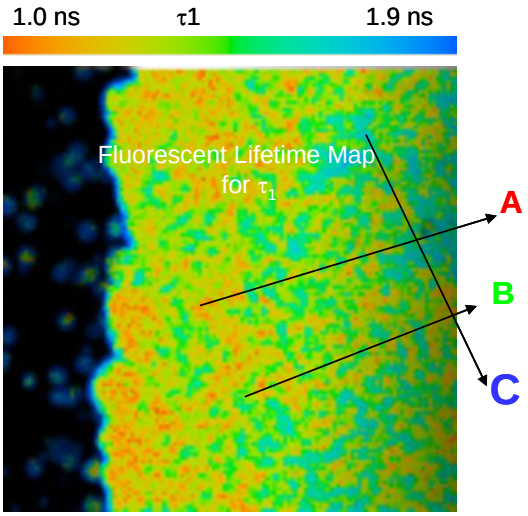

	τ_1	τ_2	a_1	a_2	χ^2
A	1.16	3.28	48	62	1.13
B	1.55	3.56	46	54	1.10
C	1.91	4.43	62	38	1.05

Figure 7-5 Fluorescence lifetime map showing τ_m, τ_1, τ_2, a_1, a_2 and χ^2 values for different points within the alumina-based ink-receiving layer.

To have a global view of the behaviour of the RhB in paper A, the analysis was done at 0, 10, 15, 20, 25, 30 and 40 µm of depth. In all cases a bi-exponential fluorescence decay curve was found. The histograms for τ_m,τ_1, τ_2 and a_1 at each depth are shown in Figure 7-6.

Analysing these histograms some interesting results can be highlighted. The distribution of the average lifetime τ_m in the first 30 µm within the paper can be described by a narrow peak which could suggest that the environment in this region is homogeneous with a τ_m around 2.6 ns. At 40 µm the τ_m is described by a wide peak with its maximum around 2.9 ns, the shape of the distribution histogram is completely different to the previous indicating the existence of a different environment in the region possibly the beginning of the second layer (Appendix II). The distribution of τ_1 is similar to τ_m. In general the value of τ_1 in the first 30 µm is around 1.5 ns, value that matches very well with the fluorescence lifetime of RhB free or not adsorbed. The situation at 40 µm again is different and the τ_1 is around 2.0 ns.

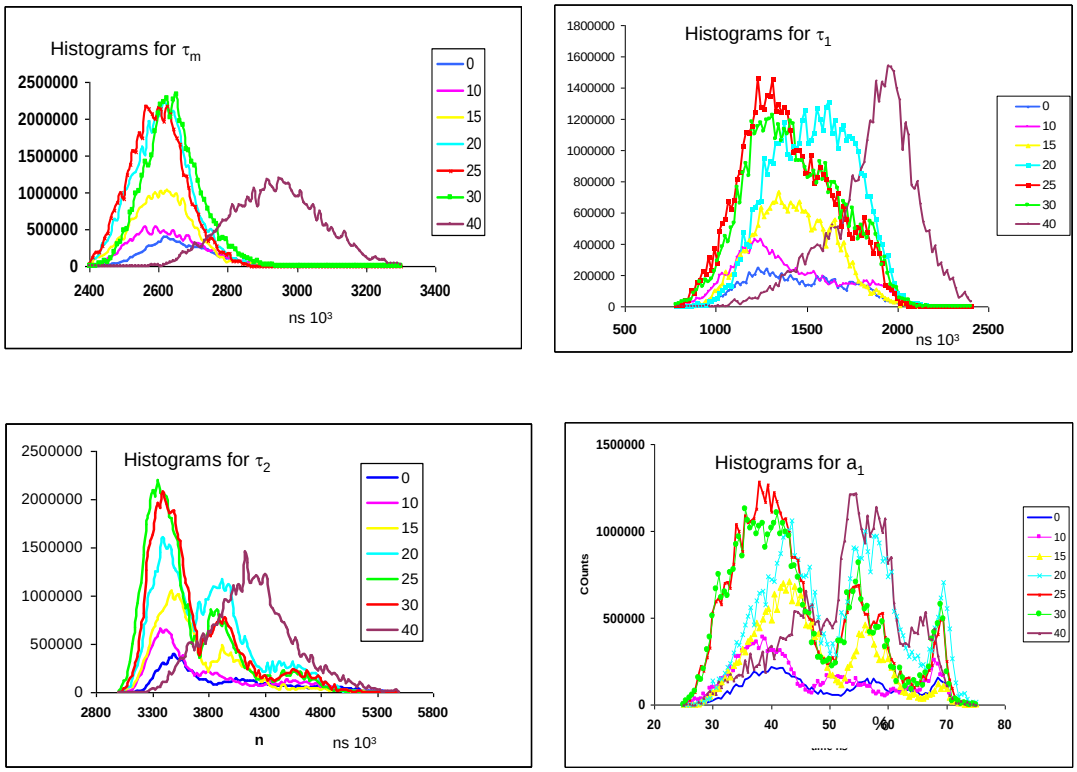

Figure 7-6 Histograms of fluorescence lifetime τ_m, τ_1, τ_2 and factor a_1.

The distribution of τ_2 is different, the histograms have three peaks: one around 3.4 ns, the second one around 3.9 ns and one small peak around 4.5 ns. All of them can be due to RhB adsorbed by silica in different ways. Again the situation at 40 µm in terms of τ_2 is dissimilar compared with the previous images. These results could be an indication that the ink is in contact with the second layer of the paper, which is a mixture of TiO_2 with some organic and inorganic fillers, therefore is a different environment which seems to be very uniform as the shape of the histograms denotes.

The data illustrated in Figure 7-6 are summarised in Table 7-3, from where it can be deduced that the average τ_1, within the first 30 µm of the sample, is around 1.4 ns which shows the existence of RhB molecules with a high degree of mobility that have not been adsorbed completely. The proportion of τ_1 is variable depending on the precise position on the sample but overall can be considered as being around 40%. This suggests that the amount of RhB adsorbed is greater than that in a free state or with a higher degree of mobility.

Depth µm	τ_{1} ns FWHM	ns Average	τ_{2} ns FWHM	ns Average	a_{1} % FWHM	% Average
0	1.17 – 1.89	1.50	3.34 – 3.68	3.50	37 – 59	46
0			3.90 – 4.31	4.10		
0			4.40 – 4.08	4.60		
10	1.09 – 1.89	1.39	3.26 – 3.57	3.42	34 – 58	43
10			3.83 – 4.01	3.94		
10			4.01 – 4.60	4.30		
15	1.20 – 1.67	1.43	3.25 – 3.60	3.42	35 – 60	46
15			3.84 – 4.14	3.99		
15			4.61 – 4.96	4.73		
20	1.19 – 1.71	1.43	3.24 – 3.55	3.39	35 – 45	40
20			3.78 – 4.03	3.90		
20			4.42 – 4.69	4.56		
25	1.17 – 1.67	1.39	3.24 – 3.54	3.39	36 – 49	43
25			3.81 – 4.08	3.93		
25			4.44 – 4.73	4.58		
30	1.27 – 1.60	1.45	3.34 – 3.61	3.48	34 – 50	41
30			3.83 – 4.13	3.98		
30			4.53 – 4.74	4.64		
40	1.60 – 1.21	1.85	3.82 – 4.52	4.18	40 – 61	49

Table 7-3 FWHM of τ_1, average τ_1, FWHM of τ_2, average τ_2, FWHM of a_1 and average a_1 at 0, 10, 15, 20, 25, 30 and 40 µm.

In conclusion it can be said that the fluorescence lifetime of RhB when printed in paper A displays a double exponential curve through the entire ink-receiving receiving layer. The two lifetime components are τ_1 of approximately 1.5 ns and τ_2 of approximately 3.5 ns which coincide with the value of free RhB and adsorbed by alumina [45] The presence of this longer lifetime component can be attributed to an interaction between RhB and alumina and maybe other molecules in the paper that affects the non-radiative decay and indicates the existence of a highly constrained environment.

Figure 7-7 shows lifetime maps of τ_1 as a function of depth. The distribution of τ_1 is homogeneous in the first 30 µm as discussed above. The change in τ_1 at 40 µm is clearly seen.

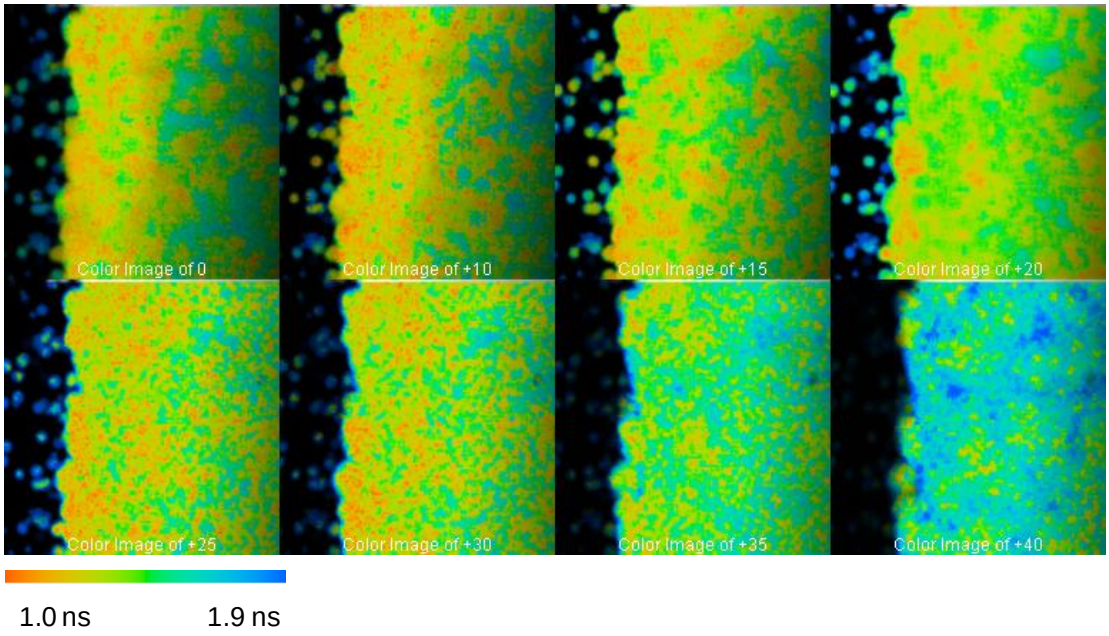

Figure 7-7 Fluorescence lifetime maps for τ_1 at 0, 10, 15, 20, 25, 30, 35 and 40 µm.

7.3.2.2 Paper B

Measurements of a sample printed with RhB-ink with 100% colour intensity were recorded at various depths within the sample starting at the surface (0 µm), identified by the reflectance mode in the CLSM, until a depth of 40 µm where the ink-receiving layer ends. Figure 7-8 shows the intensity image, average fluorescence lifetime (τ_m) map, associated histogram decay curve and the decay parameters recorded at 15 µm depth, for the pixel denoted by the blue cross hair.

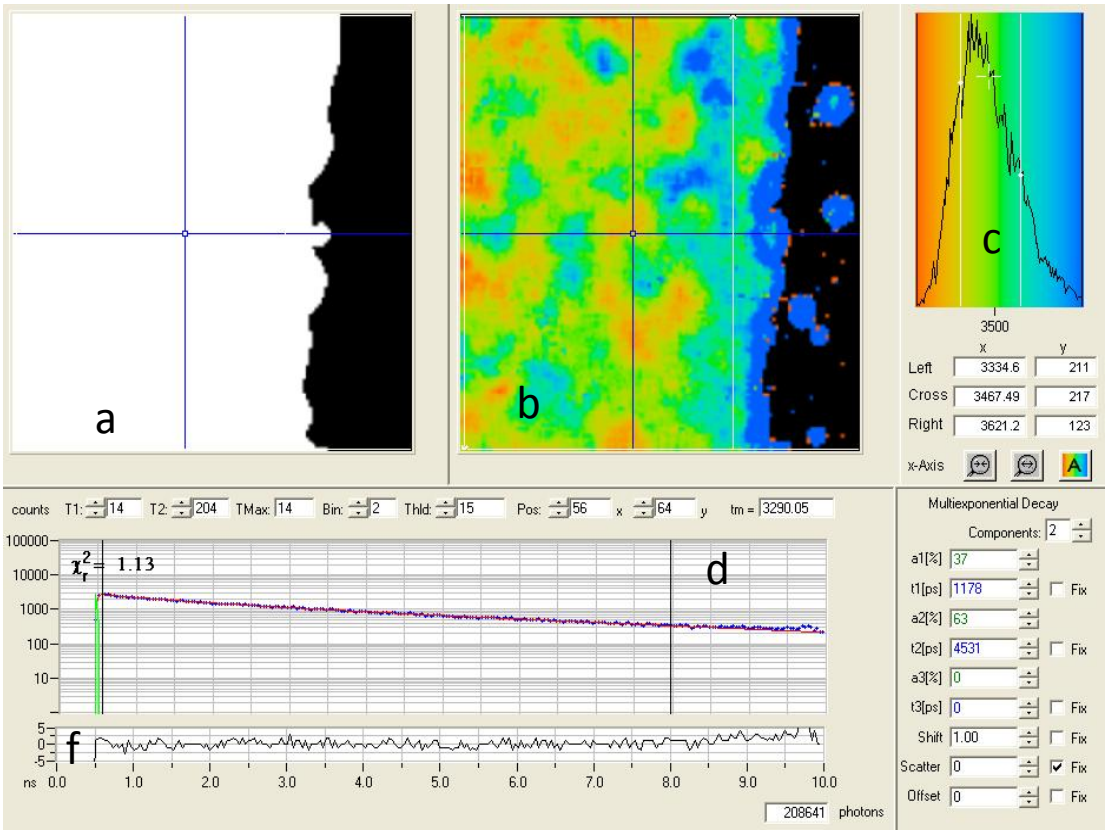

Figure 7-8 SPCImage data obtained recorded at 15 µm depth, Paper B: Intensity image (a), average fluorescence lifetime map τ_m (b), excited at 920 nm (two-photon excitation) and emission collected between 600 and 650 nm, the associated histogram (c), decay curve at the selected pixel (blue), the best fitted curve (pink) (d), the response function in green and residuals (e). A bi-exponential decay is the best fit for the pixel selected with a τ_1 of 1.17 ns and amplitude of 37% and a τ_2 of 4.53 ns with amplitude of 63%.

As can be observed, the paper is a complex and heterogeneous system showing different values of fluorescence lifetime at different points in the lifetime image (b) as could be expected for a silica-based substrate with a nanoporous micro-structure. Therefore it is best analysed using the fluorescence lifetime histogram (D) which shows the tendency of the fluorescence lifetime over the whole image. The paper by itself proved to be non-fluorescent under the conditions employed as the unprinted part of the paper shows no fluorescence intensity. The fluorescence lifetime map shows that the edge, where the printer starts each row, presents a longer fluorescence lifetime. The blue dots in the non-printed part of the sample correspond to satellite drops which are ink droplets that were ejected by the print head and deposited in the wrong position. A bi-exponential decay is the best fit for the pixel selected (blue cross-hair) with τ_1 of 1.17 ns and amplitude of 37 % and τ_2 of 4.53 ns with

an amplitude of 63%. The value of 1.13 for χ^2 corroborates the goodness of the double exponential fit.

The behaviour observed at the selected pixel suggested that the whole image displays a by-exponential decay. Figure 7-9 illustrates the fluorescence lifetime map for τ_1 together with the associated histogram for the whole image. The fluorescence lifetime, τ_1, varies between 1.03 and 1.32 ns with an average of 1.16 ns +/- 0.16 ns.

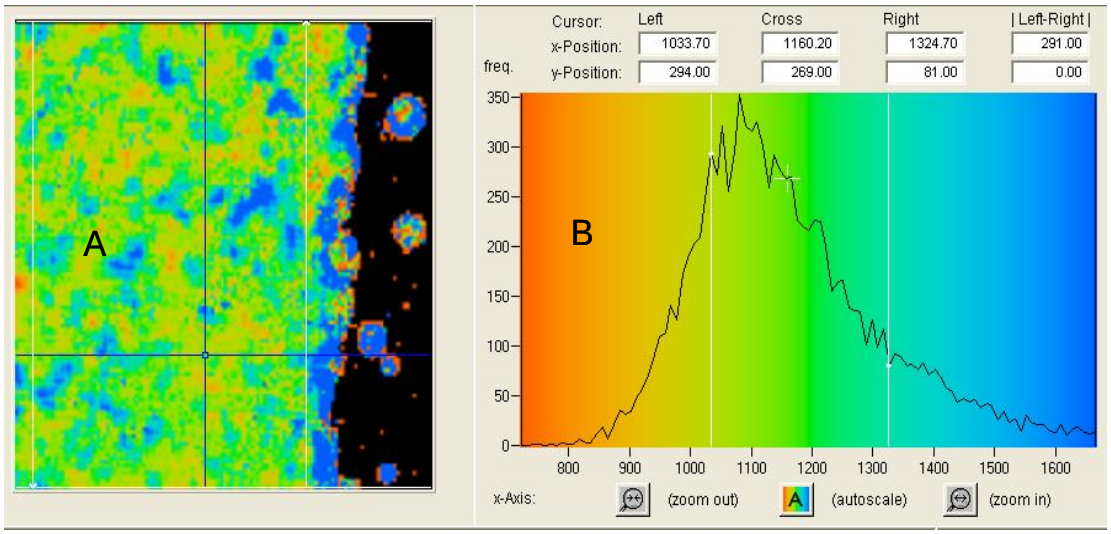

Figure 7-9 Fluorescence lifetime maps (a) and associated histograms (b) for τ_1 at 15 µm.

Fluorescence Lifetime, τ_2, varies between 4.50 and 4.96 ns with an average of 4.7 ns +/- 0.20 ns as shown in Figure 7-10.

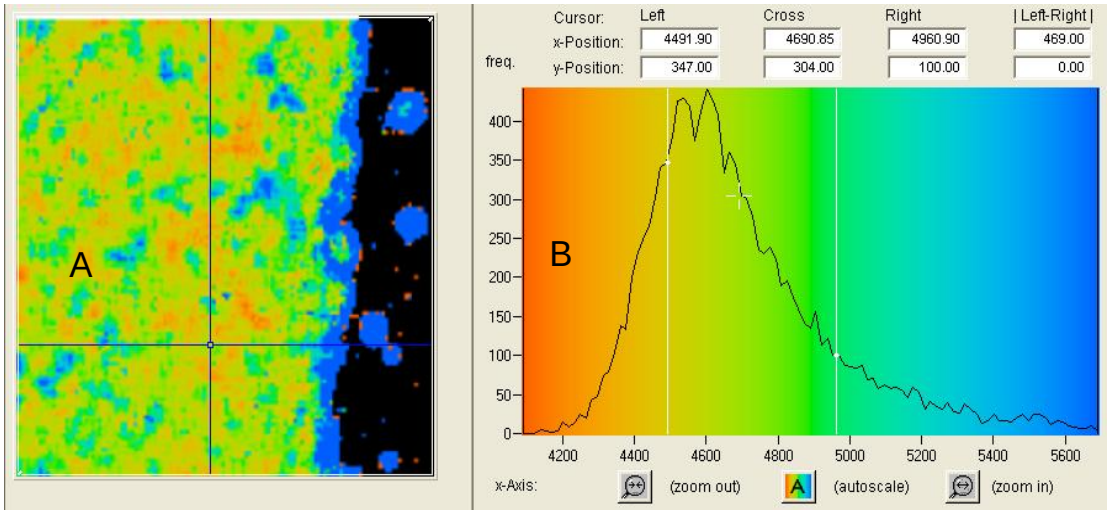

Figure 7-10 Fluorescence lifetime maps (a) and associated histograms (b) for τ_2 at 15 µm.

Figure 7-11 shows the distribution map of the relative amplitude or a_1 factor, with a value between 30 and 38%, an average of 34% +/- 4 %, indicating that at this depth the population of excited molecules responsible for τ_1, is present in less proportion than that exhibiting a longer value of fluorescence lifetime τ_2.

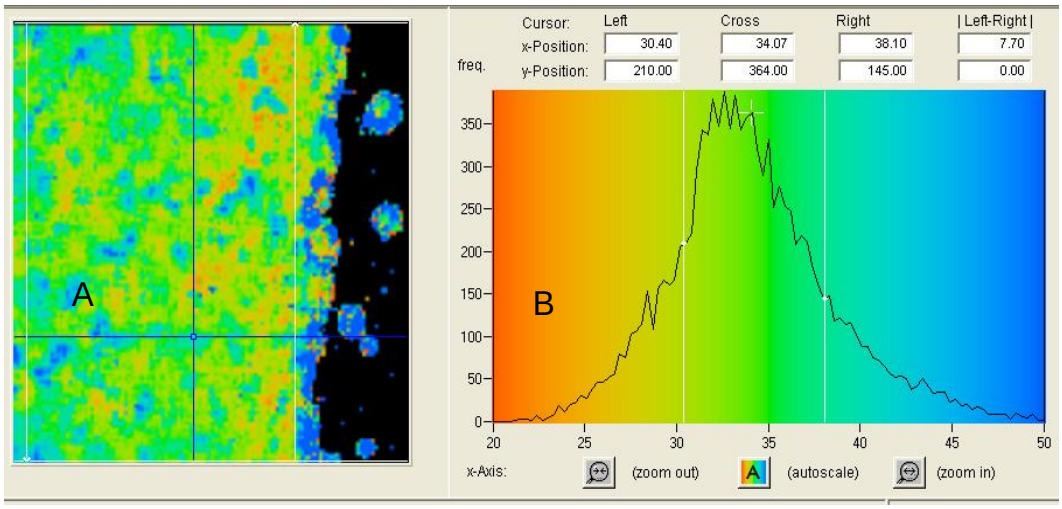

Figure 7-11 Fluorescence lifetime maps (a) and associated histograms (b) for a_1 at 15 µm.

The distribution of χ^2 shown in Figure 7-12 confirms the goodness of the fit for the bi-exponential decay as 66% of value of its value lies between 1.1 and 1.3.

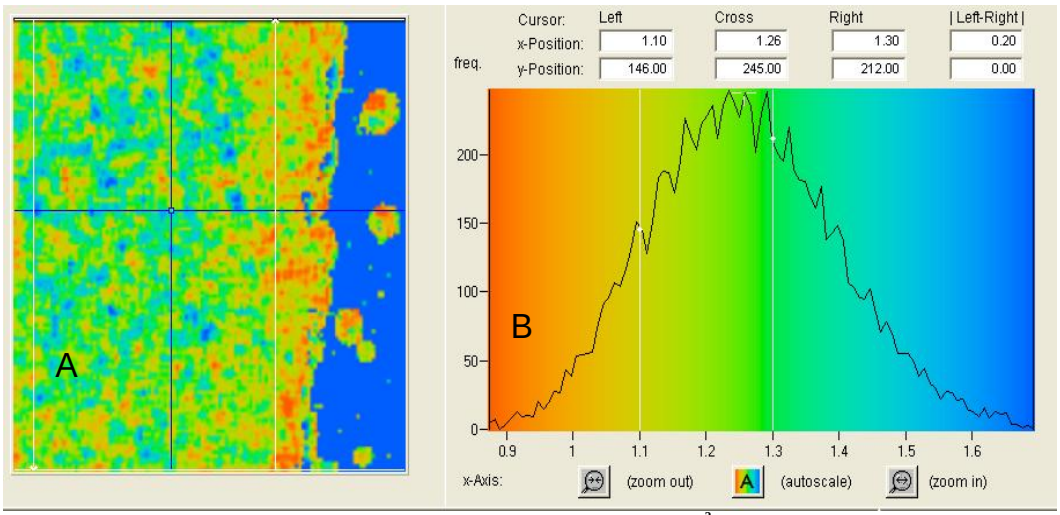

Figure 7-12 Fluorescence lifetime maps (a) and associated histograms b) for χ^2 at 15 µm.

To have a global view of the behaviour of RhB, when printed, is important to analyse its fluorescence lifetime at different depths of penetration within the sample. For this reason the same analysis was made at seven depths 0, 5, 10, 15, 20, 30 and 40 µm. All of them

displayed a bi-exponential fluorescence decay curve. The associated histograms of the fluorescence lifetimes observed at each depth are shown in Figure 7-13. The fluorescence intensity was very low at 40 µm so it was not included in the analysis. It is important to mention at this point that the surface of the paper was identified using the CLSM (reflectance mode) and because the lasers of the confocal are not aligned exactly at the same point as the Ti:sapphire laser, some degree of error will exist in the detection of the surface.

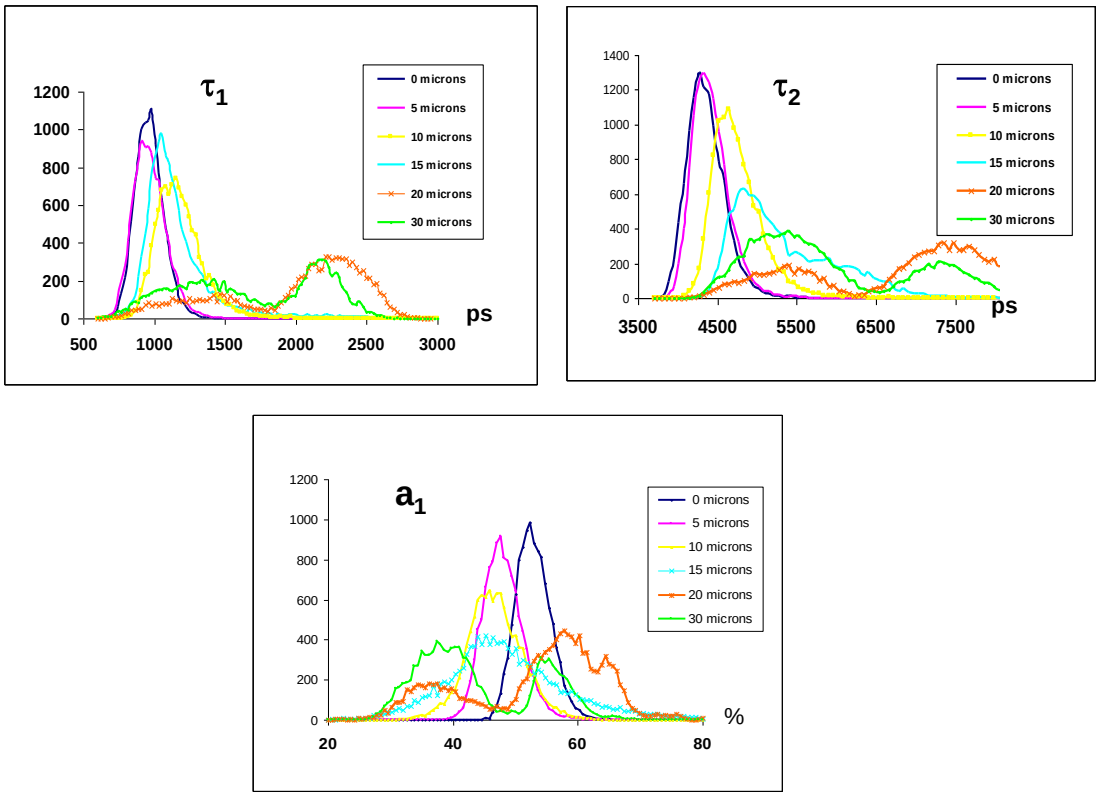

Figure 7-13 Histograms of τ_1, τ_2 and a_1 at different depths.

Between the surface and 15 µm, τ_1 and τ_2 histograms each showed a single peak, however, above 15 µm, two peaks are present for each lifetime component. Figure 7-14 shows the image recorded at 20 µm, the colour-coded map and associated histogram for a_1, with two clear peaks visible one around 40% and the other one around 60%, indicating the existence of two regions with different a_1.

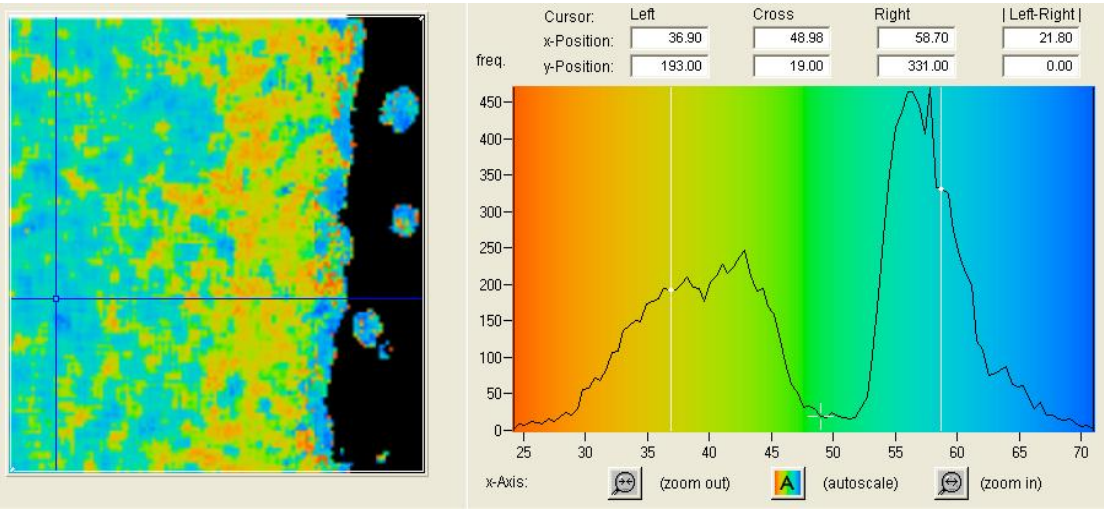

Figure 7-14 Colour-coded map and associated histogram for a_1.

If the colour-coded map is analysed in different regions as shown in Figure 7-15, two regions can be identified: one very near the edge of the paper with a_1 between 35 and 45%, and a τ_1 around 1.4 ns and a second one with a_1 between 55 and 65 % approximately, covering the majority of the printed part of the paper with a τ_1 around 2.1 ns. This can be explained by the fact that near the edge the amount of ink is higher and some RhB exists as a free dye (τ 1.6 ns), while in the printed area the RhB is in a more constrained environment, decreasing the non-radiative decay and therefore increasing the lifetime.

Table 7-4 gives a summary of the lifetime range of τ_1, τ_2 and a_1 together with the average lifetime for each of them obtained for the different depths. In general paper B shows a bi-exponential decay, with a short τ around 1.3–1.4 ns and a longer τ at around 5.4 ns with some exceptions that will be discussed further.

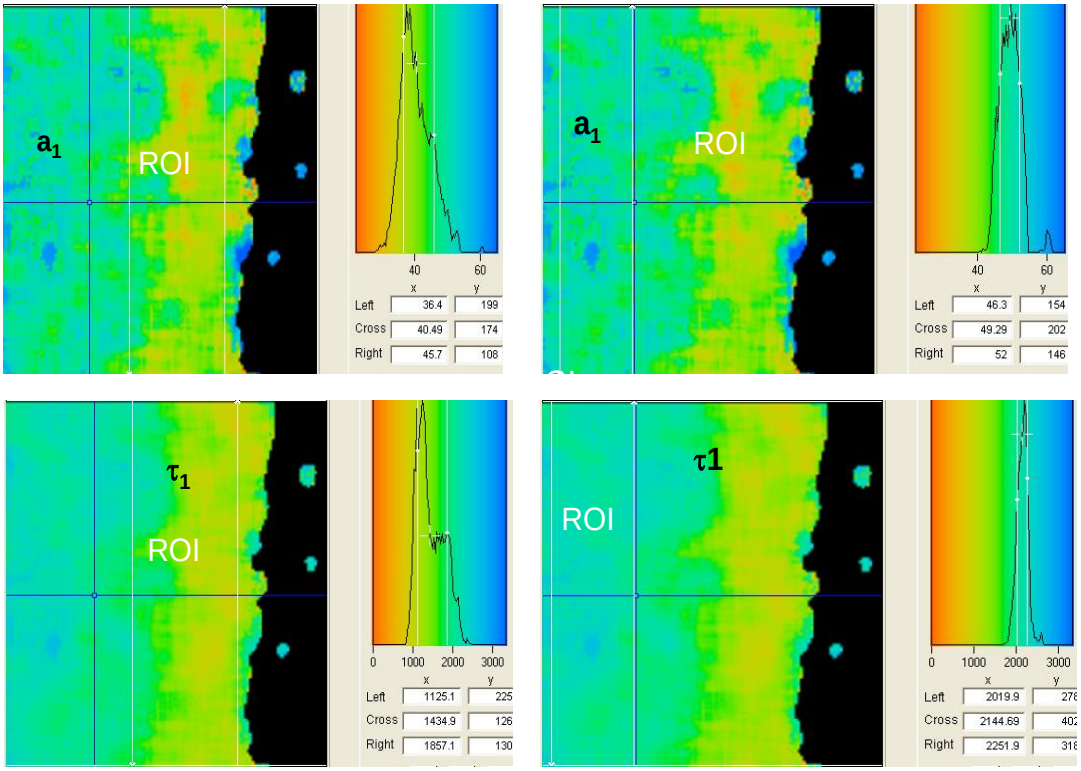

Figure 7-15 Colour-coded map for a_1 and τ_1 and the associated histograms in different regions of interest.

In the first 5 µm, the fluorescence lifetime distributions for τ_1 and τ_2 are very narrow and have shorter lifetime values than deeper in the paper. The value of the fluorescence lifetime τ_1 is around 1.0 ns with a very narrow distribution which means that the fluorescence lifetime value is very homogeneous in this section of the paper. The value of τ_2 is around 4.3 ns.

µm	τ_1 FWHM ns	ns	τ_2 FWHM ns	ns	a_1 FWHM %
0	0.90 – 1.04	0.97	4.18 – 4.51	4.34	50 – 54
5	0.92 – 1.16	1.04	4.28 – 4.75	4.50	46 – 53
10	1.37 – 1.71	1.53	4.90 – 6.09	5.40	50 – 63
15	1.03 – 1.32	1.16	4.50 – 4.96	4.70	30 – 38
20(1)	1.12 – 1.65	1.40	4.78 – 6.13	5.38	36 – 46
20(2)	2.01 – 2.25	2.10	7.26 – 8.08	7.65	46 – 52
30(1)	1.04 – 1.62	1.31	4.77 – 5.81	5.27	34 – 43
30(2)	1.94 – 2.22	2.08	6.94 – 7.84	7.36	54 – 60

Table 7-4 FWHM τ_1, average τ_1, FWHM τ_2, average τ_2 and FWHM a_1 at different depths within the paper.

Between 5 and 20 µm depth, the RhB molecules seem to have two lifetime components, one around 1.5 ns and a longer lifetime component around 5.0 ns. These results are agreement with previous studies of RhB adsorbed by silica [37].
In the region between 20 and 30 µm it seems that the RhB behave different near the edge than in the print itself. In the printed region, RhB have fluorescence lifetime values higher than the values obtained near the edge.

The intensity absence at 40 µm may well suggest that this image corresponds to the underlying cellulose and Ti layer in which there is no RhB.

To further visualise the variations in lifetimes within the paper, the FLIM images have been processed using the public domain Image J software [18]. Figure 7-16 shows consecutive τ_1 images obtained at 0, 5, 10, 15, 20, 30 and 40 µm depth, illustrating how the fluorescence lifetime values increase when penetrating the paper.

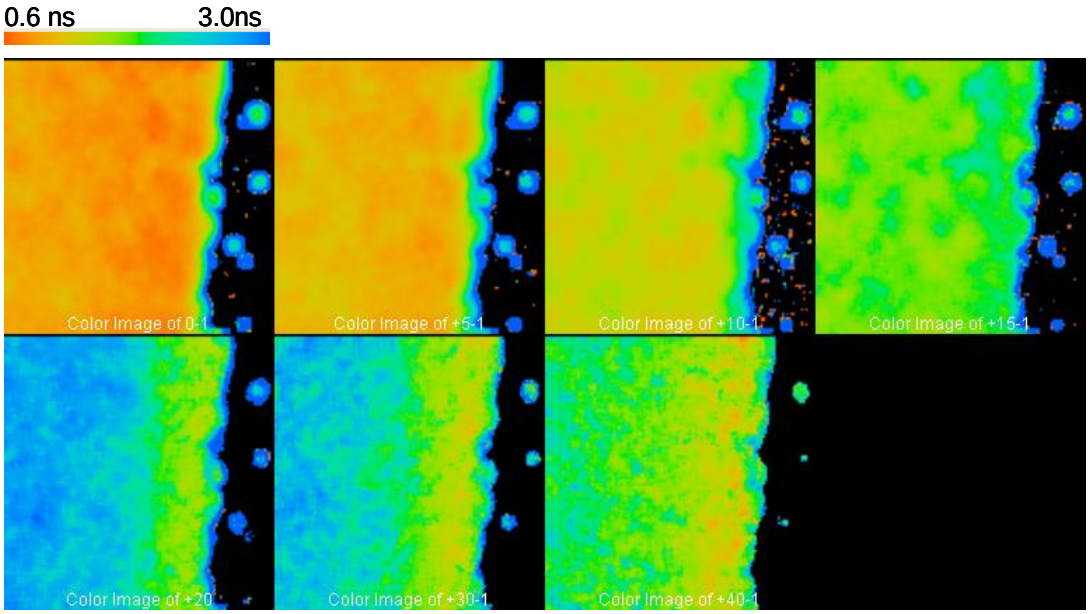

Figure 7-16 Fluorescence lifetime images of τ_1 at 0, 5, 10, 15, 20, 30 and 40 m depth.

Figure 7-17 and Figure 7-18 show 3-D representations of τ_1. The right image shows how τ_1 varies from the surface to inside the paper (LHS) while the figure at the left shows the inverse view. It can be observed that τ_1 with low value is located on the surface and increases with depth.

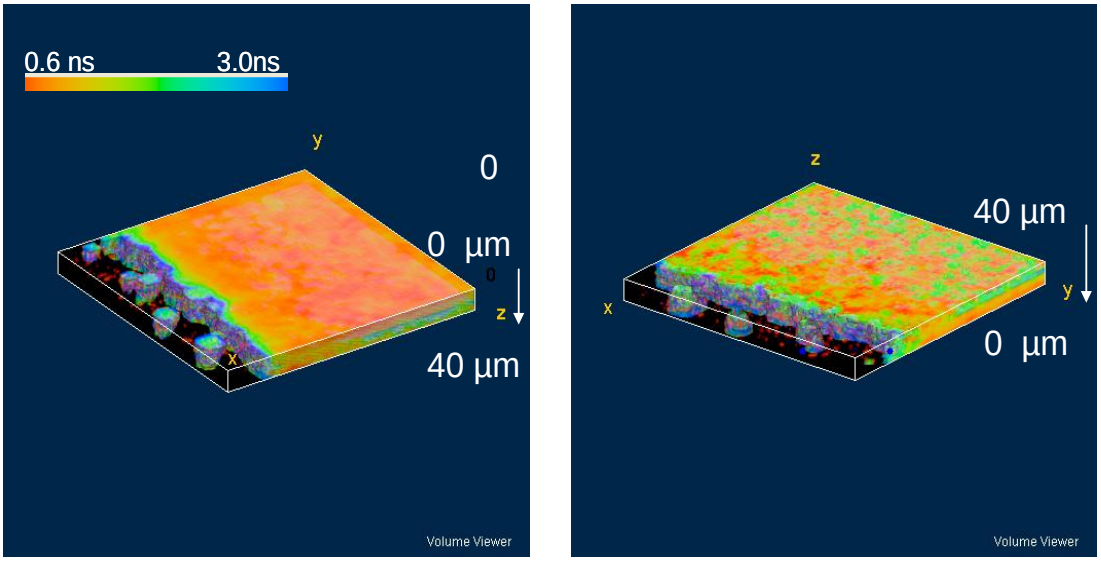

Figure 7-17 3-D images of τ_1, LHS view from the surface (0 µm) to deep into the paper (40 µm), RHS view from 40 µm to 0 µm.

In Figure 7-18 the cross-sections of the 3-D LHS view is shown for τ_1, revealing a uniform distribution inside the paper in xy but not xz.

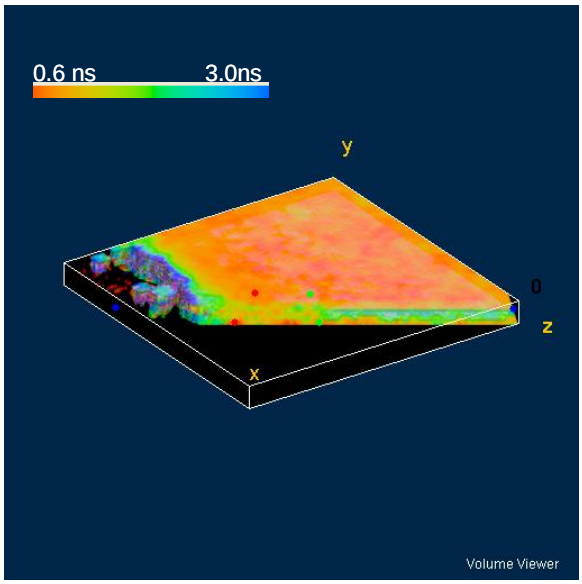

Figure 7-18 Cross-section of 3-D image for τ_1 from the surface (0 µm) to deep into the paper (40 µm).

The variation of τ_2 with depth shown in Figure 7-19 is similar to that observed with τ_1, the value increases as the ink penetrates the sample.

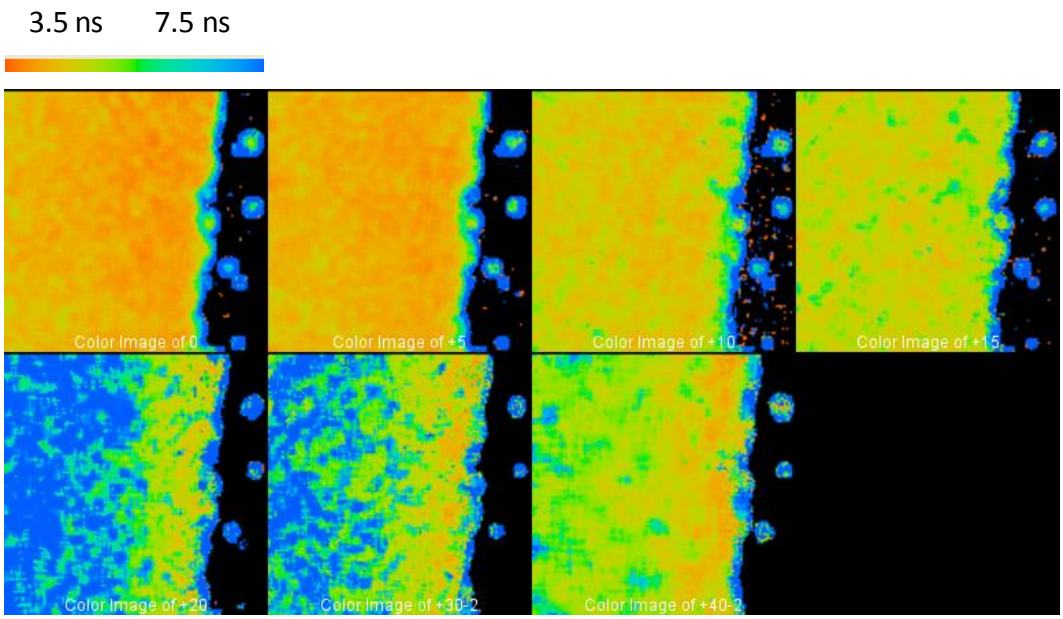

Figure 7-19 Fluorescence lifetime images of τ_2 at 0, 5, 10, 15, 20, 30 and 40 m depth.

Figure 7-20 is a scanning electron microscope (SEM) image of a printed sample of RHB-ink printed in paper B, it shows the silica network that constitutes the ink-receiving layer of paper B. The size of RhB is estimated to be about 10 A° [39] which could explain why the fluorescence lifetime maps of RhB printed in this paper are so heterogeneous as it can penetrate or be adsorbed in a different way through the whole silica network.

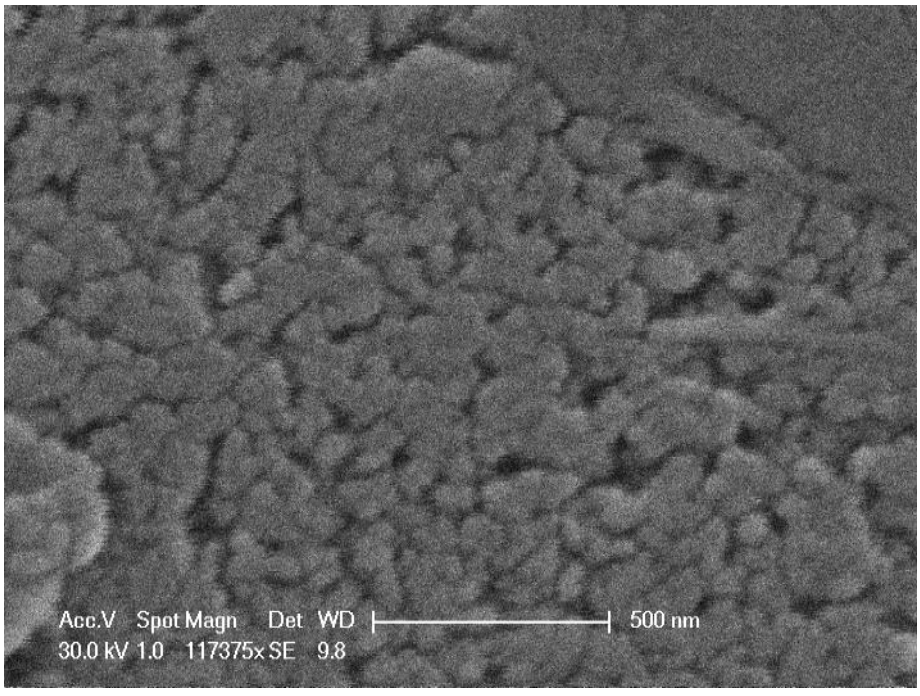

Figure 7-20 SEM image of a printed sample of RhB in paper B.

After the ink is absorbed the RhB molecules are isolated and gradually absorbed into the tiny pores of the silica network restraining in this way the rotational diffusion of the molecules and therefore decreasing the probabilities for the non-radiative energy transfer decay and increasing the fluorescence lifetime. The values of fluorescence lifetime obtained for RhB absorbed by the silica coating of paper B (and the other silica-based papers) are in good agreement with the reported in literature [39]. The presence of RhB molecules free has been proved as well, through its fluorescence lifetime value.

7.3.2.3 Silica-containing papers with different pH

7.3.2.3.1 RhB Solutions

Before analysing the papers it was necessary to verify that the emission spectra and lifetime of the RhB did not change with pH. For this purpose, aqueous solutions of RhB (3.8×10^{-6} M) at different pH (8.0, 6.2, 4.8 and 3.8) were prepared and analysed. The pH was measured using a Thermo Scientific Orion 3 Star^{TM} pH meter. Their emission spectra presented in Appendix III showed that the wavelength intensity did not change with pH.

Fluorescence decay curves were collected using an excitation wavelength of 400 nm, and emission wavelength of 585 nm. All the samples can be analysed globally to the same τ (1.61 ns) in accordance with the literature values [36]. The PH 3.8 solution showed a slightly shorter lifetime of 1.58 ns.

7.3.2.3.2 pH 8

The same procedure as with the previous samples was followed for this paper and images were recorded at different depths. However, the results obtained for this paper were dissimilar. The images did not all display the same exponential fluorescence decay function. At the surface and for the first 5 μm, two exponential fluorescent components were calculated for the best fitted curve, whereas at greater depths only one exponential component was found. Results for the surface layer are shown in Figure 7-21. The FWHM range for τ_1 is between 1.2 and 1.6 ns and for τ_2 between 4.1 and 4.7 ns. Suggesting the presence of free RhB (τ_1 1.4 ns) and trapped in the silica (τ_2 4.4 ns). The fluorescence lifetime values are very similar to those observed for the silica-based paper B.

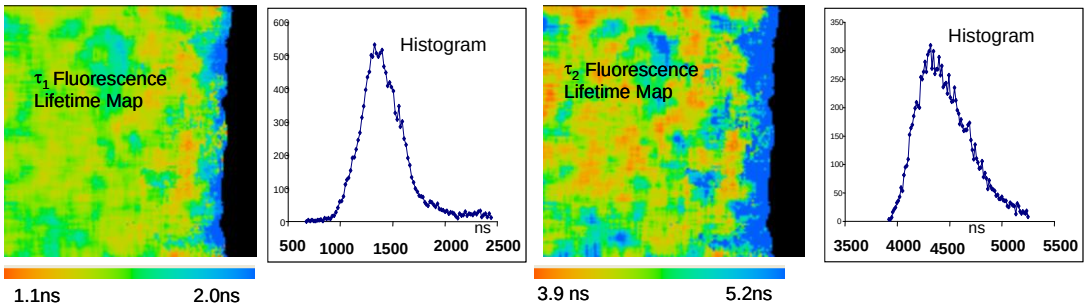

Figure 7-21 Fluorescence lifetime maps and associated histograms for τ_1 and τ_2 recorded at the surface of the paper.

The fluorescence histograms for the images obtained between 10 and 35 µm, shown in Figure 7-22, could be fitted with one exponential component with a fluorescence lifetime value between 4.2 and 4.5 ns, suggesting the absence of unconstrained free RhB within the paper.

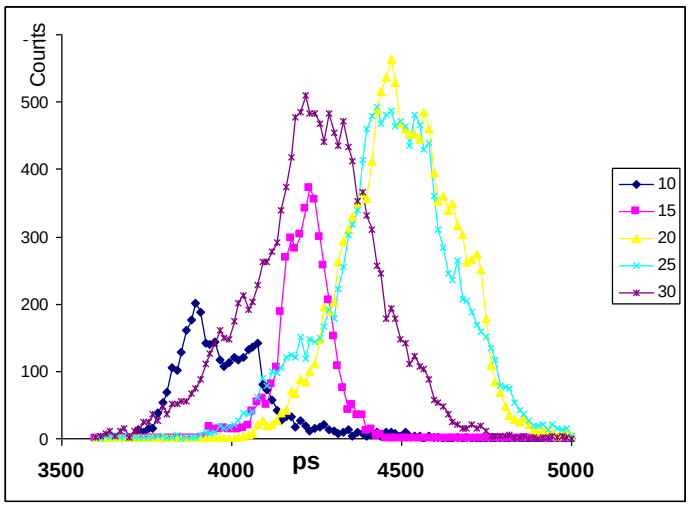

Figure 7-22 Fluorescence lifetime histograms for images between 10 and 35 µm.

7.3.2.3.3 pH 6.2

The lifetime histograms are shown in Figure 7-23. The pH 6.2 paper shows a bi-exponential decay between the surface and 15 µm with a τ_1 around 1.6 ns. Between the surface and 10 µm, τ_2 show a bimodal distribution with peaks at around 5.3 ns and 6.3 ns, whereas at 15 µm only a single peak is found at 5.5 ns.

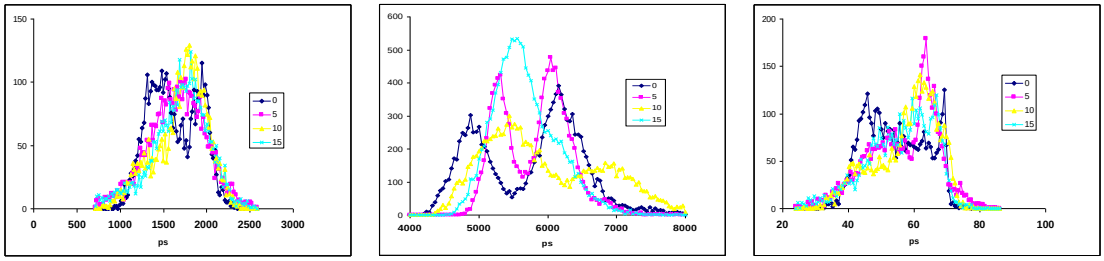

Figure 7-23 Fluorescence lifetime histograms for τ_1, τ_2 and a_1.

Between 20 and 45 µm there is only one decay component with an FWHM between 4.4 and 4.7 ns. Figure 7-24 shows the histograms for τ in this depth range. These values are similar to those observed for the pH 8 paper.

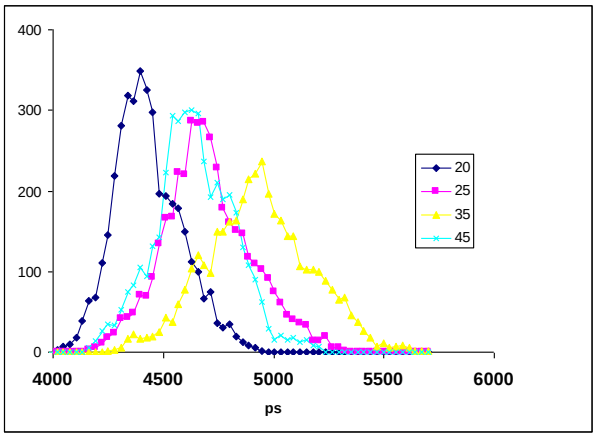

Figure 7-24 Fluorescence lifetime histograms for the images recorded between 20 and 45 µm.

The fluorescence lifetimes shown by this paper suggest the presence of free RhB and adsorbed on silica between the surface and 15 µm. The behaviour below 15 µm is indicative of RhB adsorbed on silica.

7.3.2.3.4 pH 4.8

This paper displays bi-exponential decay at all depths. The fluorescence lifetime maps are very homogeneous between the surface and 25 µm, but it seems that deeper into the paper between 35 and 45 µm, the environment is different giving longer fluorescence lifetimes.

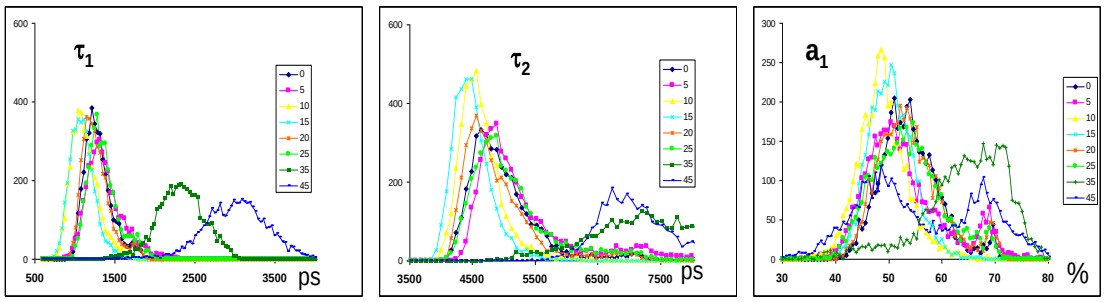

Figure 7-25 Fluorescence lifetime histograms for τ_1, τ_2 and a_1.

As shown in Figure 7-25, between 0 and 25 µm, the FWHM for τ_1 is between 1.1 and 1.5ns and for τ_2 between 4.6 and 5.1 ns. The a_1 histogram suggests that approximately 50% of RhB molecules are free, and 50% are absorbed on silica. The lifetime values obtained for the RhB adsorbed are very consistent in all the silica-based papers. In the region between 35 and 45 µm higher vales of τ are observed and although the composition of the paper is unknown, in terms of coating layers and thickness, it is clear that the RhB sees a different environment at this depth.

7.3.2.3.5 pH 3.8

This paper shows a bi-exponential decay at all depths. The distribution of lifetimes and a factor is essentially invariant with depth as shown in Figure 7-26. The longer lifetime τ_2 (3.3 – 3.5 ns) is consistent with RhB absorbed on silica, as seen previously, but τ_1 (0.5 – 0.65 ns)is much shorter than for free RhB in previous samples. This suggests that non-radiative decay of free RhB is accelerated in acidic conditions in this environment.

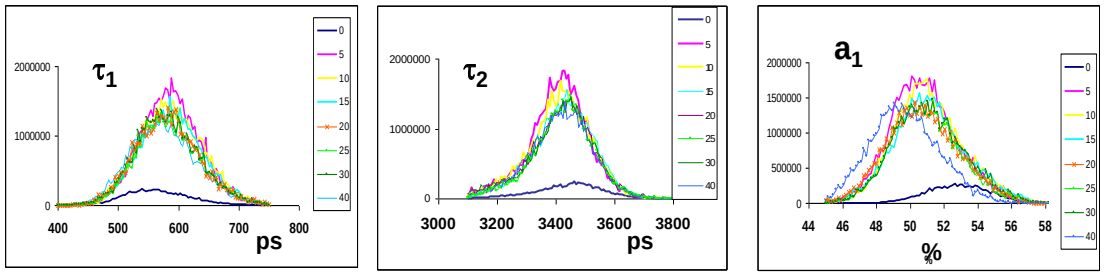

Figure 7-26 Histograms of fluorescence lifetime τ_1, τ_2 and a_1.

7.3.3 RhB-based ink printed on inkjet papers – samples with 10% ink density

A fluorescence lifetime analysis was carried out on samples with 10% ink density, where the ink dots are visible, with the purpose to observe the behaviour of the fluorescence lifetime of the RhB in various regions of the dots.

7.3.3.1 Paper A

When the dots printed in paper A were analysed it was found that the behaviour at the edge of the dot was completely different to the inner region. While the edge shows a mono-exponential decay with a FWHM between 3.4 and 4.4 ns, the inside of the dot shows a bi-exponential decay curve. This behaviour suggests that at the edge of the dot the dye is predominantly bound to alumina.

In the inner dot, τ_1 was found to be between 1.1 and 1.5 ns and τ_2 between 3.5 and 3.8 ns with an a_1 of 36%. These values are very similar to those observed in the same paper printed with 100% ink density at 20 μm (FWHM of τ_1: 1.43 ns and FWHM of τ_2: 3.42 ns, 3.9 and 4.8 ns). The a factor is similar which could indicate that the amount of RhB free and absorbed does not depend on the quantity of ink maybe because of saturation of the ink-receiving layer.

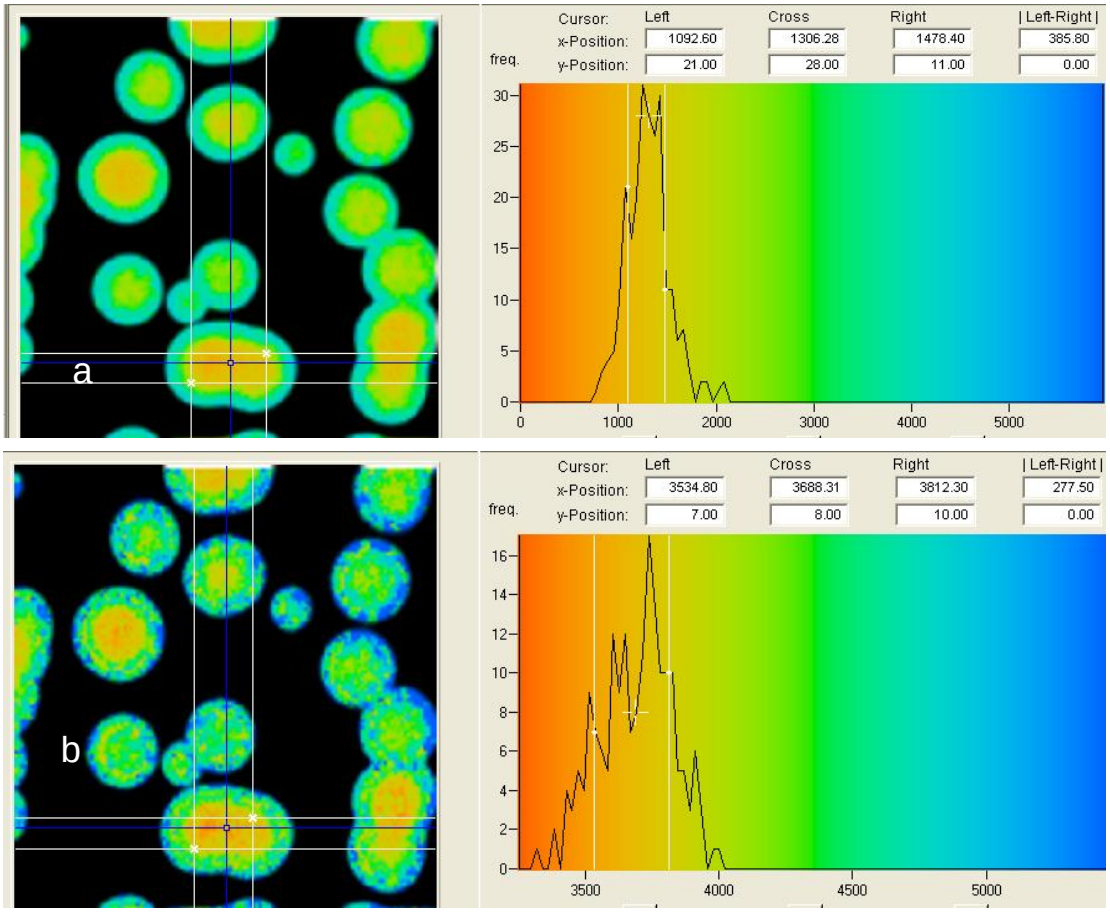

Figure 7-27 Fluorescence lifetime map and associated histogram, at 20µm depth, for τ_1 (a) of τ_2 (b) of one printed dot.

The value of τ_1 and τ_2 inside the dot suggests that 36% of the RhB remains free in solution and the rest is absorbed by the alumina and at the edge the RhB is predominantly bounded to the alumina.

7.3.3.2 Paper B

In terms of fluorescence lifetime, the behaviour inside the dot is generally the same as that observed in the sample with a 100% ink density, as it displays a bi-exponential decay curve. However, the lifetime values vary in different regions of the dot for this paper.

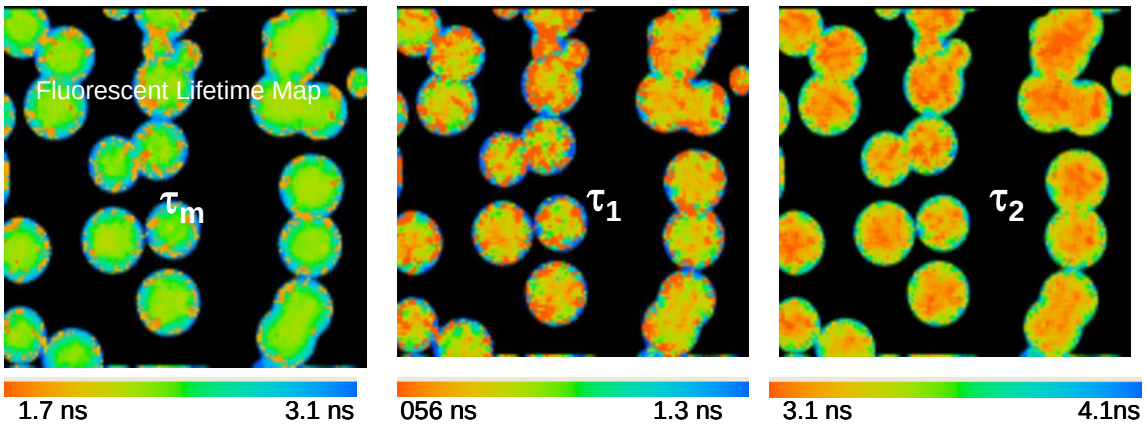

Figure 7-28 Fluorescence lifetime maps for the τ_m, τ_1, and τ_2 at 15 µm.

Figure 7-28 shows fluorescence lifetime maps for τ_m, τ_1 and τ_2 at 15 µm. It is interesting to highlight that the so-called coffee ring (stain around the dot) is observable through the fluorescence lifetime maps as a clear ring at the edge of the dot.

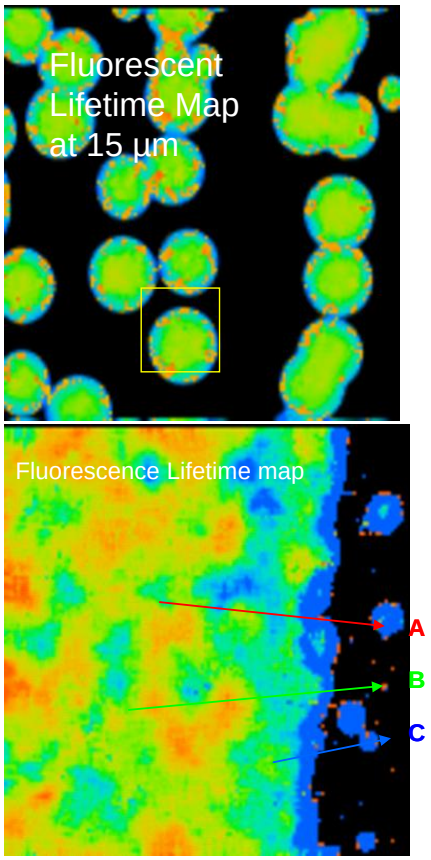

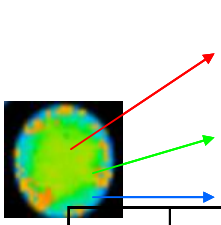

Crispia	τ_m	τ_1	τ_2	a_1
	ns	ns	ns	%
A	2.08	0.80	3.20	50
B	2.50	1.30	3.60	52
C	3.10	1.60	4.60	68

Crispia	τ_m	τ_1	τ_2	a_1
	ns	ns	ns	%
A	3.2	0.9	4.2	32
B	3.4	1.1	4.6	34
C	3.7	1.4	4.8	32

Figure 7-29 Fluorescent lifetime map at 15 µm for a 10% and a 100% ink-density sample, together with the values of τ_m, τ_1 and τ_2 in different regions.

Figure 7-29 shows shorter lifetimes in the centre of the dot. The surrounding or blue region of the dot shows a higher value of fluorescence lifetime but the intensity of the fluorescence is lower.

When comparing these results with those obtained for a 100 % colour intensity sample (Figure 7-29), the principal difference arises in the contribution of each value; the τ_1 component contributes with a higher percentage in the 10% ink-density sample, indicating that a greater proportion of the dye is free from interacting with the silica.

The behaviour of the ink in the paper B is different to the behaviour of the ink in paper A when forming the inkjet dots. In paper A, the RhB seems to be completely adsorbed by the alumina at the edge of the dot while in paper B the edge not only has RhB in solution or free, but its contribution is greater than that of the RhB adsorbed by the silica. Inside the dot both papers have some RhB free and adsorbed, but in paper B the amount of RhB free seems to be greater. This implies a different distribution of ink inside the paper that generates a different "structure" of the dot in the two papers.

However, the value of the longer lifetime component, found for this paper, is somewhat larger than values reported in the literature. It is well known that RhB has a longer lifetime in an adsorbed state than in aqueous solution because the internal rotation of the diethylamino groups is restricted by adsorption [37]. At the same time electrostatic interactions between the positively xanthene moiety of the dye and other anionic groups in the paper, ensuring a tighter fixation, could be the cause of the higher lifetime value. Another explanation of this high fluorescence lifetime could be due to the presence of J-Dimers formed due to specific adsorption geometry adopted by the RhB molecule when adsorbed onto the silica.

7.3.3.3 Si-containing papers with different pH

In general the papers with different pH show a single exponential decay curve in the outer ring of the dot and a bi-exponential decay curve in the inner region of the dot, with the exception of the pH 3.8 for which the whole dot exhibits a bi-exponential as observed in paper B.

Table 7-5 shows the lifetime values for the outer ring of the dot, for all the papers that exhibit this phenomenon. The range of values of this fluorescence lifetime component is very similar to the average fluorescence lifetime obtained inside of the dot.

Paper	τ ns
pH 8.0	3.5 – 4.7
pH 6.2	3.3 – 4.9
pH 4.8	3.1 – 3.6
pH 3.8	
Paper A	3.4 – 4.4
Paper B	

Table 7-5 Fluorescence lifetime values in the outer ring of the dot.

Table 7-6 compares the FWHM of the lifetime values inside the dots for all the papers.

Paper	τ_m ns	τ_1 ns	τ_2 ns	a_1 %	a_2 %
Paper pH 8	3.1 - 3.7	1.5 - 2.1	4.2 - 4.6	42.80	57.20
Paper pH 6	3.3 - 4.9	1.1 - 1.7	3.2 - 4.8	58.50	41.50
Paper pH 4	2.6 - 3.1	1.0 - 1.5	3.7 - 4.3	56.70	43.30
Paper pH 3	1.8 - 2.1	0.3 - 0.5	2.7 - 3.7	53.80	46.20
Paper A	3.4 - 4.3	0.9 - 1.4	3.5 - 3.9	38.20	61.80
Paper B	1.7 - 3.1	0.6 - 1.3	3.1 - 4.1	50.20	49.80

Table 7-6 FWHM of τ_m, τ_1 and τ_2, a_1, and a_2 inside the dots for pH 8.0, pH 6.2, pH 4.8, pH 3.8, Paper A and B.

The data collected for papers with pH 8, pH 6.2 and pH 4.8 shows that the behaviour of the RhB in these papers is very similar. Nevertheless it is observed that at lower pH, the value of τ_1 tends to decrease as it is shown in pH 4.8 compared with pH 6.2 and pH 8. In an acidic medium, as in pH 3.8, the behaviour is completely different but is in accordance with that observed for pH 3.8 with 100 % colour intensity printed paper (FWHM τ_1: 0.51 and 0.65 ns, and τ_2: 3.3 and 3.5 ns, and a_1 is around 50%).

However, looking at all pH values, Paper B τ_1 and τ_2 values appear to lie in between pH 3.8 and pH 4.8 values (and are shorter than values at higher pH), suggesting a pH value for paper

B around 4. FFIC reports that pH for Sec Crispia does indeed lie in the range between 3 and 4 .

7.4 Conclusions

The different values of fluorescence lifetimes obtained for paper A and B, two different inkjet coated papers with silica and alumina as their pigment in the ink-receiving layer, proved that 2P-FLIM is a sensitive technique able to detect changes in the RhB environment which in this case is the composition of the coating of the inkjet paper.

The lifetimes can not only be measured in different regions of the sample in the xy section but inside the sample in the xz section, showing in this way an indication of the fixation mechanism in terms of changes in the fluorescence lifetime of the dye (or potentially any fluorophore contained in the ink or the paper) under investigation.

Paper A and B are two inkjet papers, both with a microporous type of ink-receiving layer but with a different coating pigment. Paper A has alumina and paper B has silica as the ink-receiving layer pigment. The results obtained from paper A showed the presence of two species, which are likely to be RhB free or in solution with a τ around 1.4 ns and RhB closely interacting with the alumina with a longer fluorescence lifetime around 3.5 ns in agreement with the value for RhB adsorbed onto the surface of alumina reported in the literature.

The 2P-FLIM results for paper B showed that two different fluorescent lifetime components can be resolved, τ_1 with an average value between 1.03 ns and 1.37 ns and τ_2 with an average value between 4.4 and 7.5 ns. The presence of a longer lifetime component is consistent with previous studies of RhB absorbed on silica, and as for paper A, these results can be interpreted as indicators of the presence of RhB molecules both in bound and free state.

FFIC suggested that this type of paper is likely to have a super-crystal top layer. The fluorescence lifetime obtained in this region support this proposal, when compared with a literature study of RhB adsorbed by a different type of crystals with ideal and distorted sites, which showed that distorted adsorption sites were responsible for reduced fluorescence lifetimes.

The short fluorescence lifetime observed for RhB adsorbed in pH 3.8 paper can be attributed to effect of pH on the paper that in turn affects the RhB. The values of fluorescence lifetime obtained for paper B when compared with the fluorescence lifetime obtained for the different pH papers suggested a pH of 4 for this paper, in good agreement with the pH value reported for it. Thus RhB can be used to probe the pH of the paper.

Fluorescence lifetime values can be obtained for single inkjet dots in different regions in the xy and xz plane. This is a valuable tool to analyse the influence of the structure and composition of the printing medium on the composition of the dot formed. The fixation mechanism can be studied through the analysis of the different lifetime values obtained for the dye inside the dot. The lifetime property of the ink in the inkjet dots is different for paper A and B, indicating different distributions of the ink within the paper microstructure. In paper A, the dye seems to be completely adsorbed to the alumina particles at the edge of the dot, as there is no evidence of free RhB in this region, while in paper B some free RhB is detected in this region. Inside the dots both papers have RhB free and adsorbed but in different proportions.

8 Conclusions

The work presented in this thesis has investigated the fluorescence microscopy of inkjet prints, in order to develop methods and techniques useful in the routine evaluation of inkjet paper and prints, and for quality control procedures for paper and ink manufacturers.

Inkjet inks within the papers can be detected and observed by the confocal laser scanning microscopy (CLSM) technique. The high sensitivity of the CLSM in imaging the intrinsic fluorescence of the inks, together with absence of fluorescence from the paper, provides high-contrast images of printed inks, allowing the observation of the shape and distribution of the ink droplets on the paper.

CLSM was proven to be a very useful, non-destructive, non-invasive, easy and fast technique to evaluate the print quality of a printed sample as it can measure the position of the ink layer relative to the paper surface, and the vertical and radial distribution of the ink droplets on the paper. The depth of the ink layer can be quantified using the optical sectioning ability of the CLSM. This was validated by measuring the thickness of the ink layer in an xy image of a physical cross-section.

Two-photon laser scanning microscopy (2PLSM) improved the quality of the images obtained, compared with CLSM, showing in some cases the defects in the paper and how they can affect the penetration of the ink. The depth profiles obtained with 2PLSM report more accurately the shape of the dye profile within the paper. Nevertheless, CLSM can be used successfully to calculate the depth of penetration of the dye for comparative purposes between different prints or for evaluation of new dyes or papers.

With 2PLSM, UV fluorophores, such as the fluorescent molecules present in the papers, can be excited. It was observed that the dye attenuates the fluorescence intensity emitted by the paper, through an energy transfer process or by re-absorption. This process makes possible the indirect observation of non-fluorescent dyes as their location is shown as dark regions in the fluorescent intensity image of the paper.

Two-photon fluorescence lifetime imaging microscopy (2P-FLIM) has proved to be a valuable technique to study dye–paper interactions through the measurements of fluorescence lifetimes, because of its sensitivity to changes in the surrounding environment.

The work presented in this thesis is a preliminary approach to investigate the usefulness of 2P-FLIM as a technique to study dye–paper interactions. The inkjet system used as a probe to study dye–paper interactions, through changes in fluorescence lifetimes, included prints of RhB-ink printed in four papers with different pH and two papers with different coating pigment (silica and alumina). This work successfully exploited the suppression of the radiationless decay of RhB under adsorption, such that the fluorescence lifetime in an adsorbed state is longer than in an aqueous solution, because the internal rotation of the diethylamino groups is inhibited.

The results proved that the 2P-FLIM technique was able to differentiate between different coatings as the fluorescence lifetime for the silica paper was different to the fluorescence lifetime of the alumina paper. The effect of the coating in the adsorption mechanism was observed as well, as in the alumina paper the structure apparent in the FLIM image of the ink dot is different to the structure of the dot in the silica paper.

Because of the ability of the 2P-FLIM technique to generate fluorescence lifetime maps and their correspondent histograms, the behaviour of the fluorophore can be analysed in different regions. This means that for 100% colour density samples, the behaviour of the ink at the beginning of each row and in different areas of the print can be compared with each other, this observation being very important when analysing the quality of the surface of the paper, or pigment dispersion in the coating, or the effect of pigment size on the paper. Also, being able to analyse the fluorescence lifetime at different positions within single dots is promising, as this information will tell how the microenvironment affects the fixation and spread of the inkjet droplet. This constitutes valuable information when new ink formulations or paper coatings need to be evaluated as the fluorescence lifetime maps of the dye will indicate the percentage of the dye in solution and adsorbed in each region of the dot, in each case.

2P-FLIM not only produces two-dimensional fluorescence lifetime maps, but it also has the capability to optically slice the sample, showing the behaviour inside the print. In this way the penetration of the dye within the paper can be studied. The different layers of the coating

of the inkjet papers can be identified as they present different molecular environments to the dye fluorophore. In this work, the position of the second layer was detected and the changes that it causes to the fluorescence lifetimes of the dye could be observed.

Although only one model ink system was studied with 2P-FLIM in this thesis, there is the potential of using other models to investigate dye–media interactions, for example different dyes in the same paper. The possibility of creating fluorescence lifetime maps not only at the surface, but at different depths within the paper, and its sensitivity to environmental changes, makes 2P-FLIM a very promising technique for the study of dye-media interactions, offering a great potential for looking at the effects of new formulations in drying times, in dot shapes, in dot structures and in ink penetration. In principle, the use of different model fluorophores could lead to a full understanding of the fixation mechanism of the ink onto the substrate.

On the basis of the work presented here, a number of other potential applications of fluorescence microscopy to the study of inkjet prints can be suggested. An important advantage of CLSM and 2P-CLSM that can be exploited is the ability to detect simultaneously in different channels, fluorophores with different wavelength emission, which means that the formation of secondary colours could be monitored with the CLSM by detecting the primary colours in different channels. Secondary colours are the result of applying different numbers of drops of different colours to the paper to simulate the colour needed. This means that possible bleeding between colours could be detected; errors in dot placement, effects of rough edges when overlapping and many other problems can be monitored.

In addition to the analysis of soluble dye-inks, preliminary results showed that fluorescence microscopy can be used to investigate pigment-based ink, widely employed nowadays. As an illustration, Figure 8-1 shows the fluorescence lifetime of a pigmented ink printed on an inkjet paper, proving that it is possible to successfully image this completely different type of ink and the scope is extensive for future investigation of pigment-based ink.

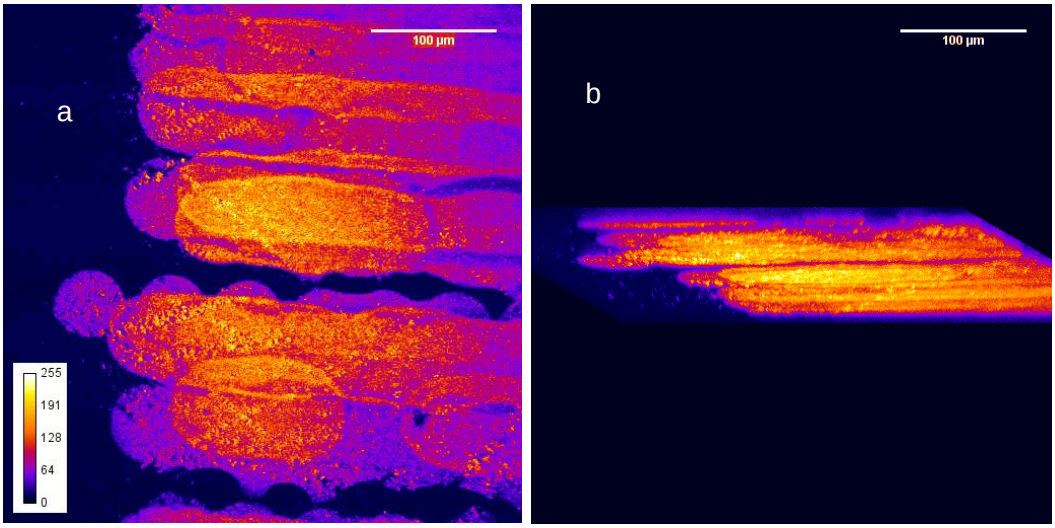

Figure 8-1 CLSM fluorescence intensity image (a) of a pigmented ink and its 3-D projection (b).

Figure 8-1 shows a CLSM fluorescence intensity image of a pigment-based ink printed in an inkjet paper (a) and its three-dimensional projection illustrating a very thin ink layer through the whole print. The depth profile obtained for the pigmented-ink was much smaller (around 5 µm) than that obtained for the soluble dyes, showing that the pigment remains very close to the surface.

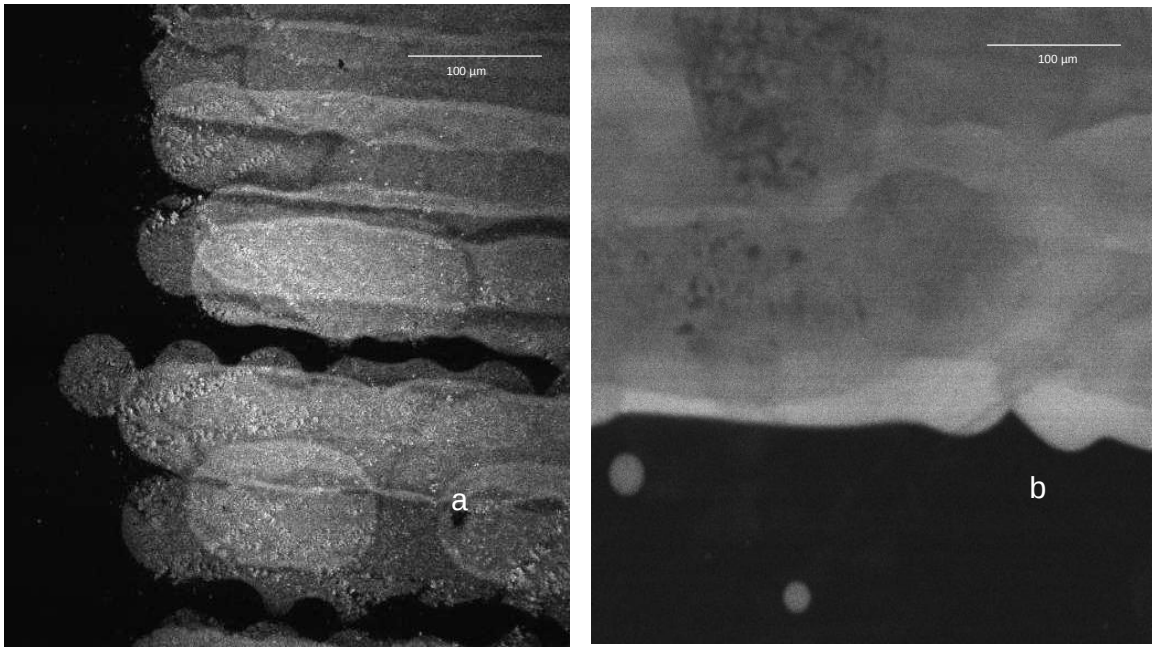

Figure 8-2 Fluorescence intensity image of a pigmented ink print (a) and fluorescence intensity image of a dye-ink print (b) with a 100% colour intensity.

Figure 8-2 shows a comparison between the fluorescence intensity image of a pigmented ink print (a) and a soluble dye-ink print (b), both images are taken with a 100% colour density sample. From the images it can be observed that they are absorbed or fixated in the paper by a different mechanism, the pigment-based ink shows free spaces between rows and the superposition of the rows is evident while the soluble dye is absorbed more homogeneously with no free spaces and the superposition of the lines is not that clear.

As well as observing the behaviour of the dye, the influence of the dye on the paper can also be studied with 2P-FLIM, analysing the changes in the fluorescence lifetime shown by the papers when printed. In a preliminary experiment, the behaviour of different papers printed with RhB was observed. Figure 8-3 shows a comparison of the average fluorescence lifetime maps (τ_m) obtained from pH 3.8 and pH 8 prints, when observing the fluorescence from the paper. The FLIM images and their correspondent histograms suggest that the pH of the substrate affects the interaction between ink and paper; on an acidic substrate the presence of the dye increases the fluorescence lifetime of the paper, while for the alkaline substrate, the interaction with the dye decreases the fluorescence lifetime.

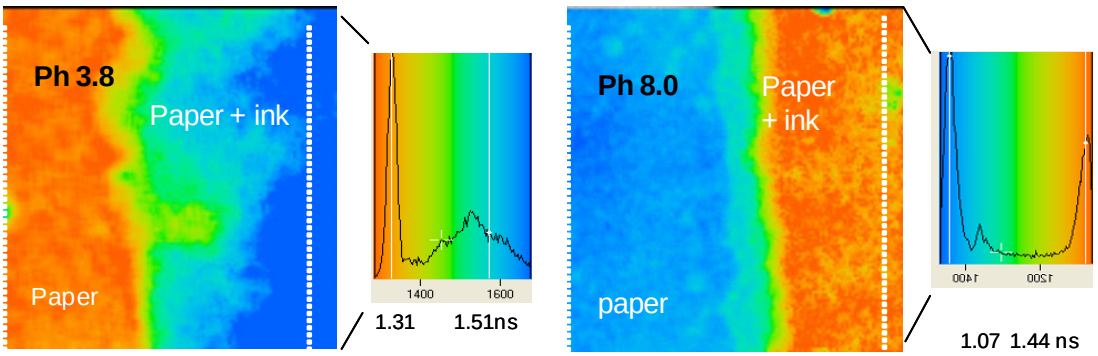

Figure 8-3 Average fluorescence lifetime maps and associated histogram for the fluorescence of papers of pH 3.2 and 8.0 printed with RhB.

The information obtained from this type of study could help in the analysis and developing of new coating formulations and, together with the study of the fluorescence lifetimes of the dye when printed will help in the understanding of ink-paper interactions and fixation mechanisms.

References

1. C. Williams., *Ink-jet technology moves beyond paper.* Physics World, 2006: p. 24-29.

2. G. Martin, I. Hutchings., *Recent Developments in the World of Inkjet* in *Inkjet Interest Group*. 2008, Cambridge University: Cambridge.

3. E. Svanholm., *Printability and Ink-Coating Interactions in Inkjet Printing*, in *Faculty of Technology and Science -Chemical Engineering*. 2007, Karstad University: Karlstad.

4. H. Le., *Progress and Trends in Ink-jet Printing Technology.* Journal of Imaging Science and Technology 1998. **42**(1): p. 49-62.

5. H. Lee, P. Flemimg and J. Cawthorne, *Influence of silica and alumina oxide on coating structure and print quality of ink-jet papers.* Tappi Journal, 2005. **4**: p. 11-16.

6. P. Atkins , J.d. Paula, *Elements of physical chemsitry*, Fourth ed. 2005, New York: Oxford University Press.

7. R. Allen., *Colour Chemistry*. First ed. 1971: Nelson.

8. P. Atkins, J. de Paula., R. Friedman, *Quanta, Matter and Change. A Molecular Approach to Physical Chemistry*. First ed. 2009, New York.

9. J. P. Simons., *Photochemistry and spectroscopy*. First ed. 1971, London: Wiley-Interscience.

10. M. Müller., *Introduction to Confocal Fluorescence Microscopy* Second ed. 2006: SPIE- The International Society for Optical Engineering.

11. J. R. Lakowicz., *Principles of Fluorescence Spectroscopy*. Third ed. 2006: Springer Science-Business Media, LLC

12. B. Herman, *Fluorescence Microscopy*. Second ed. 1998, Oxford: BIOS Scientific Publishers Limited.

13. E. Graham., *The Application of Fluorescence Lifetime Imaging Microscopy to Quantitatively Map Mixing and Temperature in Microfluidic System*. 2007, Edinburgh University

14. R K. Neely., *The Photophysical Properties of 2-Aminopurine and its application as a probe of DNA-Protein Interactions*. 2005, Edinburgh University.

15. C. Jones, K. Suhling., *Refractive Index sensing using Fluorescence Lifetime Imaging (FLIM)*, Journal of Physics: Conference Series, 2006. **45**: p. 223.

16. C. Sheppard, D. M. Shotton., *Confocal Laser Scanning Microscopy*. First ed. 1997, Oxford: BIOS Scientific Publishers Limited.

17. Bio-Rad, *Bio-Rad 2000MP Manual*

18. Rasband, W.S. *ImageJ*. 1997-2008 [cited 05-05-2010]; Available from: http://rsb.info.nih.gov/ij/.

19. A. Diaspro., *Two-photonfluorescence excitation and related techniques in biological microscopy.* Quarterly Reviews of Biophysics, 2005. **38** (2): p. 97-166.

20. W. Becker., *The bh TCSPC handbook*, in *High Performance Photon Counting*, Becker and Hickl, Editor. 2006.

21. K. Vikman., *Studies on Fastness Properties of Ink jet prints on Coated Papers*, in *Department of Forest Products Technology*. 2004, Helsinki University of Technology: Helsinki.

22. H. Lee, P. Fleming., *Influence of pigment particle size and pigment ratio on printability of glossy ink jet paper coatings.* The Journal of Imaging Science and Technology 2005. **49** (1): p. 54-60.

23. J. Sarafano., *Factors Affecting Dot. Fidelity in Solvent Based Publication Gravure.* American Ink Maker, 1999. **77**: p. 732-36.

24. J. H.Bohórquez, K. J. Courian, F. Drogo, C. A.E. Hall, C. L. Holstun, A. R. Scandalis, M. E. Shepard., *Laser-Comparable Inkjet Text Printing*. Hewlett-Packard Journal, 1994: p. 9-17.

25. P. D. Fleming, S. Halwawala, and M. K. Joyce, *Interpretation of Dot Fidelity of Ink Jet Dots Based on Image Analysis.* The Journal of Imaging Science and Technology, 2003. **47** (5): p. 394-399.

26. B. Lozo, T. Vuorinen, T. Mudck., *Nondestructive Microscopic and Spectroscopic Methods for Depth Profiling of Ink Jet prints.* Journal of Imaging Science and Technology 2006. **50**(4): p. 333-340.

27. T. Enomae., *Three-dimensional distribution of ink-jet inks in paper acquired by confocal laser scanning microscope.* 58th APPITA Annual conference & Exhibition Proceedings, 2004: p. 577-588.

28. L. Yang., *Ink -Paper Interactions : A study in inkjet colour reproduction* in *Department of Science and Technology*. 2003, Linkoping University: Linkoping.

29. K. Vikman., *Applicability of FTIR and Raman Spectroscopic Methods to the Study of Paper–ink Interactions in Digital Prints.* Journal of Imaging Science and Technology, 2003. **47**(2): p. 139-148.

30. D. Ivutin., *Ink Penetration Mechanism for Modified Calcium Carbonate-coated Ink-jet Paper.* Japan Tappi J., 2005. **59**: p. 1694-1705.

31. S. D. Hoath, G. D. Martin, T. R. Tuladhar, M. R. Mackley, and D. Vadillo, *Links Between Ink Rheology, Drop-on-Demand Jet Formation, and Printability.* Journal of Imaging Science and Technology. 2009, **53**(4): p. 041208.

32. Bonetto, P. *OrtView- PLugin of Image J*. 2003

33. J. Bakker, H.Arwin., *Determination of refractive index of printed and unprinted paper using spectroscopic ellipsometry.* Thin Solid Films, 2004. **455-456**: p. 361-365.

34. U. Lindqvist, B. Zhmud, E. Wall., *Innovations in inkjet technology*. 2003, VTT Information Technology: Espoo- Finland.

35. A. G. Ryder, T. J. Glynn , J. J. Morrison., *Time-domain measurement of fluorescence lifetime variation with pH.* SPIE.

36. D. Magde, P.G. Seybold., *Solvent Dependence of the Fluorescence Lifetimes of Xanthene Dyes.* Photochemistry and Photobiology, 1999. **70**(5): p. 737-744.

37. T. A. Smith, D. J. Haines, K. P.Ghiggino, D.P. Millar., *Time-resolved fluorescence anisotropy measurements of the adsorption of Rhodamine-B and a labelled polyelectrolyte onto colloidal silica.* Colloid Polym Sci, 1998. **276**: p. 1032-1037.

38. M. J. Snare, K.P.Ghiggino and P.J. Thistlethwaite., *The Photophysics of Rhodamine B.* Journal of Photochemistry and Photobiology, 1982. **18**: p. 335-346.

39. G. Qian., *Study on the microstructural evolution of silica gel during sol–gel–gel-glass conversions using the fluorescence polarization of rhodamine B.* J.Phys. D: Appl.Phys., 1999. **32**: p. 2462-2466.

40. A. A. El-Rayyes, A. Klein, S. Barri., *Acidity of all-silica MCM-41 studied by laser spectroscopy of adsorbed fluorescent probe compounds.* Catalysis Letters 2004. **97**(1-2): p. 83-90.

41. N. Negishi, H. Yamashita, M. A. Fox, M. Anpo., *Photophysical Properties and Photochemical Stability of Rhodamine B Encapsulated in SiO_2 and Si-Ti Binary Oxide Matrices by the Sol-Gel Method.* Langmuir, 1994. **10**: p. 1772-1776.

42. N. Mchedlov-Petrossyan, N. Doroshenko., *Ionic Equilibria of Fluorophores in Organized Solutions: The Influence of Micellar Microenvironment on Protolytic and*

Photophysical Properties of Rhodamine B. Journal of Fluorescence, 2003. **13**(3): p. 235-248.

43. F. del Monte., *Formation of Fluorescent Rhodamine B J-Dimers in Sol-Gel Glasses Induced by the Adsorption Geometry on the Silica Surface.* J. Phys. Chem. , 1998. **102**: p. 8036-8041.

44. K. Kemnitz, I. Yamazaki, N. Nakashima, K. Yoshihara., *Site-Dependent Fluorescence Llfetlmes of Isolated Dye Molecules Adsorbed on Organic Single Crystals and Other Substrates.* J. Phys. Chem. , 1987. **91**: p. 1423-1430.

45. K .Itoh, M. Nakao, K. Honda., *Fluorescence Quenching Processes of Rhodamine B on Oxide Semiconductors and Light-Harvesting Action of Its Dimers.* J. Am.Chem.Soc, 1983. **106**: p. 1620-1627.

46. Becker , H. *Data Analysis Software for Fluorescence Lifetime Imaging Microscopy*. 2006 [cited 2009].

Appendix I

Excitation- Emission spectra of dyes in solution

Ar52

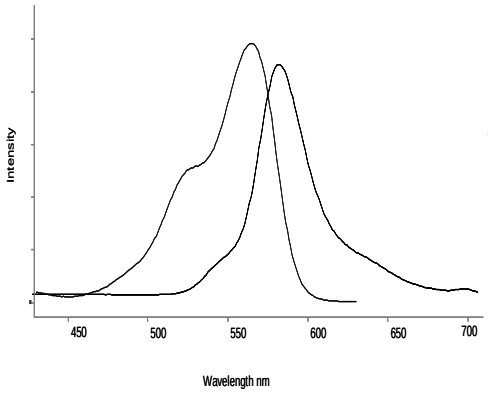

S192332/2

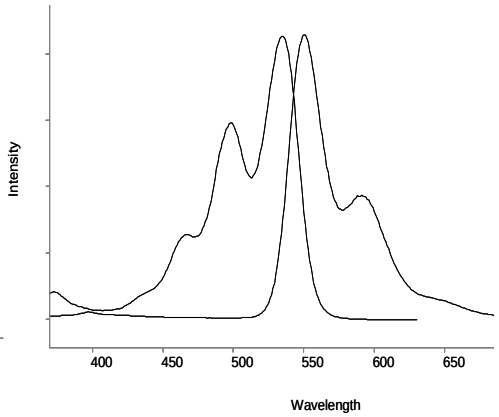

OAM

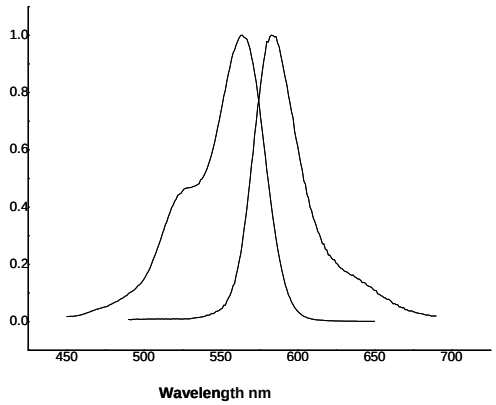

Excitation (left) and Emission (right) spectra of inkjet dyes in solution. The excitation spectra was recorded at an emission wavelength of 650 nm and the emission spectra was recorded at an excitation wavelength of 400 nm for Ar52 and OAM and 350 nm for S192332/2.

Inkjet paper coating structure

MEDIA NAME	TYPE	NUMBER OF LAYERS SUGGESTED BY ANALYSIS	COMPOSITION	
A	MICROPOROUS	5	1	40um Alumina +trace organics.
			2	5-10um Ti, O, Al, Si, C and possibly Na present - could suggest an organic with TiO2 and mixed inorganics as fillers
			3	160um Cellulose.
			4	5-10um Ti, O, Al, Si, C and possibly Na present - could suggest an organic with TiO2 and mixed inorganics as fillers
			5	25um Alumina +trace organics inc. Cl + possibly Na.
B	MICROPOROUS	4	1	37um Silica +polythene binder with traces of alumiunium.
			2	37um Cellulose with fine dispersion of titania.
			3	230um Cellulose.
			4	37um Polythene.
C	MICROPOROUS	4	1	35um Silica +polythene binder.
			2	25um Polythene
			3	160um Cellulose.
			4	60um Polythene +silica filler.
D	MICROPOROUS / SWELLABLE	5	1	Gelatin +silica (no thickness given).
			2	Polythene (no thickness given)
			3	Cellulose (no thickness given).
			4	Polythene (no thickness given)
			5	Gelatin +silica (no thickness given).
E	SWELLABLE	UNKNOWN		N / A
F	MICROPOROUS	4	1	35um Silica +polythene binder.
			2	25um Polythene
			3	160um Cellulose.
			4	60um Polythene +silica filler.
G	PLAIN	UNKNOWN		N / A

Emission spectra: Rhodamine B prints in different papers.